

วัสดุแคโทดซึ่งต้นทุนต่ำและทนทานสำหรับแบตเตอรี่สังกะสีไอออนและกระบวนการ
สกัดลิกนินที่เป็นมิตรต่อสิ่งแวดล้อมเพื่อการประยุกต์ใช้ในด้านพลังงาน

**LOW-COST ROBUST Zn-ION BATTERY CATHODE AND ECO-FRIENDLY
EXTRACTION OF LIGNIN WITH ENERGY-RELATED APPLICATIONS**



วิทยานิพนธ์นี้เป็นส่วนหนึ่งของการศึกษาตามหลักสูตรปริญญาวิศวกรรมศาสตรมหาบัณฑิต

สาขาวิชาวิศวกรรมเคมี

คณะวิศวกรรมศาสตร์

สถาบันเทคโนโลยีพระจอมเกล้าเจ้าคุณทหารลาดกระบัง

พ.ศ. 2566

KMITL-2023-EN-M-220-111

เอกสารนี้เป็นเอกสารที่สงวนไว้สำหรับการใช้งานเพื่อการศึกษาเท่านั้น ไม่อนุญาตให้นำไปใช้ประโยชน์ด้านการค้า
ไม่ว่ากรณีใดๆ ทั้งสิ้น อีกทั้งห้ามมิให้ดัดแปลงเนื้อหา และต้องอ้างอิงถึงเจ้าของเอกสารทุกครั้งที่มีการนำไปใช้

**LOW-COST ROBUST Zn-ION BATTERY CATHODE AND ECO-FRIENDLY
EXTRACTION OF LIGNIN WITH ENERGY-RELATED APPLICATIONS**



**A THESIS SUBMITTED IN PARTIAL FULFILLMENT
OF THE REQUIREMENT FOR THE DEGREE OF
MASTER OF ENGINEERING IN CHEMICAL ENGINEERING
SCHOOL OF ENGINEERING
KING MONGKUT'S INSTITUTE OF TECHNOLOGY LADKRABANG
2023
KMUTL-2023-EN-M-220-111**

เอกสารนี้เป็นเอกสารที่สงวนไว้สำหรับการใช้งานเพื่อการศึกษาเท่านั้น ไม่อนุญาตให้นำไปใช้ประโยชน์ด้านการค้า
ไม่ว่ากรณีใดๆ ทั้งสิ้น อีกทั้งห้ามมิให้ดัดแปลงเนื้อหา และต้องอ้างอิงถึงเจ้าของเอกสารทุกครั้งที่มีการนำไปใช้



COPYRIGHT 2023

SCHOOL OF ENGINEERING

KING MONGKUT'S INSTITUTE OF TECHNOLOGY LADKRABANG

เอกสารนี้เป็นเอกสารที่สงวนไว้สำหรับการใช้งานเพื่อการศึกษาเท่านั้น ไม่อนุญาตให้นำไปใช้ประโยชน์ด้านการค้า
ไม่ว่ากรณีใดๆ ทั้งสิ้น อีกทั้งห้ามมิให้ดัดแปลงเนื้อหา และต้องอ้างอิงถึงเจ้าของเอกสารทุกครั้งที่มีการนำไปใช้

Thesis title	Low-cost robust Zn-ion battery cathode and eco-friendly extraction of lignin with energy-related applications
Student name	Mr. Trakarn Yimtrakarn
Student ID.	63601052
Degree	Master of Engineering
Program	Chemical Engineering
Year	2023
Advisor	Asst. Prof. Dr. Nuttapol Lerkkasemsan

ABSTRACT

Demands for energy and natural resources are rapidly increasing, which necessitates advancements in energy research to meet humanity's ever-growing needs. As a result, the development of innovative solutions for sustainable energy storage is of utmost importance. This abstract presents two interconnected studies focused on addressing key challenges in the field. The first study explores the use of a low-cost and robust cathode material for zinc-ion batteries (ZIBs), while the second study investigates an eco-friendly extraction of lignin for energy-related applications. The findings provide valuable insights into the development of inexpensive battery cathode materials and the alternative non-hazardous lignin extraction processes, facilitating the progress towards greener energy production and storage. Both projects aim to improve the efficiency and sustainability of how energy is produced and stored, supporting the development of a more sustainable future.

The development of innovative solutions for sustainable energy storage has been proved crucial in response to the exponentially growing energy demand. ZIBs have emerged as a promising technology due to their safety, low toxicity, inexpensiveness, and ability to transfer two electrons. However, the electrochemical performance of most

cathode materials used in non-aqueous ZIBs remains unsatisfactory. To address this challenge, an economical Prussian blue analogue called sodium manganese hexacyanoferrate (NMHCF) was explored as a cathode material due to its facile synthesis, large open framework, and chemical and electrochemical tunability. NMHCF was found to exhibit high framework flexibility and structural reversibility upon divalent guest intercalation. The crystallographic vacancies and coordinated water molecules were believed to assist the cation diffusion during cell cycling. *Ex-situ* characterization techniques, including energy-dispersive X-ray spectroscopy (EDX), X-ray diffraction (XRD), and X-ray absorption spectroscopy (XAS), were used to provide a deeper understanding of NMHCF's properties. The findings guide the development of inexpensive cathode materials suitable for large-scale energy storage systems.

Furthermore, lignin, one of the most abundant natural aromatic polymers found in plant biomass, holds promise for energy-related applications, particularly as a precursor for high-value liquid fuel synthesized from lignin-derived phenolic compounds. The study was conducted to extract lignin using a microwave-assisted solvent extraction method. Rubberwood sawdust (*Hevea brasiliensis*) was subjected to extraction with either ethanol or isopropanol as an organic-based solvent. Microwave power levels and extraction times were varied to optimize the extraction process. The extracted lignin was characterized using several techniques such as Klason lignin analysis, Fourier transform infrared spectroscopy (FT-IR), two-dimensional heteronuclear single-quantum coherence nuclear magnetic resonance spectroscopy (2D HSQC NMR), ultraviolet-visible spectroscopy (UV-vis), and bomb calorimetry. The results demonstrated that longer extraction times and higher microwave power levels led to

increased lignin yield. Additionally, ethanol exhibited a higher extraction yield compared to isopropanol. These insights enhance our understanding of lignin extraction processes and contribute to the utilization of lignin in energy-related applications.

Keywords: Manganese hexacyanoferrate, Zn-ion batteries, Non-aqueous electrolyte, Lignin extraction, Microwave



เอกสารนี้เป็นเอกสารที่สงวนไว้สำหรับการใช้งานเพื่อการศึกษาเท่านั้น ไม่อนุญาตให้นำไปใช้ประโยชน์ด้านการค้า
ไม่ว่ากรณีใดๆ ทั้งสิ้น อีกทั้งห้ามมิให้ดัดแปลงเนื้อหา และต้องอ้างอิงถึงเจ้าของเอกสารทุกครั้งที่มีการนำไปใช้

หัวข้อวิทยานิพนธ์	วัสดุแคโทดซึ่งต้นทุนต่ำและทนทานสำหรับแบตเตอรี่สังกะสีไอออนและกระบวนการสกัดลิเทียมที่เป็นมิตรต่อสิ่งแวดล้อมเพื่อการประยุกต์ใช้ในด้านพลังงาน
นักศึกษา	นายตระการ ยิ้มตระการ
รหัสประจำตัว	63601052
ปริญญา	วิศวกรรมศาสตรมหาบัณฑิต
สาขาวิชา	วิศวกรรมเคมี
พ.ศ.	2566
อาจารย์ที่ปรึกษาวิทยานิพนธ์	ผศ.ดร.ณัฐพล ฤกษ์เกษมสันต์

บทคัดย่อ

ในปัจจุบันความต้องการทางด้านพลังงานและทรัพยากรธรรมชาติเพิ่มขึ้นอย่างรวดเร็วทั้งนี้จึงเกิดความจำเป็นในการวิจัยด้านพลังงานเพิ่มมากขึ้นเพื่อตอบสนองความต้องการของมนุษย์ในยุคปัจจุบัน การพัฒนานวัตกรรมสำหรับการจัดเก็บพลังงานอย่างยั่งยืนจึงเป็นสิ่งสำคัญที่สุดในเวลานี้ ในงานวิจัยนี้นำเสนอการศึกษาสองส่วนที่เชื่อมโยงในเรื่องพลังงานเพื่อแก้ไขปัญหาที่เกิดขึ้น ในการศึกษาแรกเป็นการหาวัสดุแคโทดที่มีราคาถูกและมีความทนทานสำหรับแบตเตอรี่ชนิดสังกะสีไอออน (Zinc-ion batteries; ZIBs) การศึกษาที่สองคือการศึกษากระบวนการสกัดลิเทียมเพื่อใช้เป็นพลังงานที่เป็นมิตรต่อสิ่งแวดล้อม ผลของการศึกษาสามารถสร้างความเข้าใจในการพัฒนาวัสดุแคโทดสำหรับแบตเตอรี่ราคาถูกและกระบวนการสกัดลิเทียมที่ไม่เป็นอันตรายซึ่งมีประโยชน์ในการพัฒนาการผลิตและจัดเก็บพลังงานที่เป็นมิตรต่อสิ่งแวดล้อมมากขึ้น ทั้งสองโครงการมีเป้าหมายในการเพิ่มประสิทธิภาพและความยั่งยืนของกระบวนการผลิตและจัดเก็บพลังงานที่ต้องตระหนักถึงการผลิตที่ไม่ก่อให้เกิดอันตรายต่อสิ่งแวดล้อมให้ได้มากที่สุด

เนื่องจากการพัฒนานวัตกรรมสำหรับการจัดเก็บพลังงานที่ยั่งยืนเป็นที่ประจักษ์ว่ามีความสำคัญอย่างมากต่อความต้องการพลังงานมากขึ้นในโลกที่เป็นพลวัต ZIBs มีความเป็นไปได้สูงในเชิงปฏิบัติเนื่องจากมีความปลอดภัยสูง ความเป็นพิษต่ำ ราคาถูกและสามารถถ่ายโอนได้ถึงสองอิเล็กตรอน อย่างไรก็ตามวัสดุแคโทดส่วนมากใน ZIBs แบบอเล็กโทรไลต์ที่ไม่มีน้ำเป็นส่วนประกอบมีประสิทธิภาพเชิงไฟฟ้าเคมีไม่สูงเท่าที่ควร ในการทดลองครั้งนี้จึงได้นำสารในกลุ่มปรัชชันบลูหรือโซเดียมแมงกานีสเฮกซะไซยาโนเฟอเรต (sodium manganese hexacyanoferrate; NMHCF) เป็น

วัสดุแคโทดเนื่องจากสังเคราะห์ได้ง่าย มีโครงสร้างขนาดใหญ่และมีความสามารถในการปรับแต่งโครงสร้างสูง จากผลการทดลองพบว่า NMHCF มีความยืดหยุ่นของโครงสร้างสูงซึ่งยังมีความสามารถในการคืนรูปของโครงสร้างเมื่อเกิดกระบวนการแทรกตัวของไดวาเลนต์ไอออน เมื่อมีการควบคุมความบกพร่องทางโครงสร้างอย่างเหมาะสม ประกอบกับโมเลกุลน้ำที่อยู่ในโครงสร้างมีส่วนช่วยส่งเสริมการเคลื่อนตัวของประจุในแบตเตอรี่ ในการศึกษานี้ได้ใช้เทคนิคการวิเคราะห์แบบ Ex-situ เช่น การวิเคราะห์องค์ประกอบทางเคมีด้วยสเปกโทรเมตรีรังสีเอกซ์แบบกระจายพลังงานที่ใช้ร่วมกับกล้องจุลทรรศน์อิเล็กตรอนแบบผ่าน (EDX) เทคนิคการวิเคราะห์การเลี้ยวเบนของรังสีเอกซ์ (XRD) และสุดท้ายเทคนิคการวิเคราะห์สเปกตรัมการดูดกลืนรังสีเอกซ์ (XAS) ถูกนำมาใช้เป็นเครื่องมือเพื่อให้เข้าใจคุณลักษณะของ NMHCF มากขึ้น ผลของการศึกษาจะนำไปสู่การพัฒนาวัสดุแคโทดที่มีราคาถูกลงและเหมาะสมสำหรับระบบการจัดเก็บพลังงานขนาดใหญ่

ลิกนินเป็นหนึ่งในอะโรมาติกโพลีเมอร์ที่สามารถพบได้มากที่สุดตามสารชีวมวลจากพืช ทั้งยังมีความสามารถประยุกต์ใช้ผลิตเชื้อเพลิงของเหลวที่มีมูลค่าสูงจากสารประกอบพีนอลิกที่มาจากลิกนิน จุดประสงค์ของการศึกษานี้คือเพื่อสกัดลิกนินโดยใช้วิธีการสกัดด้วยไมโครเวฟ ผงละเอียดจากไม้ยางพารา (*Havea Brasiliensis*) ถูกนำไปสกัดด้วยสารละลายอินทรีย์ เช่น เอทานอลหรือไอโซโพรพานอล กำลังของไมโครเวฟและเวลาที่สกัดถูกปรับเพื่อเพิ่มประสิทธิภาพของกระบวนการสกัด ลิกนินที่ได้จากการสกัดนั้นนำไปวิเคราะห์โดยใช้เทคนิคต่างๆ เช่น การวิเคราะห์หาปริมาณลิกนิน 2D HSQC นิวเคลียร์แมกเนติกเรโซแนนซ์สเปกโทรสโกปี (2D HSQC NMR) เทคนิคยูวี-วิสิเบิลสเปกโทรสโกปี (UV-vis) และวิเคราะห์หาค่าพลังงานความร้อน จากการทดลองพบว่าการใช้เวลาในการสกัดที่มากขึ้นและกำลังไมโครเวฟที่สูงขึ้นจะส่งผลให้ได้ปริมาณลิกนินที่มากขึ้นด้วยเช่นกัน นอกจากนี้เอทานอลมีประสิทธิภาพในการสกัดได้ดีกว่าไอโซโพรพานอล ข้อมูลเชิงลึกเหล่านี้จะช่วยเพิ่มความเข้าใจเกี่ยวกับกระบวนการสกัดลิกนินและนำไปสู่การประยุกต์ใช้ลิกนินที่เกี่ยวข้องกับพลังงานได้มากขึ้น

คำสำคัญ แมงกานีสเฮกซะยานเพอเรต; แบตเตอรี่ชนิดสังกะสีไอออน; อิเล็กโทรไลต์ที่ไม่มีน้ำเป็นองค์ประกอบ; การสกัดลิกนิน; คลื่นไมโครเวฟ

ACKNOWLEDGEMENT

Words cannot express how grateful I am to my esteemed supervisors, Professor Watchareeya Kaveevivitchai and Professor Nuttapol Lerkkasemsan, for their invaluable guidance, unwavering patience, and constructive feedback, which has shaped my research and propelled me to academic excellence. Their advice and support have been invaluable in my personal and professional development.

I also would like to express my deep appreciation to KMITL and NCKU for providing the opportunity and resources to pursue my academic aspirations. Without their support and generosity, my journey toward achieving my academic goals would have been much more challenging.

The most important for me is my family who has been an unflagging source of love and support throughout this challenging journey, and I would like to extend my heartfelt gratitude to them, particularly my mother and father, for their unwavering encouragement and understanding during my difficult time, which was full of stressful and frustrating situations.

Lastly, I want to thank my labmates and friends in both my native country and Taiwan for their essential assistance. Their constant emotional support, encouragement, and motivation have been vital in keeping me motivated and focused throughout my academic journey. This thesis would not have been possible without their assistance. Taiwan's laboratory colleagues, who helped me a lot during my time living in Taiwan, have also served me as amazing and fruitful here.

In conclusion, I am profoundly grateful to all those who have contributed to my academic journey, and I look forward to continuing to learn and grow under their guidance and mentorship.

Trakarn Yimtrakarn



เอกสารนี้เป็นเอกสารที่สงวนไว้สำหรับการใช้งานเพื่อการศึกษานี้เท่านั้น ไม่อนุญาตให้นำไปใช้ประโยชน์ด้านการค้า
ไม่ว่ากรณีใดๆ ทั้งสิ้น อีกทั้งห้ามมิให้ดัดแปลงเนื้อหา และต้องอ้างอิงถึงเจ้าของเอกสารทุกครั้งที่มีการนำไปใช้

TABLE OF CONTENTS

Chapter	Page
ABSTRACT.....	I
ACKNOWLEDGEMENT	VI
TABLE OF CONTENTS.....	VIII
LIST OF FIGURES	XII
Chapter 1 Low-cost robust zinc-ion battery cathode	1
1.1 Introduction and Research Motivation.....	1
1.1.1 Introduction	1
1.1.2 Motivation and Purpose.....	3
1.2 General Background and Literature Review	5
1.2.1 Battery Fundamentals	5
1.2.2 Aqueous and Non-aqueous Zn-ion Batteries.....	7
1.2.3 Mechanism in Zinc-ion Batteries	13
1.2.4 PBA Cathode Materials for Zn-ion Batteries	19
1.3 Experimental Section	36
1.3.1 Materials	36
1.3.2 Synthesis of Sodium Manganese Hexacyanoferrate (NMHCF)....	37
1.3.3 Preparation of Zn/ NMHCF Cells	38
1.3.4 Materials Characterization.....	39
1.4 Results and Discussion.....	42
1.4.1 Materials Characterization.....	42
1.4.2 Material Morphology.....	48
1.4.3 Electrochemical Investigation	49

เอกสารนี้เป็นเอกสารที่สงวนไว้สำหรับการใช้งานเพื่อการศึกษานั้น ไม่อนุญาตให้นำไปใช้ประโยชน์ด้านการค้า
ไม่ว่ากรณีใดๆ ทั้งสิ้น อีกทั้งห้ามมิให้ดัดแปลงเนื้อหา และต้องอ้างอิงถึงเจ้าของเอกสารทุกครั้งที่มีการนำไปใช้

TABLE OF CONTENTS

(Continued)

Chapter	Page
1.4.4 Mechanistic Study	51
1.5 Conclusion	58
Chapter 2 Eco-friendly Extraction of Lignin	59
2.1 Introduction and Research Motivation	59
2.1.1 Introduction	59
2.1.2 Research Motivation	61
2.2 General Background and Literature Review	64
2.2.1 Lignocellulose Biomass	64
2.2.2 Separation Methods of Lignin from Wood	67
2.2.3 Techniques for Characterizing Lignin	71
2.2.4 Effect of Microwave on Biomass	74
2.2.5 Microwave Heating of Organic Solvents	75
2.2.6 Softwood and Hardwood	77
2.2.7 Rubber Tree	78
2.2.8 Literature Review	79
2.3 Methodology	81
2.3.1 Materials	81
2.3.2 Solvent Extraction with Microwave-Assisted Method	81
2.3.3 Klason Lignin Analytical Method	82
2.3.4 Ultraviolet-Visible Spectrophotometry (UV-vis) Analytical Method	83

เอกสารนี้เป็นเอกสารที่สงวนไว้สำหรับการใช้งานเพื่อการศึกษาเท่านั้น ไม่อนุญาตให้นำไปใช้ประโยชน์ด้านการค้า
ไม่ว่ากรณีใดๆ ทั้งสิ้น อีกทั้งห้ามมิให้ดัดแปลงเนื้อหา และต้องอ้างอิงถึงเจ้าของเอกสารทุกครั้งที่มีการนำไปใช้

TABLE OF CONTENTS

(Continued)

Chapter	Page
2.3.5 Characterization Method Using Fourier Transform Infrared Spectroscopy (FT-IR)	84
2.3.6 Heteronuclear Single Quantum Coherence Spectroscopy (2D HSQC NMR) Characterization Method	84
2.3.7 Bomb Calorimeter Characterization Method	85
2.4 Results and Discussion	86
2.4.1 Microwave-Assisted Extraction of Lignin	86
2.4.2 Analysis Using Fourier Transform Infrared Spectroscopy (FT-IR)..	88
2.4.3 Analysis Using Heteronuclear Single Quantum Coherence Spectroscopy (2D HSQC NMR).....	91
2.4.4 Ultraviolet-Visible Spectrophotometry (UV-vis) Analysis.....	94
2.4.5 Higher Heating Value (HHV) Characterization	95
2.5 Conclusion	97
REFERENCES	98
AUTHOR BIOGRAPHY.....	116

เอกสารนี้เป็นเอกสารที่สงวนไว้สำหรับการใช้งานเพื่อการศึกษาเท่านั้น ไม่อนุญาตให้นำไปใช้ประโยชน์ด้านการค้า
ไม่ว่ากรณีใดๆ ทั้งสิ้น อีกทั้งห้ามมิให้ดัดแปลงเนื้อหา และต้องอ้างอิงถึงเจ้าของเอกสารทุกครั้งที่มีการนำไปใช้

LIST OF TABLES

Table	Page
Table 1.1 Literature Review on cathode Materials for ZIBs.....	23
Table 1.2 Chemicals Used in This Work.	36
Table 1.3 Estimated Parameters of Equivalent Circuit Models for Zn/NMHCF Cells.	57
Table 2.1 The Proportion of Lignin Monomers in Woods and Herbaceous Plants. ...	67
Table 2.2 Chemicals Used In this Work.	81
Table 2.3 The Assignment of FT-IR Bands.	91
Table 2.4 The Assignment of Main Signals in the 2D HSQC NMR Spectra of Lignin.	93

LIST OF FIGURES

Figure	Page
Figure 1.1 Schematic diagram of battery working principle.	7
Figure 1.2 The plot between working voltage and specific capacity for Zn metal anode and various cathode materials presently used for aqueous ZIBs.	9
Figure 1.3 Full Zn/NVPOF battery. (a) Rietveld refined XRD patterns of the as-prepared $\text{Na}_3\text{V}_2(\text{PO}_4)_2\text{O}_2\text{F}$. (b) CV curves of $\text{Na}_3\text{V}_2(\text{PO}_4)_2\text{O}_2\text{F}$ in dual electrolyte. (c) Cycling performance in different electrolytes (0.2C). (d) charge/discharge profile (0.2C) and (e) cycling performance (1.0C).	11
Figure 1.4 Schematic diagram of ion insertion/extraction in VPO_4F cathode.	12
Figure 1.5 Coulombic efficiencies of NiHCF cathode in various electrolytes for ZIBs.	13
Figure 1.6 Schematic diagram of Zn-ion insertion mechanism in $\gamma\text{-MnO}_2$	14
Figure 1.7 (a–c) TEM/HRTEM images of $\alpha\text{-MnO}_2$ electrode after discharge; (e–g) TEM/HRTEM images of $\alpha\text{-MnO}_2$ electrode after charge.	15
Figure 1.8 Galvanostatic intermittent titration technique (GITT) curve of the Zn/Akhtenskite-type MnO_2 cell.	16
Figure 1.9 (a) Schematic diagram of hybrid-metal ion (de)intercalation mechanism. (b) <i>In-situ</i> XRD patterns of LiMn_2O_4 cathode during the first cycle. (c) <i>Ex-situ</i> XRD patterns of Zn anode.	17
Figure 1.10 Schematic diagram of Zn–graphite battery during discharge.	19
Figure 1.11 The schematic structure of ideal NMHCF.	20
Figure 1.12 <i>Operando</i> XRD patterns of a CuHCF/Zn cell during charge/discharge.	22
Figure 1.13 Schematic diagram of co-precipitation with citrate-assisted method.	43

LIST OF FIGURES

(Continued)

Figure	Page
Figure 1.14 TGA of as-prepared NMHCF.....	44
Figure 1.15 PXRD patterns of NMHCF from this work and monoclinic PBA.....	45
Figure 1.16 Le Bail refinement of synchrotron X-ray diffraction (SXRD) pattern of NMHCF in P21/n, $wRp = 5.43\%$: $a = 10.55 \text{ \AA}$, $b = 7.48 \text{ \AA}$, $c = 7.42 \text{ \AA}$, and $\beta = 91.93^\circ$ (measured, orange; calculated, green; difference, pink; Bragg reflections, vertical tick marks).....	45
Figure 1.17 Raman spectrum of NMHCF.....	46
Figure 1.18 FT-IR of as-prepared NMHCF sample.....	47
Figure 1.19 (a,b) SEM and (b) TEM images of NMHCF at different magnifications (d,e) HRTEM images with d-spacing 0.375 and 0.536 nm indicating $(-2-1-1)$ and (011) planes and (f) SAED pattern of NMHCF.....	49
Figure 1.20 Electrochemical performance of the NMHCF a) Charge/discharge profile of the first cycle at 30 mA g^{-1} . b) Charge/discharge profile of the first cycle at various current densities. c) Cyclic voltammogram of NMHCF. d) Cycling performance at various current densities for 100 cycles.....	51
Figure 1.21 <i>Ex-situ</i> XRD patterns of NMHCF electrode at different states-of-charge: starting from (pristine) initial state charged up to 1.7 V and 2.0 V, and discharged back to 0.3 V.....	53
Figure 1.22 STEM images and elemental mapping of NMHCF particles at different states of charge, OCV, 2.0 V, and 0.3 V.....	54
Figure 1.23 <i>Ex-situ</i> XANES spectra and (a) corresponding voltage profile of (b) Fe K-edge and (c) Mn K-edge.	55

LIST OF FIGURES

(Continued)

Figure	Page
Figure 1.24 (a) The electrochemical impedance spectra of NMHCF electrodes at different states of charge, and b) the corresponding equivalent circuit.	57
Figure 2.1 The fundamental unit of cellulose.	65
Figure 2.2 Monomers in lignin.	66
Figure 2.3 Several typical linkages within the lignin molecule.	66
Figure 2.4 Ultraviolet spectra of (1) pine kraft lignin in 2-methoxyethanol/water (8:2, v/v), (2) spruce liginosulfonate in water, and (3) milled wood lignin in 95% ethanol.	72
Figure 2.5 FT-IR spectrum of a softwood kraft lignin derived from ponderosa pine.	73
Figure 2.6 Ionic conduction and dipolar polarization under microwave conditions.	77
Figure 2.7 Schematic diagram of the modified microwave oven.	82
Figure 2.8 The percentage yield of extracted lignin.	87
Figure 2.9 FT-IR spectra of lignin obtained through the organosolv method, Klason lignin, and solvents extraction using the microwave-assisted method.	89
Figure 2.10 HSQC spectra ($\delta C/\delta H$ 50–95/2.0–5.5) of (a) extracted lignin solutions using ethanol, (b) extracted lignin solutions using isopropanol, (c) Klason lignin, and (d) organosolv lignin.	92
Figure 2.11 UV-visible spectra of the experimental lignins and Klason lignin.	94
Figure 2.12 The higher heating value (HHV) of the extracted solutions compared to pure solvents.	96

CHAPTER 1

LOW-COST ROBUST ZINC-ION BATTERY CATHODE

This work is based on a published article: Yimtrakarn, T.; Liao, Y.-C.; MV, A. S.; Chen, J.-L.; Chuang, Y.-C., Lerkkasemsan, N.; Kaveevivitchai, W. "Mn-Fe Prussian Blue Analogue as Low-Cost Robust Cathode for Non-Aqueous Zn-Ion Batteries", Mater. Today Commun. 2023, 34, 105231.

1.1 Introduction and Research Motivation

1.1.1 Introduction

Electrical Energy Storage (EES) has apparently become a crucial feature of our daily lives due to our technology-driven society. The rapidly increasing demand for performance and cost effective EES units is a result of the increasing need for renewable energy sources, such as geothermal, ocean, solar, and wind energy, to reduce global warming and environmental deterioration. While Li-ion batteries (LIBs) have demonstrated excellent electrochemical characteristics, such as outstanding specific capacity, high working voltage, and long cycle life, there are concerns about their safety, cost, environmental impact, and limited lithium resources in the earth's crust. As a result, researchers are looking into a substitute for LIBs known as post-Li-ion batteries (PLIBs). Zinc metal anode, with many benefits including natural abundance, low cost, high gravimetric and volumetric capacities, and safety, can be used in Zn-based batteries which are one of the most promising PLIBs.[1]

Zinc-ion batteries (ZIBs) are one of the up-and-coming choices for large-scale energy storage applications, especially due to the environmental benignity and two-electron transfer capability. Most research on Zn-based batteries has been focused on aqueous electrolyte systems, which have high ionic conductivity, low cost, and relatively high safety.[2,3] However, these systems have limitations, including corrosion, memory effects,[4] H₂/O₂ evolution,[5] and limitation in the electrochemical potential window of water.[6] To overcome these challenges, non-aqueous electrolyte systems have gained more attention as they allow for higher operating voltage and potentially higher energy and power density. While aqueous ZIBs have shown promise in certain applications, such as grid-scale energy storage, their limitations in terms of energy density and safety have led researchers to explore the potential benefits of non-aqueous ZIBs, which could offer improved performance and stability. However, due to the high charge density and strong electrostatic interactions with the host lattice, the intercalation of divalent ions into host materials is kinetically hindered.[4,7-9] Therefore, it is still necessary to discover appropriate cathode materials for high-performance organic-based ZIBs.

Nanosized materials and open-tunnel structures/layered compounds may help alleviate the kinetic problems by decreasing diffusion pathways and facilitating the insertion/extraction of guest ions. The structural stability of the host is also an important aspect to consider for the intercalation of multivalent guest ions. As the insertion of Zn²⁺ ions takes place, a shift in the oxidation state of the transition metal ions may lead to significant local distortion of the host structure.[10]

Prussian blue and its analogues (PBAs) are among the potential cathode materials for divalent-ion batteries. These compounds often have multiple distinct redox centers, each of which can carry out a full electrochemical redox reaction and offer a capacity for two-electron transfer. Moreover, with the tunability of the PBAs, it has become one of the most promising cathode materials for ZIBs. PBAs have proven to be potential cathode materials for sodium-ion batteries.[11,12] However, research on non-aqueous ZIBs is still rare.

1.1.2 Motivation and Purpose

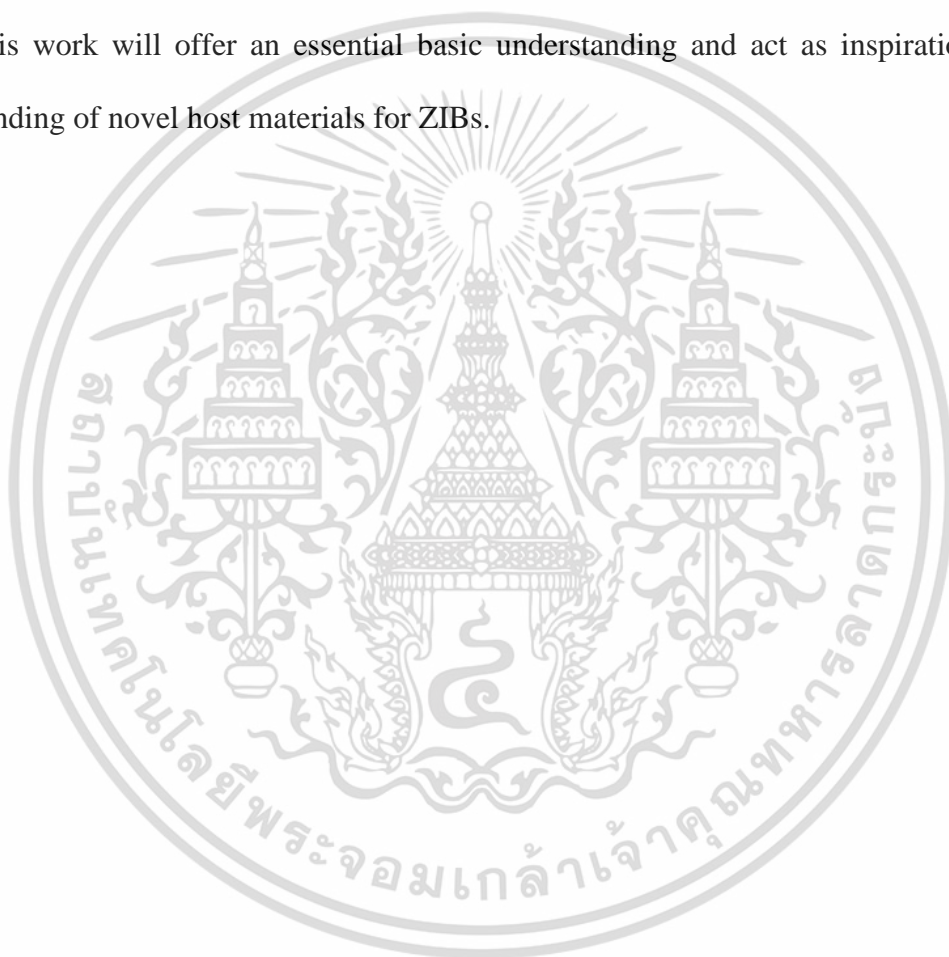
Energy storage is a critical component of renewable energy systems. It provides reliable and stable power to the user by integration with the energy generators. Many developed countries realize the crucial part of energy storage in achieving their renewable energy goals. They are investing in research and development to improve energy storage technology.

As discussed in the introduction, efficient large-scale energy storage systems are essential in maximizing the potential of renewable energy from various sources. Although LIBs are a prevalent option, their limitations have made it necessary to investigate alternative options. PLIBs could be a solution to these limitations. Among the possible options, zinc is considered one of the best candidates for next-generation large-scale ESS due to its low cost and environmental friendliness.

Aqueous electrolyte systems have received a lot of attention in the current literature on ZIBs. Finding suitable organic electrolytes and relevant host materials are challenging topics. Several cathode materials for non-aqueous ZIBs have been reported

in Mn-based and V-based, but there are still some significant shortcomings, such as low operating voltage and insufficient specific capacity.

Therefore, this research work focuses on PBAs as electrode material for non-aqueous ZIBs. Several characterization techniques were used to gain a deeper understanding of the electrochemical intercalation of guest ions into the PBAs lattice. To assist the objective of reducing the use of fossil and nuclear power, it is hoped that this work will offer an essential basic understanding and act as inspiration for the finding of novel host materials for ZIBs.



เอกสารนี้เป็นเอกสารที่สงวนไว้สำหรับการใช้งานเพื่อการศึกษาเท่านั้น ไม่อนุญาตให้นำไปใช้ประโยชน์ด้านการค้า
ไม่ว่ากรณีใดๆ ทั้งสิ้น อีกทั้งห้ามมิให้ดัดแปลงเนื้อหา และต้องอ้างอิงถึงเจ้าของเอกสารทุกครั้งที่มีการนำไปใช้

1.2 General Background and Literature Review

1.2.1 Battery Fundamentals

It is unrefusable that rechargeable batteries play a crucial role in our daily lives. They are serving as the backbone for various electronic devices, electric vehicles, and renewable energy systems. The working principles of batteries are based on the conversion of chemical energy into electrical energy through an electrochemical reaction. In this reaction, two electrodes (positive and negative) are separated by an electrolyte solution, and an electric current is generated when an electrical charge is transferred between the two electrodes.[13]

(1) Definitions

Battery: A device that converts chemical energy into electrical energy and stores it for later use.

Primary battery: A type of battery that cannot be recharged once its energy is exhausted.

Secondary battery: A type of battery that can be recharged after its energy is exhausted.

Charge: The process in which energy is given to a battery to restore the original charged state.

Discharge: The process of releasing current or energy from a battery.

Anode: The electrode in a battery or an electrochemical cell where oxidation takes place.

Cathode: The electrode in a battery or an electrochemical cell where reduction takes place.

Active material: The chemical substances in a battery that have redox-active sites and are responsible for providing useful electrical energy.

Electrolyte: A salt solution with either water or other solvents that provides ionic conductivity across the electrodes in an electrochemical cell.

Separator: A material that physically separates the anode and cathode in a battery, while allowing the flow of ions between them.

Open circuit voltage (OCV): The voltage of a battery or an electrical device when it is not connected to a circuit.

Closed circuit voltage: The voltage of a battery or an electrical device when it is connected to a circuit.

Faraday's constant: The amount of electrical charge carried by one mole of electrons, equal to approximately 96,485 coulombs per mole.

(2) Working Principles

Batteries are composed of three main components: a negative electrode, a positive electrode, and an electrolyte solution (**Figure 1.1**). In a rechargeable battery or secondary battery, the electrochemical reaction is reversible. There is current flowing from the external circuit, through the electrodes and the electrolyte solution. When a battery is in use or discharging, an oxidation reaction happens at the anode, releasing electrons into the external circuit to reach the cathode. After receiving the electrons, the cathode material is reduced. During charge, the process is reversed. The electrolyte solution is used to facilitate ion transport between the electrodes to balance the charge in the battery.

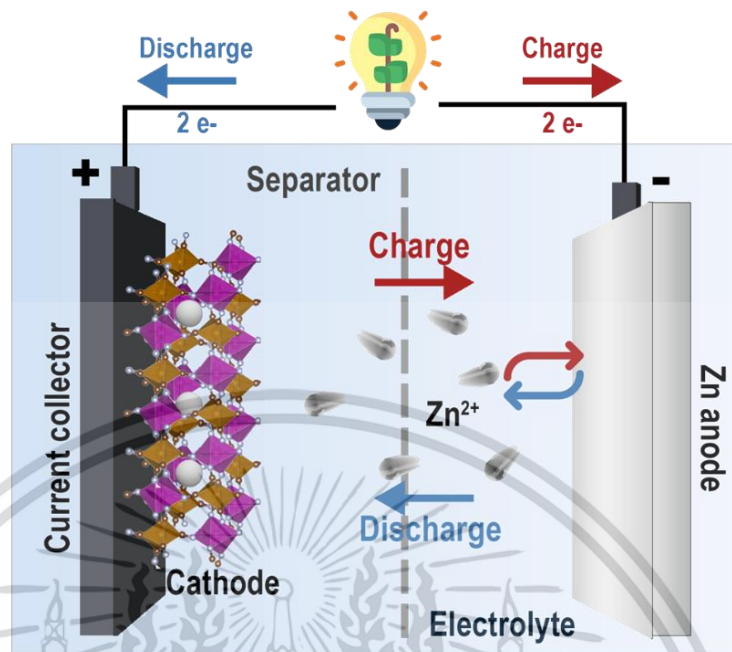


Figure 1.1 Schematic diagram of battery working principle.

1.2.2 Aqueous and Non-aqueous Zn-ion Batteries

ZIBs have several advantages over potassium, lithium, or sodium ion batteries, such as stability toward oxygen and moisture. ZIBs are also able to operate with aqueous and non-aqueous electrolytes. More recent attention has been focused on the provision of aqueous ZIBs due to their safety, high ionic conductivity, and inexpensiveness.[10,14-16] The study for organic solvents or non-aqueous ZIB electrolytes has been relatively understudied. Nevertheless, the organic electrolyte is comparatively more beneficial than the traditional aqueous electrolyte. In some research, the non-aqueous electrolyte showed higher reversibility of redox processes in electrode materials, ability to avoid zinc passivation, and stable Zn plating and stripping.[17,18]

(1) Aqueous Zn-ion Batteries

Aqueous ZIBs utilize a water-based electrolyte solution, which allows for high ionic conductivity and stable chemical properties. The use of a water-based electrolyte also eliminates the risk of thermal runaway, a common issue in non-aqueous batteries. Aqueous ZIBs show promising results for grid-scale energy storage systems, as the aqueous electrolyte enables high capacity, low-cost, and safe operation. However, the main disadvantage of aqueous ZIBs is their limited operating voltage, which limits their application in high-power devices.[19]

In recent years, there has been an increasing amount of literature on aqueous ZIBs, including those with zinc metal anode,[17,20] and cathode materials, such as, vanadium oxides,[21,22] manganese oxides,[23-25] NASICON structures,[26,27] organic compounds,[28,29] and PBAs.[14,18]

The literature on aqueous ZIBs has highlighted energy storage mechanisms (**Figure 1.2**). There are three main mechanisms, (1) insertion/extraction of Zn^{2+} , (2) chemical conversion reaction, and (3) co-insertion/extraction of H^+/Zn^{2+} . [30] Detailed studies have been performed to gain deep understanding of the battery components. The pros and cons of the Zn anode, optimum electrolytes, different cathode types, and optimization techniques aimed at high-performance aqueous ZIBs have been addressed.

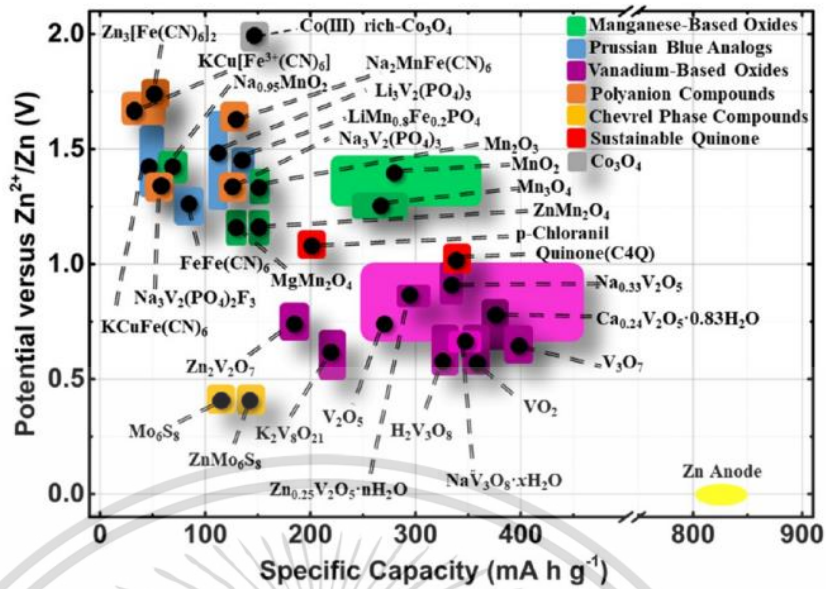


Figure 1.2 The plot between working voltage and specific capacity for Zn metal anode and various cathode materials presently used for aqueous ZIBs.[30]

(2) Non-aqueous Zn-ion Batteries

In the past decade, ZIBs have evolved as a feasible LIB alternative. They typically assembled with aqueous electrolytes. However, there are always interactions between the metallic Zn anode and the aqueous electrolyte, leading to issues of dendrites on the zinc anode.[31,32] One of the best adequate strategies is to eliminate or reduce the use of water in the electrolytes. Numerous studies have attempted to use alternative non-aqueous electrolytes. Early examples of research into non-aqueous electrolytes include aqueous/organic hybrid,[33,34] highly concentrated,[31,35] gel,[36] solid-state,[37] or even non-aqueous electrolytes.[1,4,7] Moreover, non-aqueous ZIBs show comparative capacity and long-term stability, which make them a promising option for portable electronic devices.

In 2016, Albert L. et al. demonstrated the use of an electrolyte, 0.5 M Zn(TFSI)₂ in acetonitrile, for NiHCF cathode material. The results confirmed that the non-aqueous electrolyte provided high ion insertion potential and low overvoltage. This electrolyte also allows wide voltage window for ZIBs in the range of 0.3 V to 2.0 V.[38]

To overcome the limitations of the aqueous electrolytes, Pan C. and co-workers used a non-aqueous electrolyte, a 0.3 M solution of Zn(OTf)₂ in acetonitrile, for ZnAl_xCo_{2-x}O₄ cathode in ZIBs. This cathode showed high OCV up to 1.95 V which indicates the possibility for high voltage ZIBs.[1]

Dong Y. et al. (2020) investigated the impact of dual and single cations in triethyl phosphate electrolytes. They found that the dual-cation (Na⁺ and Zn²⁺) electrolyte delivered a long-life span with 16.5% capacity fading over 1000 cycles (**Figure 1.3**). The polyanion-type electrode material, Na₃V₂(PO₄)₂O₂F, showed high output voltage as high as 1.8 V with non-aqueous electrolyte which can compatibly support the board voltage window.[39]

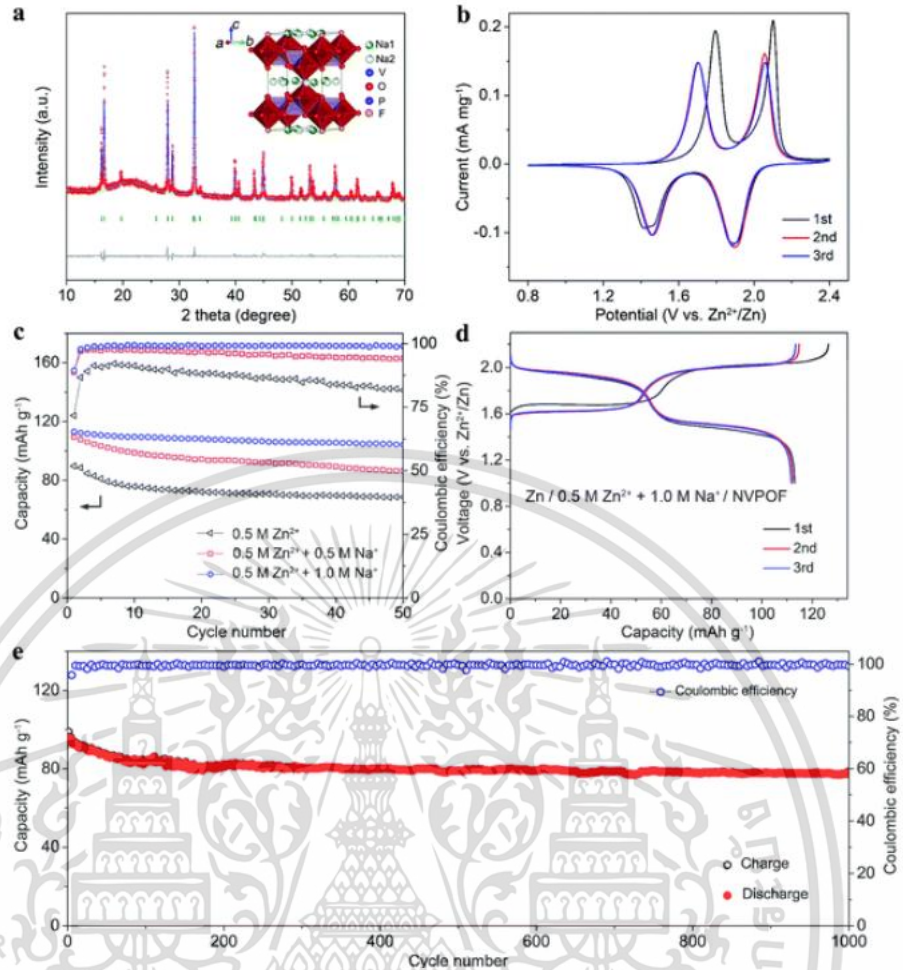


Figure 1.3 Full Zn/NVPOF battery. (a) Rietveld refined XRD patterns of the as-prepared $\text{Na}_3\text{V}_2(\text{PO}_4)_2\text{O}_2\text{F}$. (b) CV curves of $\text{Na}_3\text{V}_2(\text{PO}_4)_2\text{O}_2\text{F}$ in dual electrolyte. (c) Cycling performance in different electrolytes (0.2C). (d) charge/discharge profile (0.2C) and (e) cycling performance (1.0C).[39]

Yaghoobnejad et al. (2020) highlighted that the redox chemistry in the Zn- VPO_4F system relies on water to facilitate the redox process through the H^+ intermediate (**Figure 1.4**). Using aqueous electrolytes, however, may result in cathode-electrolyte dissolution, which eventually causes capacity decrease and early cell death. Therefore, researchers should consider exploring non-aqueous electrolytes as alternative solutions.[40]

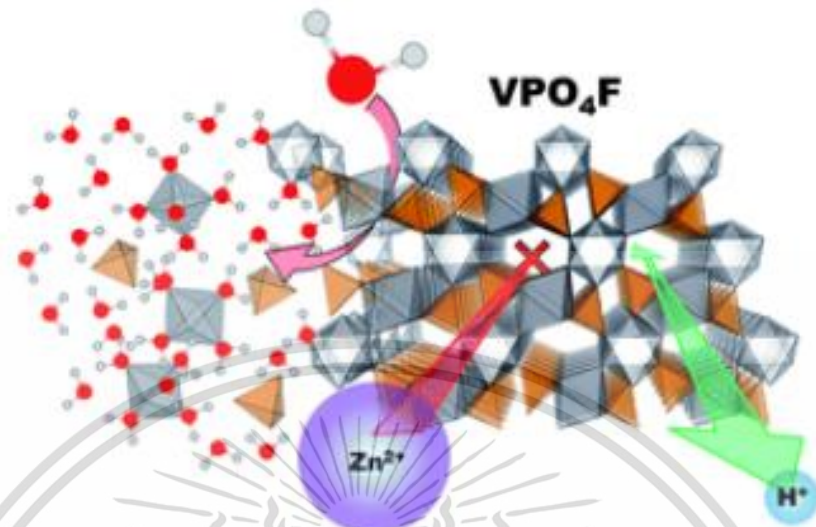


Figure 1.4 Schematic diagram of ion insertion/extraction in VPO₄F cathode.[40]

Preliminary work on organic electrolytes in NiHCF was undertaken by M.S. Chae et al. (2017). They showed the compatibility of the material with an electrolyte, 0.5 M zinc perchlorate in acetonitrile, in ZIBs. The results were confirmed by high stability with 99.9% of Coulombic efficiency for 20 cycles (**Figure 1.5**).[4]

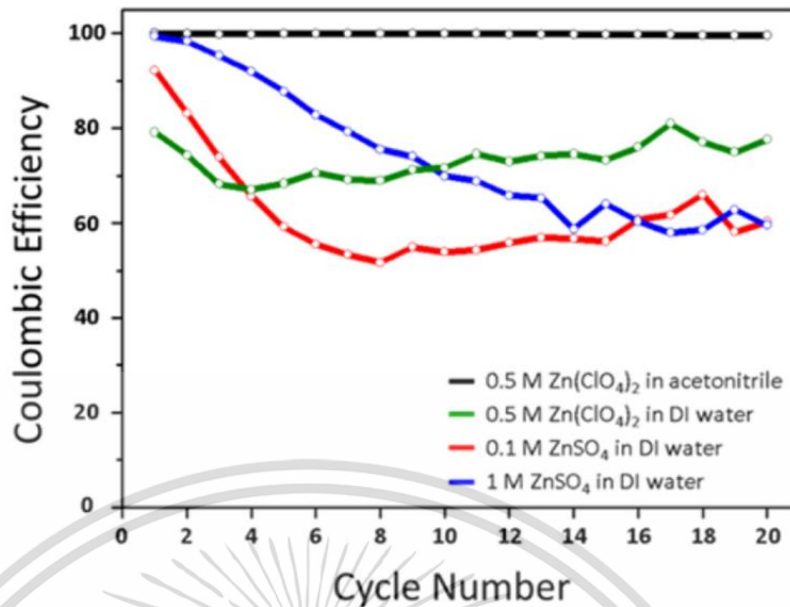


Figure 1.5 Coulombic efficiencies of NiHCF cathode in various electrolytes for ZIBs.[4]

1.2.3 Mechanism in Zinc-ion Batteries

Depending on the cathode type, several energy storage mechanisms are known in ZIBs. Zn^{2+} deintercalation/intercalation, conversion reaction, proton- Zn^{2+} co-insertion, hybrid-metal ion deintercalation/intercalation, ion-coordination, and anion deintercalation/intercalation are the primary types of reaction processes for ZIBs that have been proposed so far.

(1) Zn^{2+} Deintercalation/Intercalation

This process involves the transport of zinc ions within the ZIBs. During charge, Zn^{2+} ions are deintercalated out of the positive electrode, and during discharge, ions are intercalated into the positive electrode. Zinc ion has a smaller ionic radius (0.72 Å) compared to lithium ion (0.76 Å).[41] The small size of zinc ion is beneficial during

ion (de)intercalation into (from) the host structure (**Figure 1.6**). This mechanism is the most basic phenomenon with electrolyte between the two electrodes providing ionic conductivity and anode as a zinc ion source. Early examples of research into Zn^{2+} deintercalation/intercalation include $ZnNi_xMn_xCo_{2-2x}O_4$ spinel,[7] $V_2(PO_4)_3$,[17] VO_2 ,[21] etc.

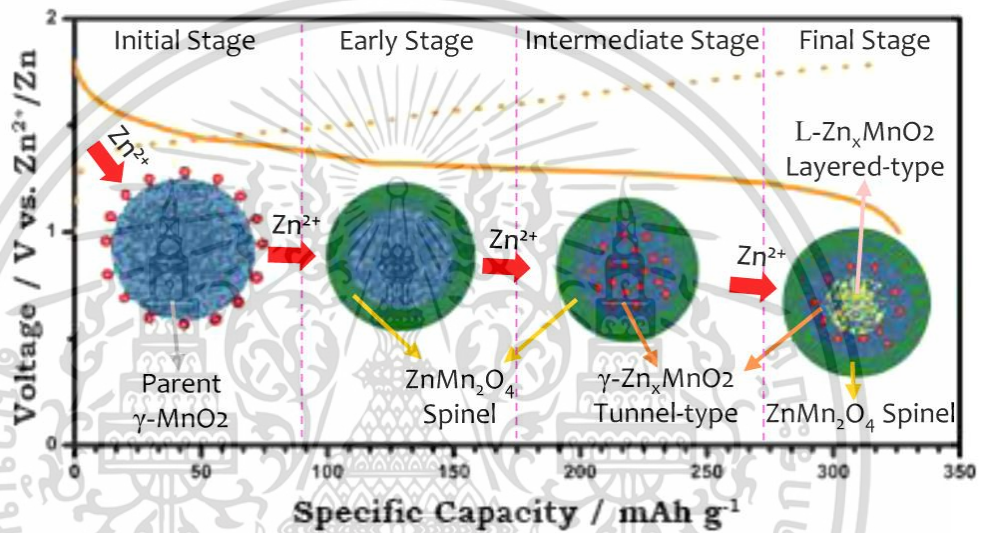


Figure 1.6 Schematic diagram of Zn-ion insertion mechanism in γ - MnO_2 . [42]

(2) Conversion Reaction

Conversion reaction refers to the chemical transformation of the electrode material during the charge/discharge processes. For example, in the cathode of ZIBs, the electrode material undergoes reaction to form a new compound. Liu et al. demonstrated a reversible conversion reaction of MnO_2 cathode in water-based ZIBs, which involves the conversion reaction between H^+ and MnO_2 (**Figure 1.7a–g**). [13] The discharge process results in the formation of a new $MnOOH$ ($MnO_2 + H^+ + e^- \leftrightarrow$

$MnOOH$). Subsequently, OH^- ion reacts with salt ($ZnSO_4$) and water in the electrolyte,

เอกสารนี้เป็นเอกสารที่สงวนไว้สำหรับการใช้งานเพื่อการศึกษา 14 เท่านั้น ไม่อนุญาตให้นำไปใช้ประโยชน์ด้านการค้า
ไม่ว่ากรณีใดๆ ทั้งสิ้น อีกทั้งห้ามมิให้ดัดแปลงเนื้อหา และต้องอ้างอิงถึงเจ้าของเอกสารทุกครั้งที่มีการนำไปใช้

leading to the generation of zinc hydroxide sulfate hydrates ($\text{ZnSO}_4[\text{Zn}(\text{OH})_2]_3 \cdot x\text{H}_2\text{O}$) to maintain the neutralized charge in the electrolyte system. This conversion reaction was confirmed through various analytical techniques, including XRD, TEM, and STEM-EDS mapping.[43]

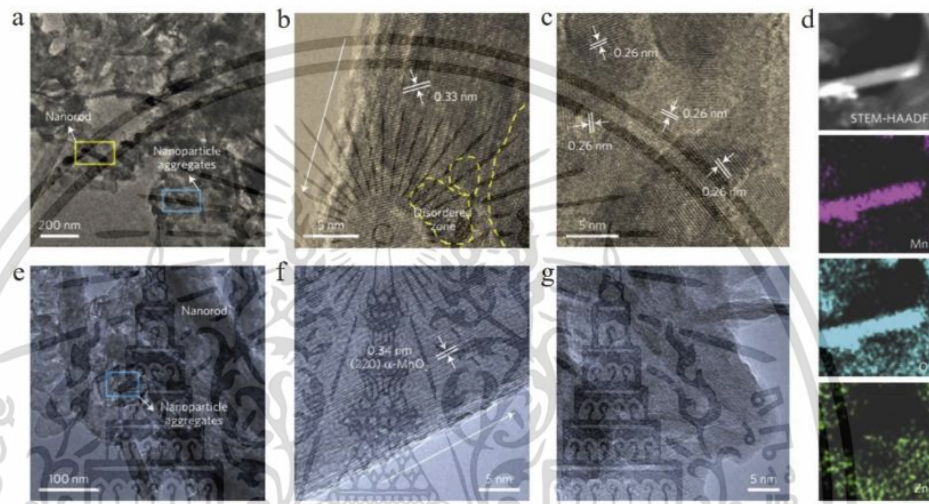


Figure 1.7 (a–c) TEM/HRTEM images of $\alpha\text{-MnO}_2$ electrode after discharge; (e–g) TEM/HRTEM images of $\alpha\text{-MnO}_2$ electrode after charge.[43]

(3) Proton and Zn^{2+} Co-insertion

Co-insertion involves the simultaneous insertion of both protons and zinc ions into the electrode. This reaction requires protons which are generally conducted in an aqueous system.

The study of the co-insertion of proton and Zn^{2+} was first carried out by Wang et al. (2017).[44] They used the galvanostatic intermittent titration technique (GITT) to investigate the ion insertion in Akhtenskite-type MnO_2 cathode material in aqueous

ZIBs (**Figure 1.8**). Faster insertion kinetics is made possible by the proton which is smaller in size and has weaker electrostatic interaction compared to Zn^{2+} . As a result, the GITT curves significantly differ, with the proton insertion process delivering a far lower overvoltage at the first discharge plateau than zinc-ion insertion process at the second plateau.

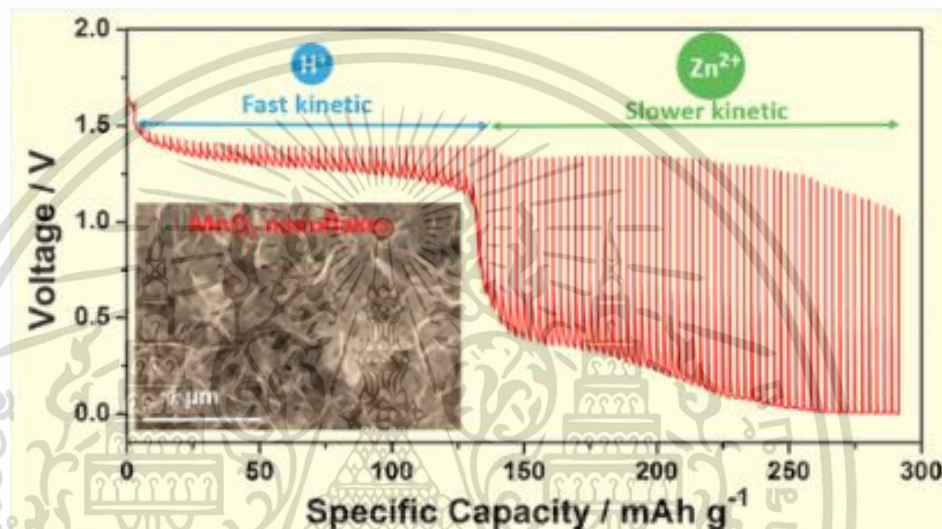


Figure 1.8 Galvanostatic intermittent titration technique (GITT) curve of the Zn/Akhtenskite-type MnO_2 cell.[44]

(4) Hybrid-metal-ion Deintercalation/Intercalation

The reaction involves the incorporation of multiple metal ions in the ZIBs system. ZIBs have recently been developed with hybrid designs, which link a metallic Zn anode and a lithium- or sodium-based intercalation cathode to form a new class of aqueous energy storage systems.

Yan et al. successfully applied LiMn_2O_4 as a cathode for ZIBs opening up a new potential pathway for the hybrid-metal-ion energy storage mechanism (**Figure 1.9**),[45]

in which the anode underwent reversible Zn deposition and the cathode underwent reversible Li^+ ion (de)intercalation. The hybrid-metal-ion (de)intercalation between the cathode and Zn anode can be expressed as:

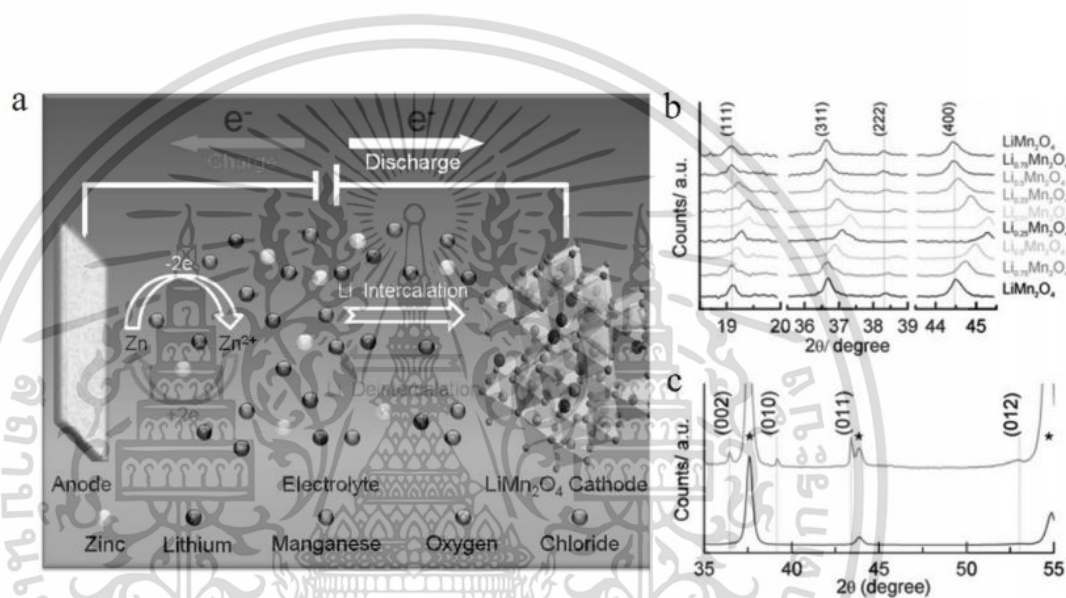
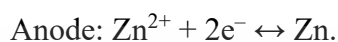


Figure 1.9 (a) Schematic diagram of hybrid-metal ion (de)intercalation mechanism. (b) *In-situ* XRD patterns of LiMn_2O_4 cathode during the first cycle. (c) *Ex-situ* XRD patterns of Zn anode.[45]

(5) Ion-coordination

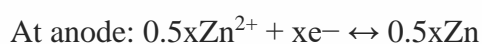
Organic molecules have received recent attention due to their property tunability, flexible structures, and high sustainability. Moreover, the functional groups, such as carbonyl and imine groups, can interact with guest ions with high reversibility.

Zhao et al.[29] highlighted the use of a small organic cathode (quinone) for ZIBs in an aqueous system. The cathode delivered a high capacity and high reversibility with 13% capacity fade at 500 mA g⁻¹ after 1000 cycles. These reactions in organic material are different from inorganic materials where it is possible for zinc ions to coordinate with electronegative oxygen atoms. Luu et al.[28] found a 2D small-molecule with π - π stacking layers of organic cathode material (HATAQ) which is rich in nitrogen and carbonyl groups. It can facilitate divalent zinc ions and protons for ion coordination with the functional groups.

(6) Anion Deintercalation/Intercalation

This process involves the movement of anions (negatively charged ions) within the electrode material. Moreover, both cation and anion may play a role in the energy storage system of rechargeable ZIBs.

Zhang et al.[46] presented a graphite ZIBs composed of zinc metal as anode and graphite cathode in 1 M Zn(TFSI)₂ in acetonitrile solvent (**Figure 1.10**). It functioned by (de)intercalating the TFSI anion into (from) the graphite, as shown in the equation below, and electrochemically plating and stripping the zinc cation at the anode.



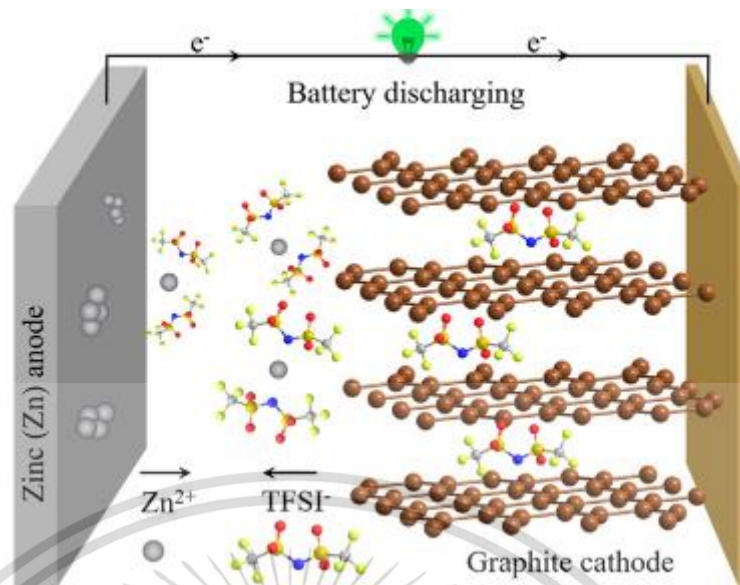


Figure 1.10 Schematic diagram of Zn–graphite battery during discharge.[46]

1.2.4 PBA Cathode Materials for Zn-ion Batteries

PBAs are typically formulated as $AM' [M''CN)_6]_n \cdot xH_2O$, where M' and M'' are divalent transition metals, such as Fe(II), Co(II), Ni(II), Cu(II), or Zn(II), or trivalent metal cations, such as Fe(III), Cr(III), or Al(III), and A is an alkali metal. The cyanide ligands (CN^-) bridge the two metal cations, forming a three-dimensional framework structure (**Figure 1.11**). This structure can be modified by incorporating other metal ions or functional groups into the framework, which can affect the properties of the PBAs and make them more suitable for specific applications. PBAs are potential materials for the positive electrode (cathode) of batteries that require two-electron transfer. PBAs are especially promising because the chemical compositions can be adjusted to optimize the performance in batteries.

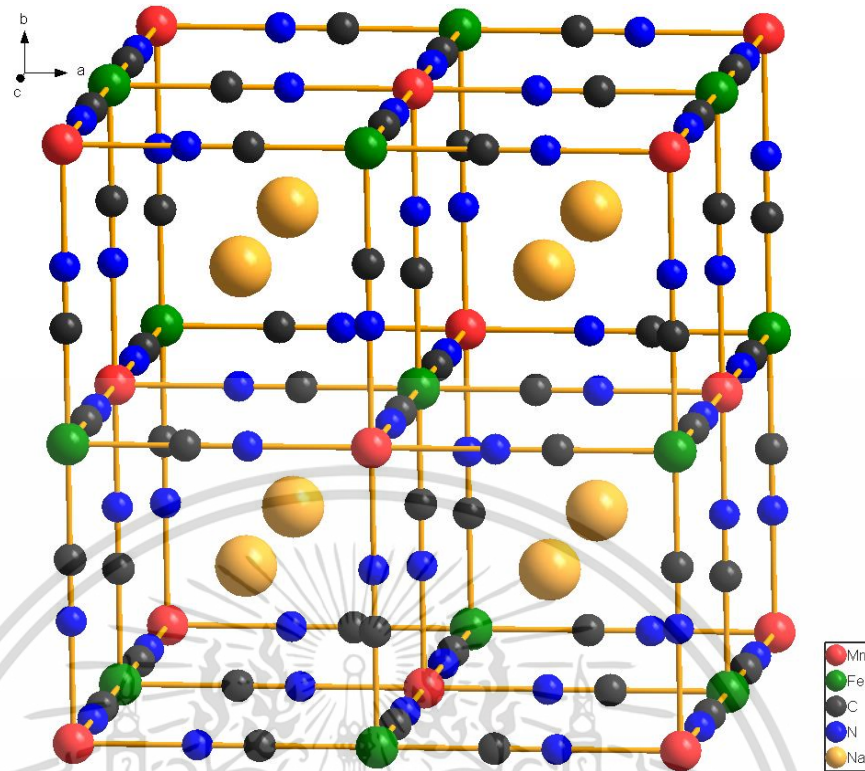


Figure 1.11 The schematic structure of ideal NMHCF.

In 2015, Liu et al. reported the first high working voltage beyond 1.5 V of aqueous ZIBs (1 M ZnSO_4) with ZnHCF (zinc hexacyanoferrate) cathode.[2] To determine the morphology-controlled effects of ZnHCF particles to improve and investigate the electrochemical performance, Liu et al.[3] compared the 3 different shapes of ZnHCF. They confirmed that the cubooctahedral shape of ZnHCF provided the acceptable capacity and retention. However, they found the dissolution issue of active material in the electrolyte.

CuHCF cathode in ZIBs was proposed by Mantia and co-workers.[14] CuHCF/Zn cells with aqueous electrolyte delivered high energy density up to 45.7 Wh kg^{-1} at 60 mA g^{-1} with excellent retention of 96.3% over 100 cycles. Two low-spin Fe^{3+} are concurrently transformed into low-spin Fe^{2+} when Zn^{2+} is inserted into the CuHCF

structure. In contrast, Kasiri et al.[47] showed one major trouble of the capacity fade which is related to the dissolution of active material (CuHCF). The phase transition of CuHCF causes active material dissolution. These results were confirmed by *operando* synchrotron XRD, and the phase changes in CuHCF were investigated by Renman et al.[48] which are related to zinc ion substitution into CuHCF host structure. **Figure 1.12**, *operando* XRD patterns of CuHCF/Zn during charge/discharge present peak shift to left and right during charge and discharge corresponding to unit cell parameter change. Chea et al.[4] utilized a PBAs cathode in a non-aqueous system. NiHCF and zinc metal are used as the ZIB positive and negative electrode materials, respectively. The organic electrolyte used in the battery was 0.5 M Zn(ClO₄)₂ in acetonitrile. The results show that the electrolyte provides higher stability compared to aqueous electrolytes. Nevertheless, this research provided a better understanding of zinc insertion in PBA structure under a non-aqueous system.

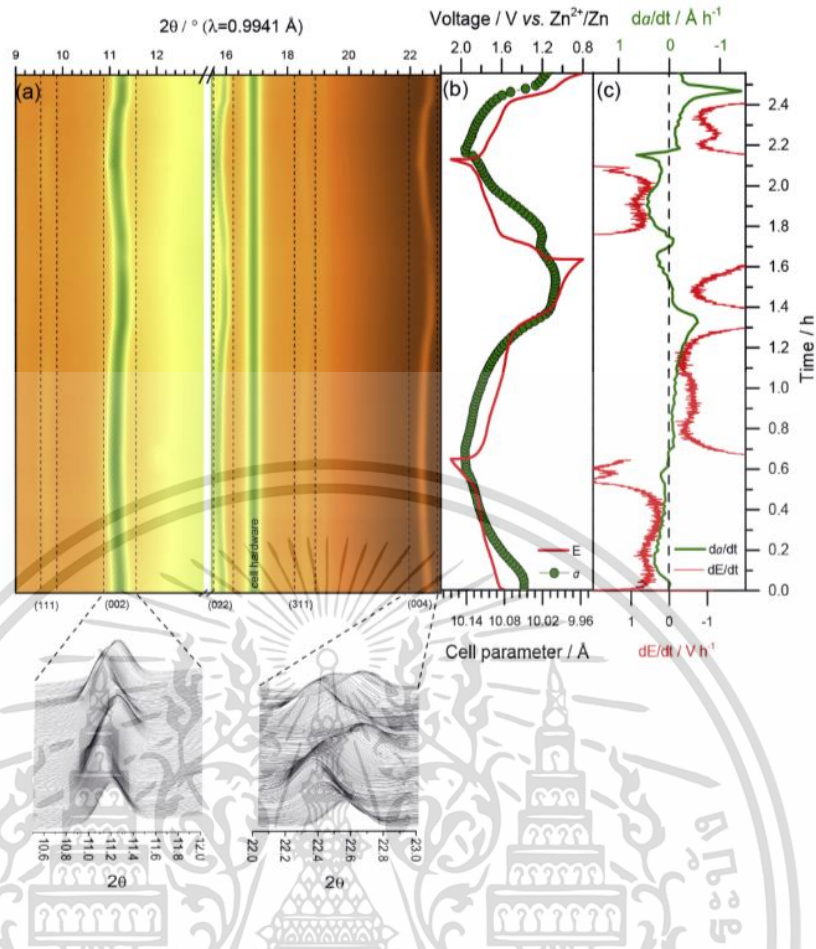


Figure 1.12 Operando XRD patterns of a CuHCF/Zn cell during charge/discharge.[48]

The manganese-iron PBA cathode is known for its low cost, making it an attractive alternative for developing low-cost ZIBs. In addition to its cost-effectiveness, the manganese-iron Prussian blue cathode also offers high stability and improved performance (2 redox-active sites) compared to traditional cathode materials. This has led to its increasing use in various applications, such as portable electronics and renewable energy storage systems.

Table 1.1 Literature Review on cathode Materials for ZIBs.

Compound	Electrode Composition†	Electrolyte	Voltage Window (V vs. Zn/Zn²⁺)	Average Working Voltage (V vs. Zn/Zn²⁺)	Initial Capacity at Lowest Rate Reported	Reversible Capacity at Highest Rate Reported	Ref.
Na _{1.2} Mn[Fe(CN) ₆] _{0.8} ·3H ₂ O	AM:Super P:Graphite KS4:PVDF (5:3:1:1)	0.2 M Zn(CF ₃ SO ₃) ₂ in 1:4 PC/DMSO	0.3–2.0	1.45	~89.5 mAh g ⁻¹ at 30 mA g ⁻¹	27.8 mAh g ⁻¹ at 820 mA g ⁻¹	This work
K _{1.64} Mn _{1.2} Fe(CN) ₆	AM:AB:PVDF (7:2:1)	2 M Zn(ClO ₄) ₂ in TEGDME	0.7–1.9	1.6	65.5 mAh g ⁻¹ at 50 mA g ⁻¹	62.0 mAh g ⁻¹ at 200 mA g ⁻¹	[49]
K _{0.78} Zn _{2.86} [Fe(CN) ₆] ₂ ·4.5H ₂ O	AM:AB:PVDF (6:3:1)	0.5 M KCF ₃ SO ₃ and 0.1 M Zn(CF ₃ SO ₃) ₂ in TEP	0.7–2.1	1.7	77 mAh g ⁻¹ at 50 mA g ⁻¹	~ 62 mAh g ⁻¹ at 2000 mA g ⁻¹ (47 mAh g ⁻¹ at 5000 mA g ⁻¹ for 6 cycles)*	[50]
K _{1.29} Ni[Fe(CN) ₆] _{0.821} ·2.64H ₂ O	AM:Super P: Graphite KS6:PVDF (8.0:0.9:0.2:0.9)	1 M Zn(ClO ₄) ₂ in AN	0.8–1.8	~1.2	60 mAh g ⁻¹ at 39 mA g ⁻¹	~52 mAh g ⁻¹ at 39 mA g ⁻¹	[51]

Compound	Electrode Composition†	Electrolyte	Voltage Window (V vs. Zn/Zn ²⁺)	Average Working Voltage (V vs. Zn/Zn ²⁺)	Initial Capacity at Lowest Rate Reported	Reversible Capacity at Highest Rate Reported	Ref.
$\text{K}_{0.86}\text{Ni}[\text{Fe}(\text{CN})_6]_{0.954} \cdot (\text{H}_2\text{O})_{0.766}$	AM:SuperP:PVDF (8:1:1)	0.5 M Zn(ClO ₄) ₂ in AN	0.7–1.8	~1.23	55.6 mAh g ⁻¹ at 11.2 mA g ⁻¹	~45 mAh g ⁻¹ at 11.2 mA g ⁻¹ (8 mAh g ⁻¹ at 224 mA g ⁻¹ for 6 cycles)*	[4]
$\text{Na}_{0.45}\text{NiFe}(\text{CN})_6$	AM:Super C45:PVDF (8:1:1)	0.5 M Zn(TFSI) ₂ in AN	0.3–2.0	~1.1	~62 mAh g ⁻¹ at 10 mA g ⁻¹	~67 mAh g ⁻¹ at 10 mA g ⁻¹	[38]
$\text{Na}_2\text{MnFe}(\text{CN})_6$	AM:Super P:PVDF (8:1:1)	0.5 M Zn(CF ₃ SO ₃) ₂ + 1 M NaFSI in TMP with 5% TTFP	1.0–2.2	~1.4	115 mAh g ⁻¹ at 80 mA g ⁻¹	77.2 mAh g ⁻¹ at 160 mA g ⁻¹ (20 mAh g ⁻¹ at 1600 mA g ⁻¹ for 10 cycles)*	[52]
$\text{ZnAl}_{0.656}\text{Co}_{1.344}\text{O}_4$	AM:Carbon black:PVDF (7:2:1)	0.3 M Zn (CF ₃ SO ₃) ₂ in AN	1.04–2.15	~1.7	134 mAh g ⁻¹ at 0.1C	~105.5 mAh g ⁻¹ at 1C (14.2 mAh g ⁻¹ at 10C for 5 cycles)*	[53]
$\text{ZnNi}_{0.5}\text{Mn}_{0.5}\text{CoO}_4$	AM:Carbon black:PVDF (7:2:1)	0.3 m Zn(CF ₃ SO ₃) ₂ in AN	0.80–2.15	1.8	180 mAh g ⁻¹ at 42 mA g ⁻¹	147 mAh g ⁻¹ at 42 mA g ⁻¹ (40 mAh g ⁻¹ at 10C for 5 cycles)*	[54]

Compound	Electrode Composition†	Electrolyte	Voltage Window (V vs. Zn/Zn ²⁺)	Average Working Voltage (V vs. Zn/Zn ²⁺)	Initial Capacity at Lowest Rate Reported	Reversible Capacity at Highest Rate Reported	Ref.
Zn _x Mo _{2.5+y} VO _{9+z} ; (x=1–3)	AM:Super P:PVDF (7.5:1.5:1.0)	0.2 M Zn(CF ₃ SO ₃) ₂ in 1:4 PC/DMSO	0.0–1.6	0.25	~220 mAh g ⁻¹ at 2 mA g ⁻¹	~200 mAh g ⁻¹ at 20 mA g ⁻¹	[55]
VPO ₄ F/C	AM:Super P:PVDF (7:1.5:1.5)	ZnCl ₂ - (NH ₂) ₂ CO ionic liquid	0.8–1.8	1.5	120 mAh g ⁻¹ at C/50	~112 mAh g ⁻¹ at C/50 (80 mAh g ⁻¹ at C/10 for 5 cycles)*	[40]
V ₂ (PO ₄) ₃	AM:Super P:PVDF (7.0:1.5:1.5)	0.3 M Zn(CF ₃ SO ₃) ₂ in PN	0.7–1.9	1.2	82 mAh g ⁻¹ at C/20	~19.5 mAh g ⁻¹ at C/5	[56]
Na ₃ V ₂ (PO ₄) ₂ O ₂ F	AM:Super P:CMC (8:1:1)	0.5 M Zn(CF ₃ SO ₃) ₂ and 1.0 M NaClO ₄ in TMP	1.0–2.2	1.8	126.5 mAh g ⁻¹ at 26 mA g ⁻¹	75 mAh g ⁻¹ at 130 mA g ⁻¹ (58 mAh g ⁻¹ at 260 mA g ⁻¹ for 5 cycles)*	[39]
Na ₃ V ₂ (PO ₄) ₃	AM:AB:PVDF (7:2:1)	1 M NaCF ₃ SO ₄ 0.1 M Zn(CF ₃ SO ₃) ₂ in TEP	0.6–1.8	1.3	84 mAh g ⁻¹ at 50 mA g ⁻¹	~74 mAh g ⁻¹ at 500 mA g ⁻¹ (54 mAh g ⁻¹ at 1000 mA g ⁻¹ for 5 cycles)*	[57]

Compound	Electrode Composition†	Electrolyte	Voltage Window (V vs. Zn/Zn ²⁺)	Average Working Voltage (V vs. Zn/Zn ²⁺)	Initial Capacity at Lowest Rate Reported	Reversible Capacity at Highest Rate Reported	Ref.
NVO nanoribbon/CFP	Electro-deposition	0.5 M ZnCl ₂ in ethaline (Deep eutectic electrolyte)	0.01–1.80	0.6	310 mAh g ⁻¹ at 100 mA g ⁻¹	167 mAh g ⁻¹ at 300 mA g ⁻¹ (118 mAh g ⁻¹ at 600 mA g ⁻¹ for 6 cycles)*	[58]
Carbon-Coated Zn ₂ Fe(PO ₄) ₂	AM:AB:CMC (7:2:1)	0.5 M Zn(TFSI) ₂ in AN	0.7–1.7	1.2	194 mAh g ⁻¹ at 20 mA g ⁻¹	178 mAh g ⁻¹ at 200 mA g ⁻¹ (150 mAh g ⁻¹ at 400 mA g ⁻¹ for 5 cycles)*	[59]
ZnMn ₂ (PO ₄) ₂ @C	AM:AB:CMC (7:2:1)	0.5 M Zn(TFSI) ₂ in AN	0.67–1.67	1.17	186 mAh g ⁻¹ at 0.05C	119 mAh g ⁻¹ at 0.1C (75 mAh g ⁻¹ at 2C for 5 cycles)*	[60]
Nanostructured bilayered hydrated V ₂ O ₅	Electrochemical deposition on carbon substrate	0.5 M Zn(TFSI) ₂ in AN	0.3–1.5	~0.8	196 mAh g ⁻¹ at C/10	~170 mAh g ⁻¹ at C/10 (130 mAh g ⁻¹ at 20C for 5 cycles)*	[8]

Compound	Electrode Composition†	Electrolyte	Voltage Window (V vs. Zn/Zn ²⁺)	Average Working Voltage (V vs. Zn/Zn ²⁺)	Initial Capacity at Lowest Rate Reported	Reversible Capacity at Highest Rate Reported	Ref.
γ' -V ₂ O ₅	AM:AB:Graphite:PTFE (8:0.75:0.75:0.05)	0.3 M Zn(CF ₃ SO ₃) ₂ in AN	0.3–2.0	0.9	125 mAh g ⁻¹ at 8 mA g ⁻¹	80 mAh g ⁻¹ at 8 mA g ⁻¹ (85 mAh g ⁻¹ at 320 mA g ⁻¹ for 6 cycles)*	[61]
K _{0.11} MnO ₂ ·0.7H ₂ O	AM:Super C45:PVDF (8:1:1)	0.5 M Zn(TFSI) ₂ in AN	0.05–1.90	~0.75	95 mAh g ⁻¹ at 12.3 mA g ⁻¹	~76.0 mAh g ⁻¹ at 12.3 mA g ⁻¹ (~30 mAh g ⁻¹ at 308 mA g ⁻¹ for 5 cycles)*	[62]
δ -MnO ₂	AM:Carbon black:PVDF (8:1.5:0.5)	0.25 M Zn(CF ₃ SO ₃) ₂ in DMSO	0.75–1.80	1.15	159 mAh g ⁻¹ at 50 mA g ⁻¹	75 mAh g ⁻¹ at 100 mA g ⁻¹	[63]
KS6 Graphite	AM:CMC (9:1)	1 M Zn(TFSI) ₂ in AN	1.00–2.55	2.2	42 mAh g ⁻¹ at 50 mA g ⁻¹	~35 mAh g ⁻¹ at 1 A g ⁻¹ (35.7 mAh g ⁻¹ at 4 A g ⁻¹ for 20 cycles)*	[46]
CoS ₂	AM:Super P:PVDF (8:1:1)	3 M Zn(CF ₃ SO ₃) ₂ in AN	0.0–1.6	0.1	156 mAh g ⁻¹ at 0.05C	116 mAh g ⁻¹ at 0.25C	[64]

Compound	Electrode Composition†	Electrolyte	Voltage Window (V vs. Zn/Zn ²⁺)	Average Working Voltage (V vs. Zn/Zn ²⁺)	Initial Capacity at Lowest Rate Reported	Reversible Capacity at Highest Rate Reported	Ref.
DMBQ	AM:Carbon black:PVDF (8:1:1)	0.5 M Zn(TFSI) ₂ in AN	0.0–1.2	0.7	302.6 mAh g ⁻¹ at 0.2C	~25 mAh g ⁻¹ at 0.2C	[65]
PANi	AM:CNT:PVD F (8:0.5:1.5) CNT : carbon nano tube	0.3 M Zn(TFSI) ₂ in PC	0.4–1.4	0.8	~150 mAh g ⁻¹ at 0.5C	120 mAh g ⁻¹ at 1C	[66]
2DQP	AM:AB:PVDF (4:5:1)	0.5 M Zn(TFSI) ₂ in AN	0.01–1.5	~0.7	65 mAh g ⁻¹ at 100 mA g ⁻¹	55 mAh g ⁻¹ at 1000 mA g ⁻¹	[67]
PQ-MCT	AM:KB:PTFE (6:3:1)	0.5 M Zn(CF ₃ SO ₃) ₂ in DMF	0.1–1.7	0.75	145 mAh g ⁻¹ at 50 mA g ⁻¹	100 mAh g ⁻¹ at 1000 mA g ⁻¹	[68]

Compound	Electrode Composition†	Electrolyte	Voltage Window (V vs. Zn/Zn ²⁺)	Average Working Voltage (V vs. Zn/Zn ²⁺)	Initial Capacity at Lowest Rate Reported	Reversible Capacity at Highest Rate Reported	Ref.
K _{0.05} Fe([Fe(CN) ₆] ₂ ·2.6 H ₂ O)	AM:Super C65:Graphite SFG6:PVDF (8.0:1.0:0.2:0.8)	1 M Zn(CH ₃ COO) ₂ (Bio-Ionic Liquid–Water Mixture)	0.8–2	~1.1	122 mAh g ⁻¹ at 10 mA g ⁻¹	115 mAh g ⁻¹ at 10 mA g ⁻¹ (30 mAh g ⁻¹ at 60 mA g ⁻¹ for 10 cycles)*	[34]
MnO ₂ @CNT fibrelike composite electrode	MnO ₂ nanosheet deposited on CNT fiber	2 M Zn(CF ₃ SO ₃) ₂ - PVA gel polymer (Semi-solid state)	1.0–1.8	1.4	188 mAh g ⁻¹ at 100 mA g ⁻¹	~184 mAh g ⁻¹ at 100 mA g ⁻¹	[69]
γ-MnO ₂	AM:Graphite:P EO polymer binder (8:1:1)	Poly(ethylene oxide)-Zn(CF ₃ SO ₃) ₂ -BANFs Composite (Solid state)	1.0–1.8	~1.3	146.2 mAh g ⁻¹ at 15 mA g ⁻¹	~110.0 mAh g ⁻¹ at 30 mA g ⁻¹ (89.2 mAh g ⁻¹ at 150 mA g ⁻¹ for 8 cycles)*	[70]

Compound	Electrode Composition†	Electrolyte	Voltage Window (V vs. Zn/Zn ²⁺)	Average Working Voltage (V vs. Zn/Zn ²⁺)	Initial Capacity at Lowest Rate Reported	Reversible Capacity at Highest Rate Reported	Ref.
Co(III) rich-Co ₃ O ₄ nanorod	Co(III) rich-Co ₃ O ₄ growing on carbon cloth	PAM hydrogel (2 M ZnSO ₄) electrolyte with additive (0.2 M CoSO ₄) (Solid state)	0.8–2.3	~1.9	~178.6 mAh g ⁻¹ at 500 mA g ⁻¹	~119.0 mAh g ⁻¹ at 2000 mA g ⁻¹ (52.0 mAh g ⁻¹ at 8000 mA g ⁻¹ for 10 cycles)*	[71]
[EMIM]PF ₆ -PEDOT:PSS/Bi ₂ S ₃	AM:AB:PVDF (7:2:1)	PAM hydrogel (1 mol kg ⁻¹ Zn(TFSI) ₂ and 21 mol kg ⁻¹ LiTFSI) (Semi-solid state)	0.1–2.3	1.4	275 mAh g ⁻¹ at 300 mA g ⁻¹	177 mAh g ⁻¹ at 1000 mA g ⁻¹ (50 mAh g ⁻¹ at 6000 mA g ⁻¹ for 10 cycles)*	[72]
V ₂ O ₅ /CNT	AM:Super P:PVDF (8:1:1)	Gelatin and alginate-based membrane (Semi-solid state)	0.2–1.6	~0.7	260 mAh g ⁻¹ at 1000 mA g ⁻¹	~212 mAh g ⁻¹ at 2000 mA g ⁻¹ (152 mAh g ⁻¹ at 20000 mA g ⁻¹ for 6 cycles)*	[73]

Compound	Electrode Composition†	Electrolyte	Voltage Window (V vs. Zn/Zn ²⁺)	Average Working Voltage (V vs. Zn/Zn ²⁺)	Initial Capacity at Lowest Rate Reported	Reversible Capacity at Highest Rate Reported	Ref.
Binder-free polyaniline/molecular-decorated carbon cloth	in-situ polymerization of aniline	PVA/1 M Zn(CF ₃ SO ₃) ₂ (flexible quasi solid state)	0.7–1.7	~1.1	165.6 mAh g ⁻¹ at 0.8C	~100.0 mAh g ⁻¹ at 3.3C (96.4 mAh g ⁻¹ at 16.3C for 10 cycles)*	[74]
Electrochromic polypyrrole (PPy)	PPy-electrodeposited on PET film	PVA/KCl/Zn Cl ₂ (Semi-solid state)	0–1.2	~0.5	123 mAh g ⁻¹ at 1900 mA g ⁻¹	~39.38 mAh g ⁻¹ at 4400 mA g ⁻¹	[75]
K _{0.08} Zn _{1.44} Fe(CN) ₆	AM:Super P:Graphite KS6:PVDF (7.5:1.2:0.3:1.0)	1 M ZnSO ₄ (aq)	0.8–1.9	1.7	65.4 mAh g ⁻¹ at 60 mA g ⁻¹	~42.5 mAh g ⁻¹ at 300 mA g ⁻¹	[2]
K _{0.07} Zn[Fe(CN) ₆] _{0.69}	AM:Super P:PVDF (7.5:1.5:1.0)	3 M ZnSO ₄ (aq)	0.8–2.0	1.73	66.5 mAh g ⁻¹ at 60 mA g ⁻¹	~47.4 mAh g ⁻¹ at 300 mA g ⁻¹	[3]
K _{0.02} (H ₂ O) _{0.22} Zn _{2.94} [Fe(CN) ₆] ₂	AM:Super P:PVDF (8:1:1)	0.1 M Zn(SO ₄) ₂ (aq)	1.20–2.05	1.75	62.5 mAh g ⁻¹ at 42.2 mA g ⁻¹	~50.6 mAh g ⁻¹ at 42.5 mA g ⁻¹	[76]

Compound	Electrode Composition†	Electrolyte	Voltage Window (V vs. Zn/Zn ²⁺)	Average Working Voltage (V vs. Zn/Zn ²⁺)	Initial Capacity at Lowest Rate Reported	Reversible Capacity at Highest Rate Reported	Ref.
K _{0.336} Zn _{2.486} [Fe(CN) ₆] ₂ ·3.09H ₂ O	AM:KB:PVDF (7:2:1)	0.5 M ZnSO ₄ + 0.25 M K ₂ SO ₄ (aq)	0.8–2.2	1.937	78.7 mAh g ⁻¹ at 172 mA g ⁻¹	40 mAh g ⁻¹ at 1720 mA g ⁻¹	[18]
K _{2x/3} Cu[Fe(CN) ₆] _{2/3} ·3.4H ₂ O x = 1.0	AM:Super P:PVA (7.5:1.5:1.0)	1 M ZnSO ₄ (aq)	1.2–2.1	1.7	55 mAh g ⁻¹ at 60 mA g ⁻¹	~48 mAh g ⁻¹ at 60 mA g ⁻¹	[77]
KCuFe(CN) ₆	AM:Super P:Graphite SFG6:PVDF (8:0.9:0.2:0.9)	0.1 M Zn(ClO ₄) ₂ + 2 M NaClO ₄ (aq)	1.2–2.1	1.8	55 mAh g ⁻¹ at 60 mA g ⁻¹	~41 mAh g ⁻¹ at 60 mA g ⁻¹	[78]
KCuFe(CN) ₆	AM:Super P:Graphite SFG6:PVDF (8.0:0.9:0.2:0.9)	0.1 M ZnSO ₄ (aq)	1.2–2.1	1.6	55 mAh g ⁻¹ at 1C	37 mAh g ⁻¹ at 10C	[47]
KCuFe(CN) ₆	AM:AB:PVDF (8.0:1.5:0.5)	1 M ZnSO ₄ (aq)	1.0–2.1	~1.55	56 mAh g ⁻¹ at 20 mA g ⁻¹	43 mAh g ⁻¹ at 20 mA g ⁻¹	[79]

Compound	Electrode Composition†	Electrolyte	Voltage Window (V vs. Zn/Zn ²⁺)	Average Working Voltage (V vs. Zn/Zn ²⁺)	Initial Capacity at Lowest Rate Reported	Reversible Capacity at Highest Rate Reported	Ref.
K _{0.71} Cu[Fe(CN) ₆] _{0.72} ·3.7H ₂ O	AM:Super P:Graphite SFG6:PVDF (8.0:0.9:0.2:0.9)	0.02 M ZnSO ₄ (aq)	1.43– 2.13	1.73	47 mAh g ⁻¹ at 60 mA g ⁻¹	~52 mAh g ⁻¹ at 60 mA g ⁻¹ (42 mAh g ⁻¹ at 600 mA g ⁻¹ for 5 cycles)*	[14]
KCu[Fe(CN) ₆]	AM:Carbon black:Graphite: PS (3.75:2.50:2.50: 1.25)	1 M Na ₂ SO ₄ + 0.01 M H ₂ SO ₄ (aq)	1.4–2.1	~1.65	60 mAh g ⁻¹ at 60 mA g ⁻¹	~51 mAh g ⁻¹ at 300 mA g ⁻¹	[80]
Cu _{0.93} Zn _{0.07} [Fe(CN) ₆]	AM:Super C65:Graphite SFG6:PVDF (8.0:0.9:0.2:0.9)	0.2 M ZnSO ₄ (aq)	1.17– 2.07	~1.52	~49 mAh g ⁻¹ at 60 mA g ⁻¹	~42 mAh g ⁻¹ at 60 mA g ⁻¹	[81]
Na _{0.63} (VO) _{1.3} [Fe(CN) ₆] ₂ ·5.8H ₂ O	AM:AB:PVDF (6:3:1)	4 M Zn(CF ₃ SO ₃) ₂ (aq)	0.3–1.9	~1.0	~100 at 500 mA g ⁻¹	~151 mAh g ⁻¹ at 2000 mA g ⁻¹ (122 mAh g ⁻¹ at 5000 mA g ⁻¹ for 10 cycles)*	[82]
K _{1.14} (VO) _{3.33} [Fe(CN) ₆] ₂ ·6.8H ₂ O with DCCF	AM:Super P:PTFE (7:2:1)	2 M ZnSO ₄ in 2:5 water/EG (aq)	0.2–2.0	~0.75	180 mAh g ⁻¹ at 400 mA g ⁻¹	120 mAh g ⁻¹ at 400 mA g ⁻¹ (116 mAh g ⁻¹ at 8000 mA g ⁻¹ for 10 cycles)*	[83]

Compound	Electrode Composition†	Electrolyte	Voltage Window (V vs. Zn/Zn ²⁺)	Average Working Voltage (V vs. Zn/Zn ²⁺)	Initial Capacity at Lowest Rate Reported	Reversible Capacity at Highest Rate Reported	Ref.
Na _{0.61} Fe _{1.94} (CN) ₆ · □ _{0.06}	AM:KB:PTFE (7:2:1)	1 M Na ₂ SO ₄ (aq)	0.8–1.6	1.1	76 mAh g ⁻¹ at 100 mA g ⁻¹	56 mAh g ⁻¹ at 300 mA g ⁻¹ (70.1 mAh g ⁻¹ at 500 mA g ⁻¹ for 10 cycles)*	[84]
KCoFe(CN) ₆ · 5.5H ₂ O	AM:KB:PTFE (7:2:1)	4 M Zn(CF ₃ SO ₃) ₂ (aq)	0.8–2.0	1.75	173.4 mAh g ⁻¹ at 300 mA g ⁻¹	~142.0 mAh g ⁻¹ at 3000 mA g ⁻¹ (109.5 mAh g ⁻¹ at 6000 mA g ⁻¹ after 10 cycles)*	[85]
Na ₂ Mn[Fe(CN) ₆] · 2.78H ₂ O	AM:AB:PTFE (8:1:1)	1 M ZnSO ₄ (aq)	0.97–1.97	1.77	53.7 at 50 mA g ⁻¹	33.0 mAh g ⁻¹ at 50 mA g ⁻¹ (43.3 mAh g ⁻¹ at 300 mA g ⁻¹ for 10 cycles)*	[86]
K _{1.6} Mn[Fe(CN) ₆] _{0.94} · 0.63H ₂ O	AM:KB:PTFE (7:2:1)	30 M KFSI + 1 M Zn(CF ₃ SO ₃) ₂ (aq)	0.5–2.0	1.74	138 mAh g ⁻¹ at 200 mA g ⁻¹	~69 mAh g ⁻¹ at 2000 mA g ⁻¹	[87]

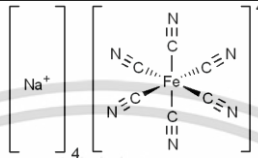
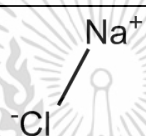
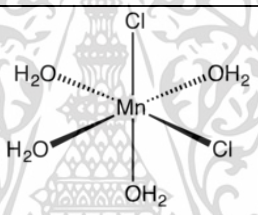
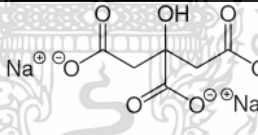
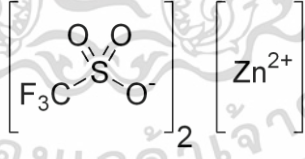
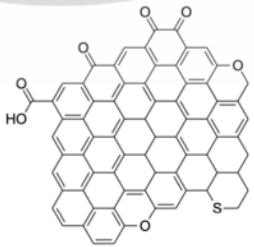
Note: * indicates capacity taken from the rate capability plot or the discharge/charge profile.; † (active material (AM): conductive carbon: binder)

PVDF: poly(vinylidene fluoride), PTFE: polytetrafluoroethylene, CMC: sodium carboxymethyl cellulose, PS: polystyrene, PAM: polyacrylamide, PVA: polyvinyl alcohol, PEO: polyethylene oxide, DMF: dimethylformamide, AB: acetylene black, KB: Ketjen black, CNT: carbon nanotube, CFP: carbon fiber paper, PC: propylene carbonate, DMSO: dimethyl sulfoxide, TEGDME: tetra ethylene glycol dimethyl ether, TMP: trimethyl phosphate, TEP: triethyl phosphate, AN: acetonitrile, EG: Ethylene glycol, PN: propionitrile, Zn(TFSI)₂: Zinc (II) Bis(trifluoromethanesulfonyl)imide, TTFP: Tris(2,2,2-trifluoroethyl) phosphite, NaFSI: Sodium bis(fluorosulfonyl)imide, DCCF: double conductive carbon framework, KFSI: Potassium bis(fluorosulfonyl)imide, BANFs: branched aramid nanofibers PEDOT:PSS: poly(3,4-ethylenedioxythiophene):poly(styrenesulfonate), [EMIM]PF₆: 1-ethyl-3-methylimidazolium-hexafluorophosphate.

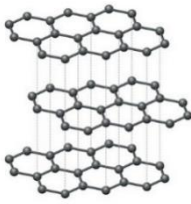

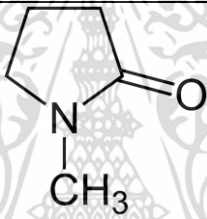
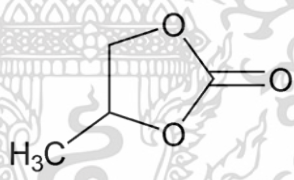
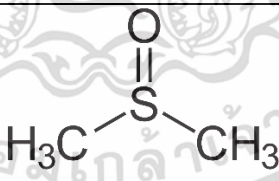
1.3 Experimental Section

1.3.1 Materials

Table 1.2 Chemicals Used in This Work.

Name Chemical Formula	Structure	Purity	Source
Sodium ferrocyanide hydrate $\text{Na}_4\text{Fe}(\text{CN})_6 \cdot 10\text{H}_2\text{O}$		99%	Alfa Aesar
Sodium chloride NaCl		99.5%	SHOWA
Manganese (II) chloride hydrate $\text{MnCl}_2 \cdot 4\text{H}_2\text{O}$		$\geq 99\%$	Sigma-Aldrich
Trisodium citrate hydrate $\text{Na}_3\text{C}_6\text{H}_5\text{O}_7 \cdot 2\text{H}_2\text{O}$		99%	Alfa Aesar
Zinc triflate $\text{Zn}(\text{CF}_3\text{SO}_3)_2$		98%	Alfa Aesar
Carbon black (Super P) C		99%	TIMCAL

เอกสารนี้เป็นเอกสารที่สงวนไว้สำหรับการใช้งานเพื่อการศึกษาเท่านั้น ไม่อนุญาตให้นำไปใช้ประโยชน์ด้านการค้า
ไม่ว่ากรณีใดๆ ทั้งสิ้น อีกทั้งห้ามมิให้ดัดแปลงเนื้อหา และต้องอ้างอิงถึงเจ้าของเอกสารทุกครั้งที่มีการนำไปใช้

Name Chemical Formula	Structure	Purity	Source
Graphite (KS4) C ₆		N/A	Imerys
Zinc metal Zn	Zn	99.98%	Alfa Aesar
Polyvinylidene fluoride (PVDF) -(C ₂ H ₂ F ₂) _n -		N/A	Alfa Aesar
N-methyl-2-pyrrolidinone (NMP) C ₅ H ₉ NO		99.5%	Alfa Aesar
Propylene carbonate (PC) C ₄ H ₆ O ₃		99.7%	Sigma-Aldrich
Dimethyl sulfoxide (DMSO) (CH ₃) ₂ SO		≥ 99.9%	Sigma-Aldrich

1.3.2 Synthesis of Sodium Manganese Hexacyanoferrate (NMHCF)

With a little modification, the method used to prepare NMHCF had been previously reported.[88] In order to make a 100 mL solution, 3 mmol (or 1.45 g) of sodium ferrocyanide hydrate and 240 mmol (or 14.00 g) of sodium chloride were dissolved in deionized water. Then, a 50 mL solution was created by dissolving 6 mmol

เอกสารนี้เป็นเอกสารที่สงวนไว้สำหรับการใช้งานเพื่อการศึกษา 37 เท่านั้น ไม่อนุญาตให้นำไปใช้ประโยชน์ด้านการค้า
ไม่ว่ากรณีใดๆ ทั้งสิ้น อีกทั้งห้ามมิให้ดัดแปลงเนื้อหา และต้องอ้างอิงถึงเจ้าของเอกสารทุกครั้งที่มีการนำไปใช้

(or 1.19 g) of manganese (II) chloride hydrate and 10 mmol (or 2.58 g) of trisodium citrate hydrate in deionized water. After that, the 50 mL solution was slowly dropped to the 100 mL solution via peristaltic pumping and vigorously stirring continuously at room temperature. 1.5 h of dropping was followed by 1 h of aging. The reaction produced a white insoluble precipitate. To eliminate the unreacted compounds, the product was centrifuged at 10000 rpm for 5 min and then washed three times with deionized water. The resultant white precipitate was then decanted and dried in a vacuum oven at 120 °C for 1 d.

1.3.3 Preparation of Zn/NMHCF Cells

Electrochemical properties of Zn/NMHCF were conducted by using CR2032 coin cell type. The cathode electrode was made by blending active material, Super P, graphite KS4, and PVDF in a weight ratio of 5:3:1:1. The blended slurry was coated on stainless steel current collector (20 μm thickness, 10 mm in diameter) and dried in a vacuum at 100 °C for 1 d. The average mass loading of active material was 1–1.5 mg cm^{-2} (200 μm thick).

CR2032 coin cells were assembled in an argon-filled glovebox by using zinc metal (0.25 mm thick, 16 mm diameter) as an anode, GF/A Whatman glass fiber as separator (260 μm thick), and 0.2 M zinc triflate in 1:4 v/v PC/ DMSO as electrolyte (130 μL). [63] Before making the electrolyte, zinc triflate was dried at 120 °C in vacuum for 2 d to eliminate moisture content in the salt. PC and DMSO are anhydrous solvents which were dried over molecular sieves (3 Å) before use. On a Biologic VMP3 potentiostat and an Arbin Instruments battery tester, respectively, cyclic voltammetry (CV) and galvanostatic tests were carried out at room temperature. Using a Biologic VMP3

multichannel potentiostat, electrochemical impedance spectroscopy (PEIS) was performed over a frequency range of 1 kHz – 4 mHz with an amplitude voltage (V_m) of 10 mV.

1.3.4 Materials Characterization

(1) Powder X-ray Diffraction (PXRD)

As-synthesized powder sample was ground and dried at 120 °C in a vacuum for 1 d before measurements, PXRD patterns were collected by using zero background sample holders on a Bruker D8 Advance ECO with Cu K α radiation.

(2) Synchrotron Powder X-ray Diffraction (SPXRD)

The synchrotron PXRD data were collected at TPS 09A beamline at the National Synchrotron Radiation Research Center (NSRRC), Taiwan). The powder sample was sealed in a glass capillary (0.2 mm diameter). Data collection took place for 120 s utilizing a Mar345 image plate detector with Debye-Scherrer geometry and 15 keV X rays (wavelength = 0.82656 Å) provided by an *in-vacuo* undulator (IU22). By using GSAS-II software,[89] the patterns were refined, and the angle calibration was done in accordance with the LaB₆ (SRM 660c) standard.

(3) Inductively Coupled Plasma-Mass Spectrometry (ICP-MS)

ICP-MS was used to calculate the ratio of iron, manganese, and sodium. ELEMENT XR from Thermo Scientific was used to perform the ICP-MS. To prepare the samples, 5 mg of NMHCF was dissolved in 1500 μ L of sulfuric acid and 500 μ L of

hydrochloric acid, then the mixture was diluted with ultra-high-quality water to make a 250 mL solution.

(4) *Thermogravimetric Analysis (TGA)*

The water content of NMHCF was determined via TGA utilizing a PerkinElmer TGA4000 analyzer in a nitrogen environment with a ramping rate of 5 °C min⁻¹. The sample was heated from 25 °C to 600 °C.

(5) *Elemental Analysis (EA)*

EA was done on an Elementar Vario EL III. EA was used to calculate the ratio of carbon (C), hydrogen (H), and nitrogen (N) contents in the sample.

(6) *Fourier-Transform Infrared Spectroscopy (FT-IR)*

FT-IR was performed on a NICOLET 6700 FT-IR spectrometer using the KBr pellet technique. The data was collected in a wavenumber of 200 to 3000 cm⁻¹ with a 532 nm laser beam at room temperature.

(7) *Scanning Electron Microscopy (SEM)*

SEM was carried out on a SU8010 HR-FESEM. The samples were platinum-sputtered before the test to increase the conductivity of the material.

(8) *Transmission Electron Microscopy (TEM)*

A JEM-2100F electron microscope was used to carry out HRTEM, scanning transmission electron microscopy (STEM), selected area electron diffraction (SAED), and energy-dispersive X-ray spectroscopy (EDX) elemental mapping. After being

thoroughly dispersed in DMF, a small sample was dropped onto a copper grid under an argon environment.

(9) Raman Spectroscopy

A DXR Raman microscope was used to collect data using a 532 nm laser beam at room temperature.

(10) Ex-situ Characterization

All of the *ex-situ* samples were obtained by disassembled coin cells that had been charged or discharged at a rate of 30 mA g⁻¹ to a particular state-of-charge (active mass loading 2.5 mg cm⁻²). Without any contact with the air, the data were gathered on the electrodes. In beamline, TPS 44A at NSRRC, Taiwan, synchrotron X-ray absorption spectroscopy (XAS) experiments were performed *ex-situ*. The Fe and Mn foils were utilized as a reference for the energy calibration, and the data were gathered in transmission mode. The Athena software program was used to standardize the spectrum. *Ex-situ* PXRD measurements were performed using Cu K α radiation on a Bruker D2 diffractometer.

1.4 Results and Discussion

1.4.1 Materials Characterization

PBAs are often produced using the conventional precipitation process, which frequently results in unideal products. This is caused by the extraordinarily low solubility product constants (K_{sp}) of PBA compounds.[90] Because of the immediate and simultaneous occurrence of the nucleation and crystal growth processes, as well as the extremely rapid reaction kinetics, the resulting products are nanosized and have an irregular structure as well as a lot of structural vacancies.[90] To improve the crystallinity of PBAs, Co-precipitation [2,3] and the use of dispersants or additives [90-93] are strategies which can help reduce the reaction rate.

In the synthesis of NMHCF, $MnCl_2$, and $Na_4Fe(CN)_6$ were utilized as the primary reaction reagents. Trisodium citrate dihydrate ($Na_3C_6H_5O_7 \cdot 2H_2O$) and NaCl were used to increase the concentration of Na ions in the reaction mixture and delay the crystallization process. The metal ions (Mn^{2+}) are initially attracted to citrate ions to create Mn-citrate chelate complexes, which can function as a reservoir to gradually release Mn^{2+} into the reaction mixture to react with hexacyanoferrate anions and generate nuclei for the crystal formation process.[90] Moreover, in the co-precipitation with the citrate-assisted method (Figure 1.13), citrate anions may adsorb on the surface of the crystal, slowing development and preventing crystal aggregation.[90] The high alkaline ion content in PBAs is preferred. Therefore, a high Na ion content in the reaction environment leads to higher Na ions in the final product.[94] NMHCF with reduced structural defects and coordinating water can be produced as a result. Since, they were discovered to have a significant impact on the properties of the final products,

such as the particle size and shape, product morphology, color, as well as

electrochemical performance, all reaction parameters, including reaction temperature, stirring speed, and time, aging time, and drying method, were kept constant.

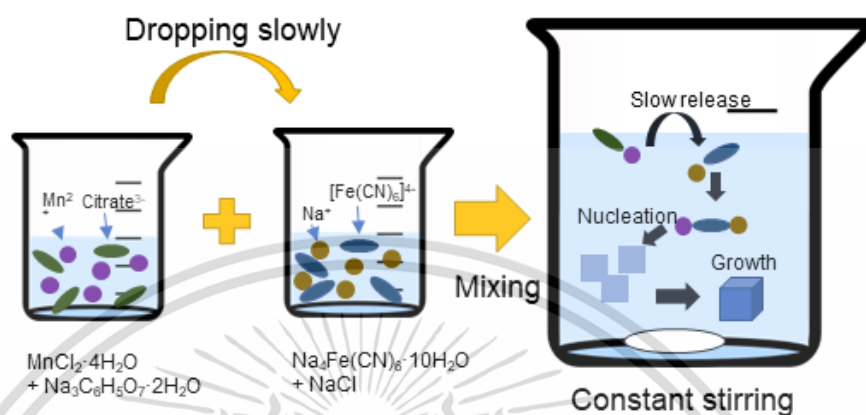


Figure 1.13 Schematic diagram of co-precipitation with citrate-assisted method.

ICP-MS analysis revealed that the *as-synthesized* compound Na:Mn:Fe atomic ratio was 1.2:1.0:0.8. TGA was used to determine how much water was present in the NMHCF product (**Figure 1.14**). The first two steps that take place below 210 °C might be ascribed to the removal of interstitial water and the loss of adsorbed water, respectively.[91,95] The water content per formula unit is 3 units which correlates to weight loss (17.57%). The disintegration of the framework is indicated by the dramatic weight loss in the region of 225 °C – 450 °C.[91] EA was also utilized to verify that the C:N ratio, which was 1:0.93, was the accurate ideal of a 1:1 ratio. The chemical composition of the compound is $\text{Na}_{1.2}\text{Mn}[\text{Fe}(\text{CN})_6]_{0.83}\cdot\text{H}_2\text{O}$ as a result.

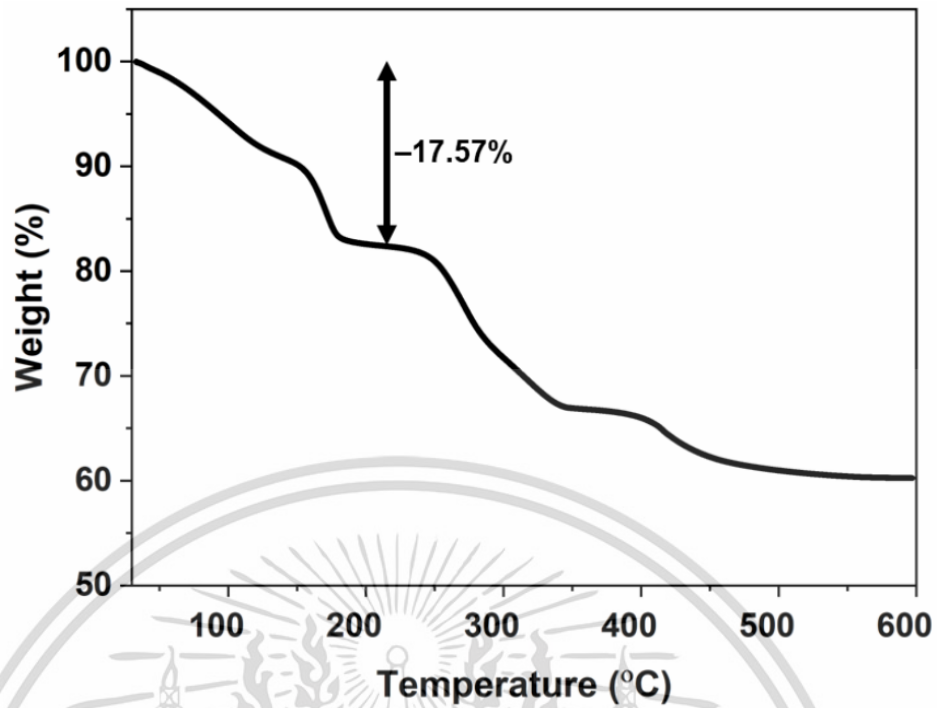


Figure 1.14 TGA of as-prepared NMHCF.

In-house and synchrotron PXRD patterns of *as-synthesized* NMHCF show a pure crystalline monoclinic phase with all the characteristic peaks as reported previously (**Figure 1.15**).^[91] Crystal structure of *as-synthesized* NMHCF was confirmed by the profile refinement of the synchrotron PXRD data revealing monoclinic space group ($P1\ 21/n\ 1$) with lattice parameters, $a = 10.54\ \text{\AA}$, $b = 7.47\ \text{\AA}$, $c = 7.41\ \text{\AA}$, and $\beta = 91.90^\circ$ (**Figure 1.16**).

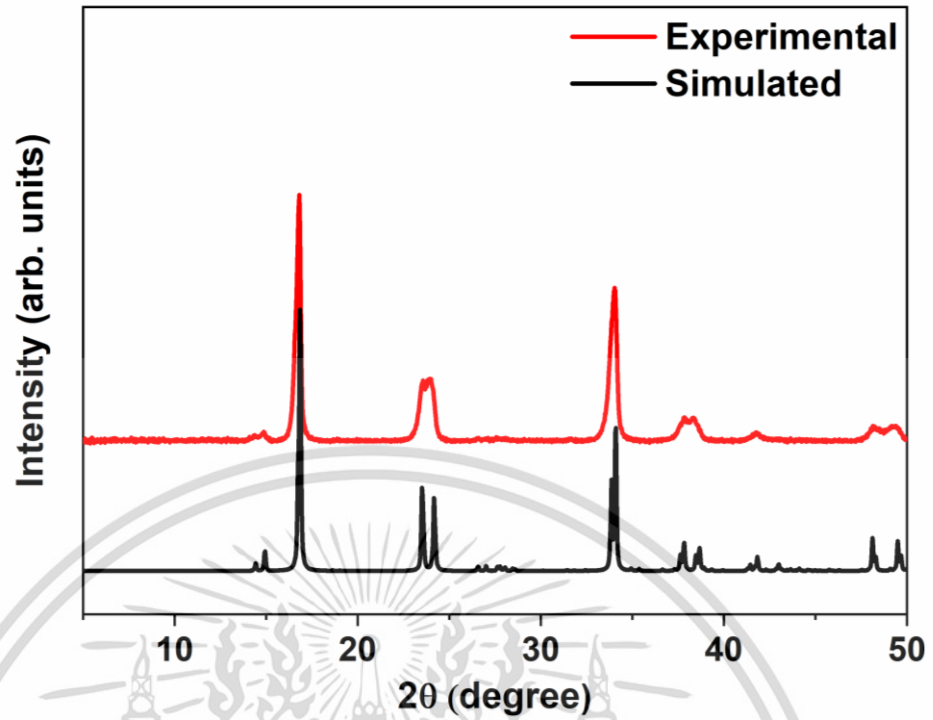


Figure 1.15 PXRD patterns of NMHCF from this work and monoclinic PBA.

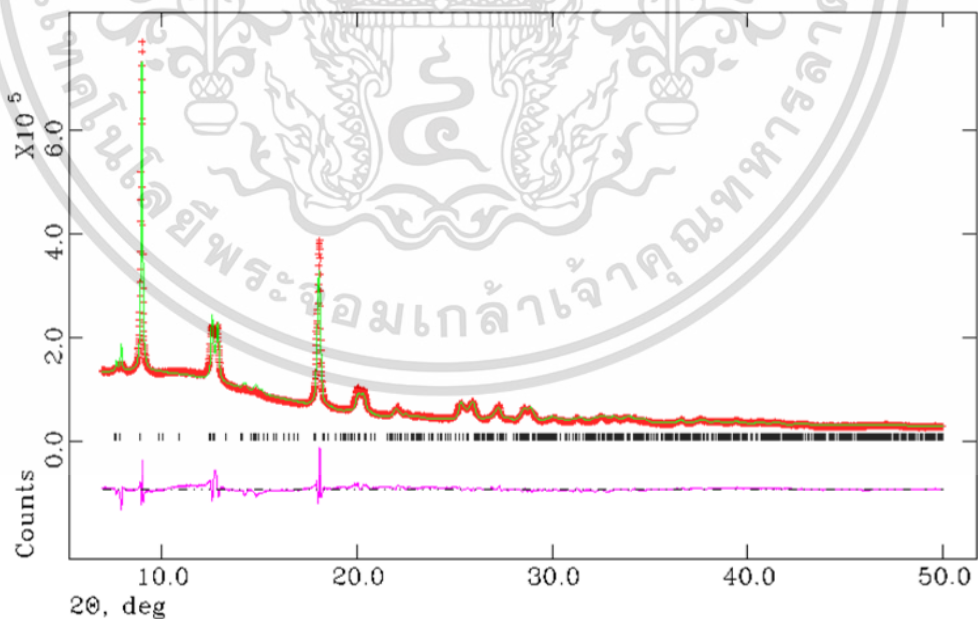


Figure 1.16 Le Bail refinement of synchrotron X-ray diffraction (SXR)

pattern of NMHCF in P21/n, $wRp = 5.43\%$: $a = 10.55 \text{ \AA}$, $b = 7.48 \text{ \AA}$, $c = 7.42 \text{ \AA}$, and

$\beta = 91.93^\circ$ (measured, orange; calculated, green; difference, pink; Bragg reflections, vertical tick marks).

The Raman spectrum was collected in the wavelength range of 2000 and 2200 cm^{-1} (**Figure 1.17**). Two obvious peaks at 2088 and 2127 cm^{-1} were detected, indicating the vibration of the cyanide group and the bonding strength of the cyanide group connecting to Fe and Mn ions with different oxidation states.[94,96] The coordination of Fe and Mn atoms in the $\text{C}\equiv\text{N}^-$ bridging ligand allows for various possible pairs of oxidation states such as $\text{Fe}^{\text{II}}-\text{CN}-\text{Mn}^{\text{II}}$, $\text{Fe}^{\text{II}}-\text{CN}-\text{Mn}^{\text{III}}$, $\text{Fe}^{\text{III}}-\text{CN}-\text{Mn}^{\text{II}}$, and $\text{Fe}^{\text{III}}-\text{CN}-\text{Mn}^{\text{III}}$. [94] Based on the Raman data, it is evident that the oxidation number of both Fe and Mn is 2.[97], as the disproportionation reaction of Mn^{3+} hinders the creation of a charged NMHCF with Mn^{3+} . [98]

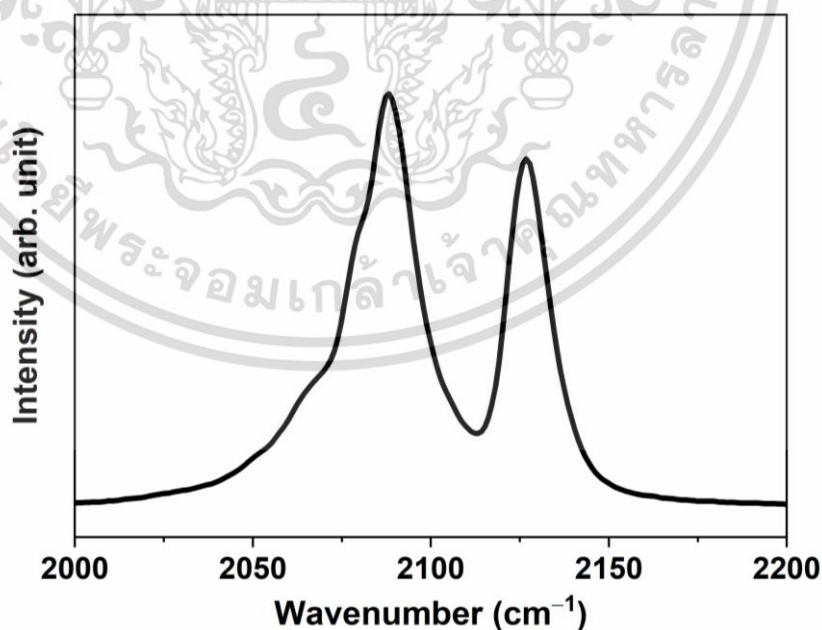


Figure 1.17 Raman spectrum of NMHCF.

The sharp absorption seen at 2063 cm^{-1} in the FT-IR spectrum (**Figure 1.18**) indicates the stretching vibration of the CN group in $\text{Fe}^{\text{II}}\text{-CN-Mn}^{\text{II}}$. This group is sensitive to oxidation by the atmosphere, so the oxidation state is likely $\text{Fe}^{\text{II}}\text{-CN-Mn}^{\text{II}}$. [90,99] The absorption bands seen at 1620 cm^{-1} and 3425 cm^{-1} represent the bending modes of water and the stretching modes of hydroxyl group, respectively. [91,99] Additionally, the Fe-CN and Fe-C absorption bands are observed at 596 cm^{-1} and 453 cm^{-1} wavelength, respectively. [99] These observations provide insight into the molecular structure and composition of the sample being studied.

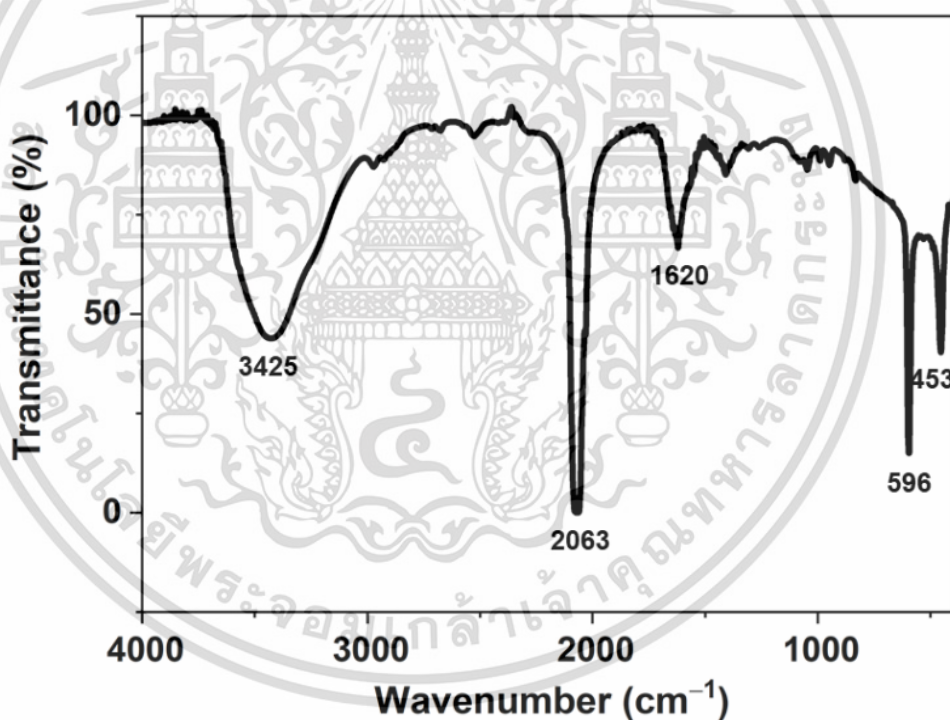


Figure 1.18 FT-IR of as-prepared NMHCF sample.

1.4.2 Material Morphology

The morphology of the *as-synthesized* NMHCF was characterized by SEM and TEM. The SEM and TEM images (**Figure 1.19a–c**) reveal the cubic morphology of NMHCF, with a particle size of ~100–150 nm, and the particles appear to be uniform with no signs of any impurities. In the high-resolution TEM (HRTEM) image, the diffraction fringes with d-spacing of 0.375 and 0.536 nm are assigned to the (–2–1–1) and (011) lattice planes of the NMHCF structure, respectively (**Figure 1.19d,e**). Moreover, the SAED pattern (**Figure 1.19f**) clearly reveals the crystalline structure of NMHCF. The elements mapping images suggest a uniform distribution of Na, Mn, and Fe elements (**Figure 1.19**).

After assembly, the pristine electrode is charged to extract Na ions from the PBA structure. As Na ions move out from the PBA structure, the transition metal ions are oxidized to maintain charge balance. Then, after discharging down to 0.3 V, NMHCF shows the insertion of Na and Zn ions into the structure. These phenomena are confirmed by the elemental mapping (**Figure 1.22**).

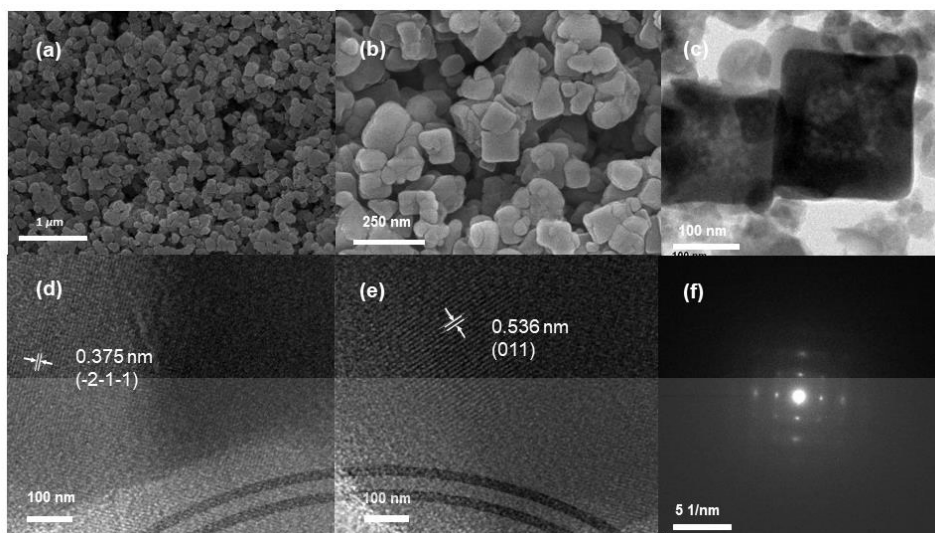


Figure 1.19 (a,b) SEM and (b) TEM images of NMHCF at different magnifications (d,e) HRTEM images with d-spacing 0.375 and 0.536 nm indicating (–2–1–1) and (011) planes and (f) SAED pattern of NMHCF.

1.4.3 Electrochemical Investigation

Figure 1.20a shows the charge/discharge profile of the first cycle at different current densities. The cells operate on voltage window in the range of 0.3 – 2.0 V that is quite wide compared with previous work published (**Table 1.1**). The open circuit voltage (OCV) is 1.0 V vs Zn/Zn²⁺. The charge/discharge curve of the Zn/NMHCF cell presents the first 2 plateaus at 1.50 V and 1.75 V during the charging process. It corresponds to the Na ion removed from the structure. The compound undergoes reduction during discharge, resulting in two voltage plateaus at roughly 1.65 V and 1.45 V, yielding a specific capacity of 89.5 mAh g⁻¹ (theoretical discharge capacity = 115.5 mAh g⁻¹), which translates to about 1.02 electron transfer per formula unit of NMHCF. It is important to note that the majority of the discharge capacity could be acquired from the voltage plateau between 1.70 V and 1.30 V, with an average working voltage of

about 1.50 V, which is significantly high compared to the majority of cathodes

previously reported for non-aqueous ZIBs (**Table 1.1**). Even though some other cathode materials for ZIBs with organic electrolytes could deliver a higher capacity, the operating voltage is usually lower.[100] The wide electrochemical window electrolyte is selected to support the redox reactions.²⁹ The $\text{Zn}(\text{CF}_3\text{O}_3\text{S})_2$ in combination with non-aqueous solvents exhibits remarkable stability in facilitating Zn/NMHCF cells at high potentials which are required to activate the high spin $\text{Mn}^{\text{II}}/\text{Mn}^{\text{III}}$.

The electrochemical process was characterized by a charge/discharge profile and CV curve. **Figure 1.20c** shows the CV curve at a scan rate of 0.05 mV s^{-1} during the first cycle. It demonstrates two pairs of redox peaks at $1.56 \text{ V}/1.47 \text{ V}$ and $1.81 \text{ V}/1.68 \text{ V}$ that correspond to the redox couple the low-spin $\text{Fe}^{\text{II}}/\text{Fe}^{\text{III}}$ and high spin $\text{Mn}^{\text{II}}/\text{Mn}^{\text{III}}$, respectively.

Likewise, at different current densities of 40, 90, 100, 580, and 820 mA g^{-1} , the first discharge capacities of NMHCF are 87.0, 78.8, 75.8, 62.6, and 56.4 mAh g^{-1} , respectively (**Figure 1.20b**). With increasing current densities, the voltage plateaus still remain visible. The cathode appears to be relatively robust, especially at rates of 90 and 100 mA g^{-1} (1C), with reversible capacities of 57 and 55 mAh g^{-1} , or 71.4% capacity retention for both rates after 100 cycles (**Figure 1.20d**). Although increasing current densities lead to a decrease in capacities due to the kinetic effects, the PBA can still deliver high reversible capacity (30 mAh g^{-1} for 100 cycles) at a high rate (820 mA g^{-1}). In addition, the capacity is higher compared with the previously reported non-aqueous ZIBs with 8 mAh g^{-1} at the highest current rate of 224 mA g^{-1} . [4]

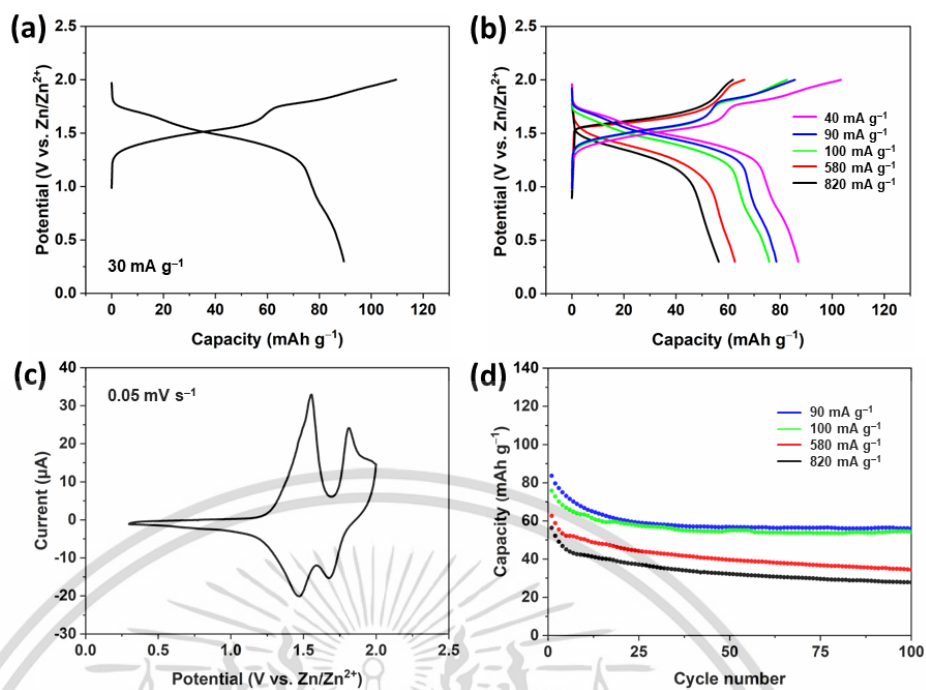


Figure 1.20 Electrochemical performance of the NMHCF a) Charge/discharge profile of the first cycle at 30 mA g⁻¹. b) Charge/discharge profile of the first cycle at various current densities. c) Cyclic voltammogram of NMHCF. d) Cycling performance at various current densities for 100 cycles.

1.4.4 Mechanistic Study

The mechanistic study of the Mn-Fe PBAs as a cost-effective and durable cathode for non-aqueous ZIBs is a crucial aspect of this thesis. This section aims to investigate the ion insertion or extraction mechanisms in the cathode material. To achieve this, various analytical techniques were employed, including *ex-situ* XRD, *ex-situ* X-ray absorption near-edge structure (XANES), STEM, and energy-dispersive X-ray spectroscopy (EDX) analyses, as well as EIS at various states of charge. Through this comprehensive approach, a deeper understanding of the electrochemical behavior

and performance of the Mn-Fe PBAs as a cathode material for non-aqueous ZIBs can be obtained.

(1) *Ex-situ* PXRD

In order to understand the insertion and extraction mechanism, the phases changing during charge/discharge states were investigated by *ex-situ* XRD. **Figure 1.21** shows XRD patterns at the initial and different charge/discharge states. Phase change during charge and discharge is induced by guest ion extraction and insertion. For the pristine electrode, four characteristic peaks of NMHCF appear at 14.9°, 16.9°, 23.6°, and 34.1°, corresponding to (101), (011), (-2-1-1), and (022) planes, respectively. In addition, peaks at 26.6° and 44° correspond to the (002) reflection of KS4 graphite, and stainless steel 316 from the electrode, respectively.[101,102] When the pristine electrode is charged to 1.72 V, which is the end of the first plateau. All the NMHCF peaks slightly shift to the left, suggesting an expansion of the unit cell.[103] Then, the electrode is fully charged to 2.0 V, and the double peak around 14.9° merges to a single peak indicating the transformation of the monoclinic to cubic phase.[104] Afterward, the NMHCF is discharged to the cutoff voltage from 2.0 V to 0.3 V. All the NMHCF peaks are shifted to higher degrees of 2θ , with the original peak positions and characteristic features of the monoclinic phase being restored. This displacement of NMHCF peak positions indicates the expansion and shrinkage of the PBA structure and reveals the extraction and insertion of the guest ions. Normally, alkali-ion extraction in the PBA lattice crystal structure and the right shift of peaks in the charging state imply shrinkage in the PBA structure. However, this NMHCF has a cubic structure. The

transformation of monoclinic to cubic affects a reduction of β and influences lattice expansion. All NMHCF peaks revert to their original states after ion insertion or discharge, demonstrating high structural reversibility.[96] The change of the oxidation states of the metals in PBA was confirmed by *ex-situ* XANES in the next session.

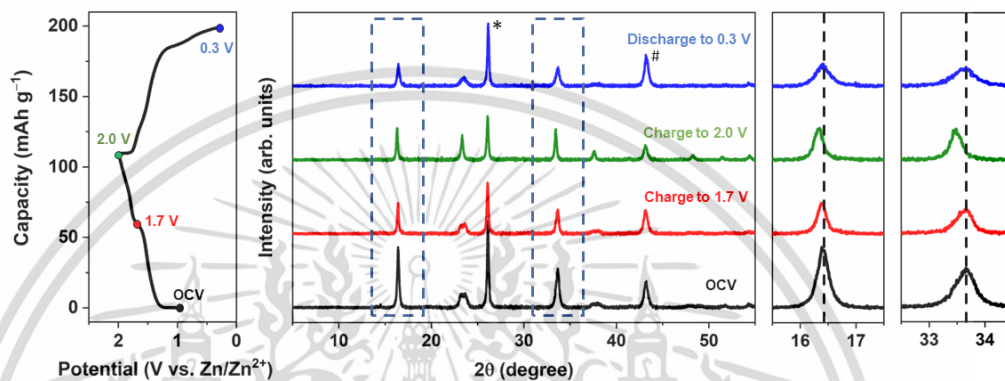


Figure 1.21 *Ex-situ* XRD patterns of NMHCF electrode at different states-of-charge: starting from (pristine) initial state charged up to 1.7 V and 2.0 V, and discharged back to 0.3 V.

(2) STEM and EDX Analyses

The electrodes were investigated by elemental mapping using STEM and EDX analyses at the end of charge and discharge, as shown in **Figure 1.22**. When compared to the pristine compound at OCV, the charged NMHCF electrode had a lower concentration of Na and a uniform distribution of Mn, Fe, and N. The electrochemical results from Zn/NMHCF cells above, which show that Fe and Mn metals in NMHCF undergo oxidation during charge as Na^+ is removed to maintain charge balance, are consistent with this observation. In order to maintain charge neutrality during discharge,

Fe and Mn species are reduced as cation charge carriers such as Zn^{2+} are inserted into

the framework of NMHCF. This effect is also seen in the elemental mapping, which demonstrates an increase in zinc concentration at the end of discharge.

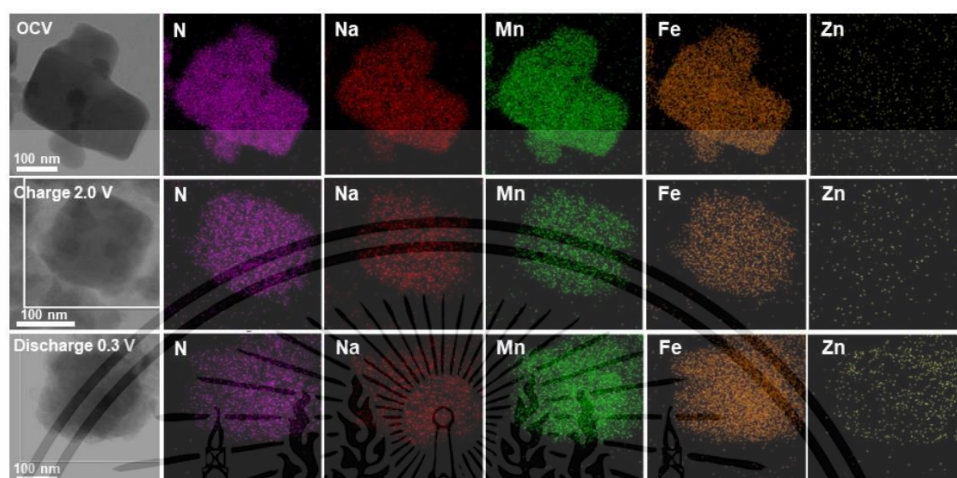


Figure 1.22 STEM images and elemental mapping of NMHCF particles at different states of charge, OCV, 2.0 V, and 0.3 V.

(3) *Ex-situ* XANES

Ex-situ XANES was performed in order to understand the change in the oxidation state of the transition metal ions in NMHCF during charge/discharge, as illustrated in **Figure 1.23**. Starting from the pristine electrode (position A, black), the oxidation state of both Mn and Fe are 2+ (Fe pre-edge peak at 7114.2 eV; Mn pre-edge peak at 6540.6 eV). Afterward, NMHCF is charged to 1.72 V (position B, red) which is the end of first plateau in the charge/discharge curve. The pre-edge peak of Fe shifts to higher energy (7114.6 eV assigned to Fe^{III}), while the pre-edge peak of Mn does not move to higher energy. This indicates that the Fe^{II}/Fe^{III} is active, while the Mn^{II}/Mn^{III} is inactive.[105] Then, the electrode is continually charged up to 2 V (position 3, green), and the pre-edge of Mn slightly shifts to higher energy (6541.0 eV for Mn^{III}), whereas

the pre-edge of Fe stays at the same position. These phenomena that occur at the second plateau indicate that Mn^{II} is oxidized to Mn^{III} , while the Fe couples stay inactive.[106] After that, the electrode is discharged down to 0.3 V (position D, blue), and the pre-edge peaks both of Fe and Mn shift back to lower energy at the same position as the pristine (position A, black). These indicate that both Fe and Mn ions are reduced. It is worth noting that XANES spectra provide useful information about the oxidation state change of transition metal ions in NMHCF structure during charge/discharge in ZIBs. In addition, the Fe and Mn spectra imply the redox reversibility of NMHCF.

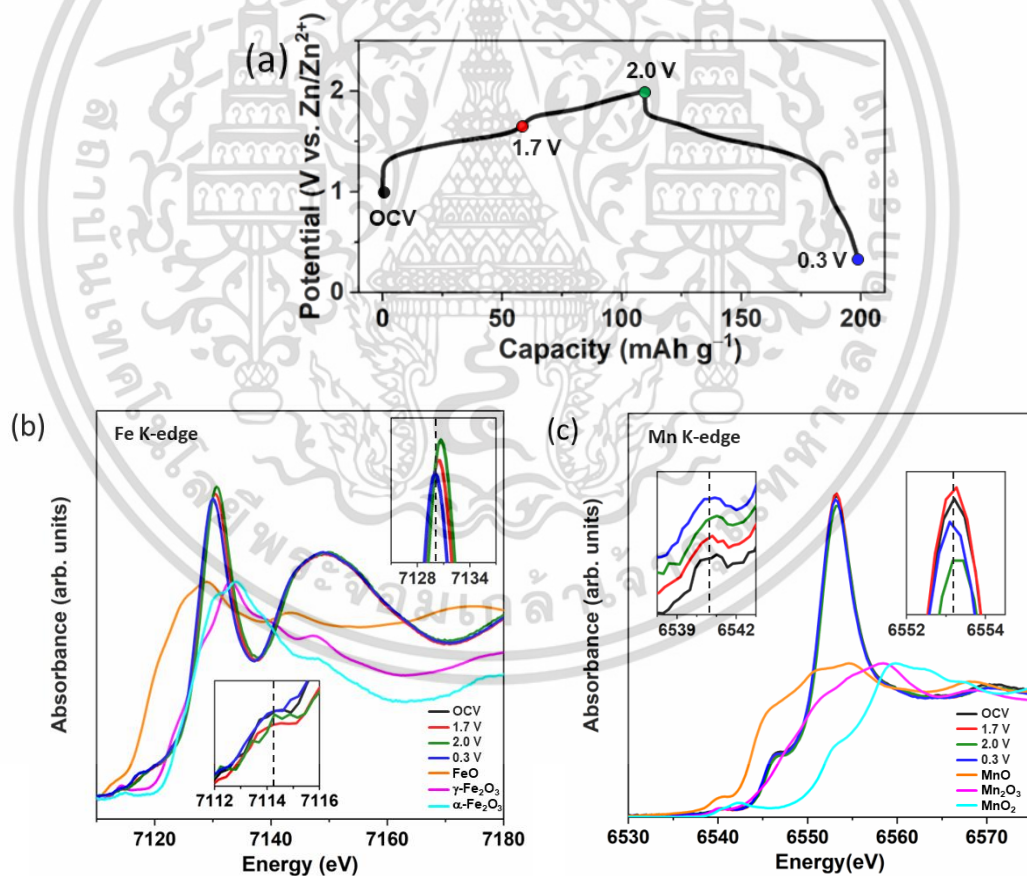


Figure 1.23 *Ex-situ* XANES spectra and (a) corresponding voltage profile of (b)

Fe K-edge and (c) Mn K-edge.

(4) EIS Analysis

At various states of charge during cycling, the Nyquist plots for the Zn/NMHCF cell were obtained to gain an additional understanding of electrochemical performance, especially of capacity fade (**Figure 1.24**). The Zn/NMHCF cell's Nyquist plot is made up of two semicircles that partially overlap in the medium to high-frequency ranges with a linear signal in the low-frequency range. The EIS data were fit with an appropriate equivalent circuit (**Figure 1.24b**) by using Zfit in EC-lab software. The fitted impedance values from the equivalent circuit are shown in **Figure 1.24**. The R_b is the internal resistance of the cell, which is the impedance from the electrolyte, electrodes, and separator. The passivation film impedance (R_{SEI}) and the charge transfer impedance (R_{ct}) correspond to the semicircles. Warburg impedance (W) relates to the diffusion process of ions at low frequencies. The impedance from internal resistance (R_b) was almost constant in any measured conditions. The effect of the state of charge, while ion insertion into the structure during discharge, requires more energy for the insertion of ions because of the lower active sites in the electrode.[63] Impedance during discharge is higher than that of charge because SEI is formed in the discharge process while decomposing in the charging process.[107] Additionally, the inclined line's length increase observed after discharge demonstrates a worse diffusivity of guest ions in the electrode material when ions were introduced into the structure.[58] NMHCF upon 100th cycle was collected at the end of discharge (0.3 V). The semicircle diminished throughout cycling because the active material surface area is larger as a result of electrochemical grinding after repeated charge/discharge processes.[62]

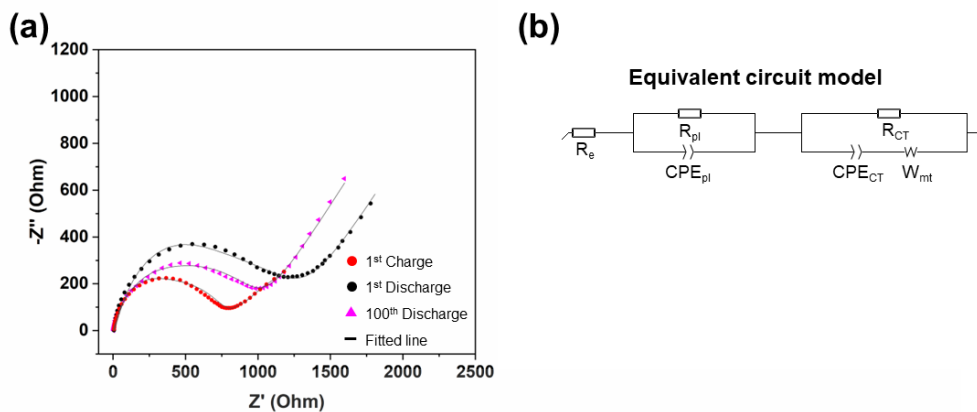


Figure 1.24 (a) The electrochemical impedance spectra of NMHCF electrodes at different states of charge, and b) the corresponding equivalent circuit.

Table 1.3 Estimated Parameters of Equivalent Circuit Models for Zn/NMHCF Cells.

Condition	Potential (V vs. Zn/Zn ²⁺)	R _b (Ohm)	R _{sei} (Ohm)	R _{ct} (Ohm)
After 1 st charge	2.0	6.35	203	596
After 1 st discharge	0.3	6.12	388	912
After 100 th discharge	0.3	3.37	335	668

1.5 Conclusion

$\text{Na}_{1.2}\text{Mn}[\text{Fe}(\text{CN})_6]_{0.8}\cdot 3\text{H}_2\text{O}$ (NMHCF) was successfully synthesized using citrate-assisted crystallization and investigated as an affordable cathode material for a non-aqueous rechargeable ZIBs, exhibiting excellent electrochemical performance with broad operating voltage, high capability, and long-term cyclability. The material was found to possess two redox-active sites which are Fe and Mn performing under high current densities up to 820 mA g^{-1} and delivering an initial discharge capacity of 89.5 mAh g^{-1} at a rate of 30 mA g^{-1} . The electrode material is found to remain stable without any structural collapse after long cycling. The structurally optimized NMHCF showed the effect of water and $\text{Fe}(\text{CN})_6$ vacancy number in the structure on the electrochemical performance. The *ex-situ* characterizations of the cell, namely, HRTEM, XRD, and XAS, provide more understanding of the phenomena inside the material. The reversibility of NMHCF is directly confirmed by electrochemical performance and structural/chemical information obtained by several *ex-situ* techniques. This work sheds light on potential material design approaches for large-scale high-performance energy storage systems.

CHAPTER 2

ECO-FRIENDLY EXTRACTION OF LIGNIN

*This work is based on a published article: Yimtrakarn, T.; Kaveevivitchai, W.; Lee, W.-C.; Lerkkasemsan, N. "Study of Lignin Extracted from Rubberwood Using Microwave Assisted Technology for Fuel Additive", *Polymers* **2022**, *14*, 814.*

2.1 Introduction and Research Motivation

2.1.1 Introduction

Industrial technology is rapidly depleting finite fossil fuel resources, making renewable energy an increasingly crucial alternative.[108] Lignin has garnered significant attention for its diverse applications, such as being used as a dispersant[109-111], protective UV-absorbent[112,113], (nano)composite[114,115], and nanoparticle[116,117]. Notably, the process of turning lignin nanoparticles into highly fluorescent graphene quantum dots is necessary for lignin to be valued as a value-added product.[118] Because of the complex nature of lignin's structure, the pretreatment procedure used to separate lignin from biomass is an essential step in the extraction process. Lignin extracted using a particular technique needs detailed characterization to assure appropriateness for certain applications.[119] Recently, several lignin manufacturing processes have drawn interest, including solvolysis, hydrogenolysis, oxidation, acid hydrolytic fractionation, and supercritical solvent extraction.[120-124]

Chemical delignification is one method employed to extract lignin from biomass, utilizing either aqueous or organic solvents.[125] Alcohol is commonly used

for delignification among organic solvents.[126,127] Because of their low risk, ease of recovery, and efficient diffusion into the wood, the extraction solvents used in this experiment, ethanol and isopropanol, were chosen.[128] Employing a ternary solvent (MBK, ethanol, and water), Chutikan Inkrod et al.[129] achieved a 20% extraction efficiency at 160 °C while focusing on the lignin extraction from inexpensive Para rubberwood sawdust identical to ours. With the ideal circumstances of 0.5 moles of ionic liquid, 120 min of extraction time, and 100 °C temperature, Ahmad Adlie Shamsuri and Dzulkefly Kuang Abdullah effectively recovered lignin from rubberwood, yielding 13.03 wt%.[129]

Microwave technology provides an alternative method for heating biomass. Unlike other methods that rely on conduction, microwaves directly generate heat within a material by radiating electromagnetic energy. This technique offers advantages such as reduced extraction time, increased product yield, energy savings, and uniform heat distribution.[130] Our method of utilizing ethanol and microwave to successfully remove lignin from sawdust is similar to a study by YU Hai-bo et al.[131], which used microwave and ethanol to extract polyphenols from the grape peel. With our method, we hope to accomplish the advantages of this technology, such as a shorter extraction time, reduced polyphenol oxidation, and enhanced polyphenol yield. Saksit Imman et al.[132] indicate that one benefit of using microwave-assisted extraction is that the extraction process takes less time. They used microwave-assisted solvolysis to remove lignin from rice straw and discovered that the microwave treatment led to faster reaction times, uniform heat distribution, and greater reaction rates. According to Long Zhou et al.[133], using microwaves yielded lignin with better purity and yield when compared

to traditional methods, which is consistent with the results of a previous investigation.[134]

This work focuses on the microwave-assisted solvolysis of ethanol and propanol to separate lignin from sawdust. The rubberwood lignin that was extracted as part of the experiment was characterized. The long-term goal of this study is to substitute toxically dangerous and difficultly recovered acidic or alkaline solvents with alternatives like ethanol or propanol.

2.1.2 Research Motivation

The depletion of limited fossil fuels by industrial technology has raised significant concerns about the sustainability of our energy sources. As these non-renewable resources continue to diminish, there is an urgent need to explore alternative energy options that can mitigate our reliance on fossil fuels. Renewable energy has emerged as a promising solution, and lignin, a natural polymer found in biomass, has garnered considerable attention for its potential as a sustainable energy source. Lignin offers a range of applications, including its use as a dispersant, UV-absorbent, composite material, and nanoparticle. Harnessing lignin's potential requires efficient extraction methods that can be applied to biomass. Therefore, there is a pressing motivation to investigate innovative techniques for the extraction of lignin from biomass that can contribute to the development of renewable energy technologies.

The purpose of this study is twofold. Firstly, we aim to explore the solvent extraction of lignin from biomass using a microwave-assisted method. Microwave-assisted extraction techniques have shown promise in various fields due to their

potential to enhance extraction efficiency, reduce extraction time, and ensure uniform heat distribution. By applying this method to lignin extraction, we seek to determine its effectiveness in improving the efficiency and yield of lignin extraction compared to traditional methods. This investigation will provide valuable insights into the feasibility and potential advantages of microwave-assisted extraction for lignin production and applications.

Secondly, we aim to investigate the parameters involved in the solvent extraction process with microwave assistance. Understanding the key factors that influence the efficiency and selectivity of the extraction process is crucial for optimizing lignin extraction. Parameters such as the type of solvent, extraction temperature, and extraction time play vital roles in determining the yield and quality of extracted lignin. Through systematic experimentation and analysis, we will examine the impact of these parameters on the extraction process. This investigation will help identify the optimal conditions for lignin extraction using the microwave-assisted method, thereby contributing to the development of more efficient and sustainable lignin extraction protocols.

Overall, the motivation behind this study is to address the challenges posed by fossil fuel depletion and contribute to the advancement of renewable energy technologies. By investigating the solvent extraction of lignin from biomass using a microwave-assisted method and exploring the associated parameters, this research aims to provide valuable insights into efficient and sustainable lignin extraction processes. The findings of this study can potentially facilitate the development of novel and environmentally friendly methods for lignin production, thereby supporting the transition towards a more sustainable energy future. Additionally, by characterizing the

extracted lignin and evaluating its properties, we also aim to explore the feasibility of utilizing lignin as a fuel additive. Understanding the potential of lignin as a renewable energy resource will contribute to the broader goal of reducing our reliance on fossil fuels and promoting a greener energy landscape.



เอกสารนี้เป็นเอกสารที่สงวนไว้สำหรับการใช้งานเพื่อการศึกษาเท่านั้น ไม่อนุญาตให้นำไปใช้ประโยชน์ด้านการค้า
ไม่ว่ากรณีใดๆ ทั้งสิ้น อีกทั้งห้ามมิให้ดัดแปลงเนื้อหา และต้องอ้างอิงถึงเจ้าของเอกสารทุกครั้งที่มีการนำไปใช้

2.2 General Background and Literature Review

2.2.1 Lignocellulose Biomass

Lignocellulose biomass is an organic compound derived from plants. It consists of carbohydrate polymers such as cellulose and hemicellulose, as well as an aromatic compound called lignin. Through the process of photosynthesis, plants convert solar energy, carbon dioxide, and water into sugars (hexose) and oxygen, as shown in

Equation 2-1.[135] This solar energy is stored as chemical energy within the biomass.



Lignocellulose biomass is the most abundant renewable fuel source and can be converted into usable energy through chemical, physical, and biological processes. These energy sources are predominantly utilized in the production of biofuels and biochemicals. Cellulose, **Figure 2.1**, a linear sugar polymer composed of D-glucose linked by β -1,4-glucosidic bonds, serves as a major component of plant cell walls, providing structural strength. Its degree of polymerization can reach up to 10,000 monomer units. Cellulose finds application primarily in paper production which be hydrolyzed into bioethanol, a valuable biofuel.[136]

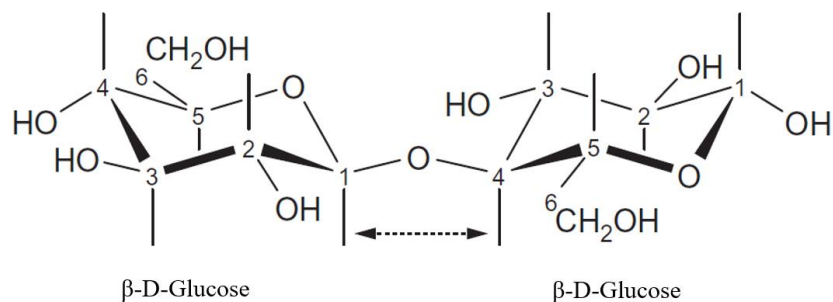


Figure 2.1 The fundamental unit of cellulose.[135]

Hemicellulose, on the other hand, is a heteropolymer composed of various monomers such as glucose, mannose, galactose, xylose, arabinose, 4-O-methyl glucuronic acid, and galacturonic acid residues. It typically consists of 500 to 3000 units connected by branches and coexists with cellulose in plant cell walls.[136]

Lignin, the second most abundant resource in the world, contributes to the mechanical strength properties of plant tissues, providing rigidity and hardness. Lignin's structure consists of randomly cross-linked phenolic units, primarily composed of three monomers: p-coumaryl alcohol, coniferyl alcohol, and sinapyl alcohol (**Figure 2.2**). The bond between each monolignol typically presents at the β -positions.[137] The linkages between these monomers are typically ether linkages (solid squares) and condensed linkages (dot squares), as depicted in **Figure 2.3**.[138]

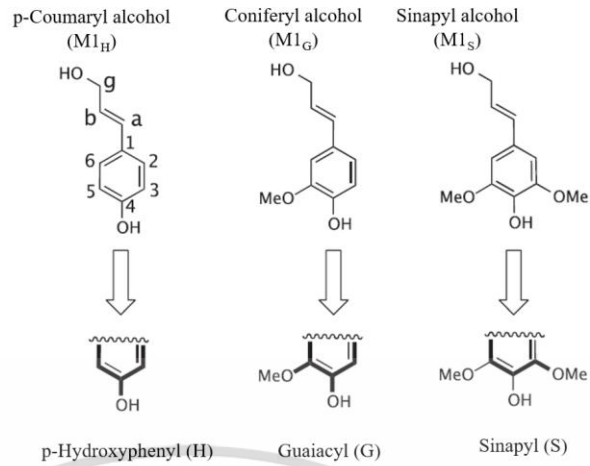


Figure 2.2 Monomers in lignin.[137]

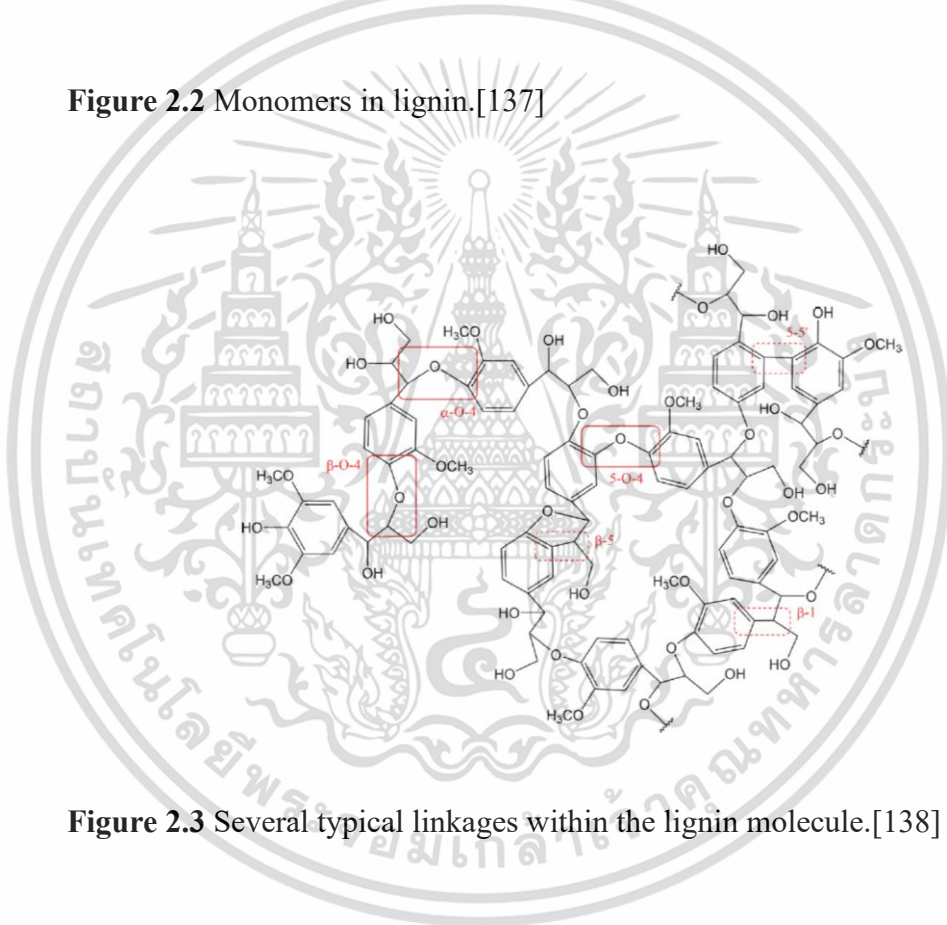


Figure 2.3 Several typical linkages within the lignin molecule.[138]

Different types of natural lignin can be classified based on plant taxonomy and the proportion of basic phenolic units. The classification based on plant taxonomy includes angiosperm lignins (from hardwood plants), gymnosperm lignins (from softwood plants), and grass lignins (from herbaceous plants). However, lignin classification based on phenolic units includes four groups: Type-G, Type-G-S, Type-

H-G-S, and Type-H-G. The composition of lignin monomers varies depending on the specific nature of the plants, as shown in **Table 2.1**.

Table 2.1 The Proportion of Lignin Monomers in Woods and Herbaceous Plants.[138]

Type	p-Coumaryl alcohol	Coniferyl alcohol	Sinapyl alcohol
Softwood	<5%	>95%	0%
Hardwood	0% – 8%	25% – 50%	45% – 75%
Herbaceous plants	5% – 55%	35% – 80%	20% – 25%

Lignin has several favorable properties, such as being a natural antioxidant, a free radical scavenger, and its ability to bind to cations. It has versatile applications, including the production of high-value compounds. Lignin can be combined with other substances to form lignin-based biopolymers with antioxidant capacity, or it can be broken down to obtain vanillin. In the construction field, lignin can be used as a binder in concrete to prevent the lumping and settling of particles. Furthermore, lignin can be transformed into an emulsifier for diesel-water fuel.[139]

2.2.2 Separation Methods of Lignin from Wood

Several methods are used to isolate lignin from wood, which can be categorized into three main groups: chemical, physical, and biological, or a combination of these approaches. This section describes some separation techniques, including lignin hydrolysis extraction, Brauns lignin, milled wood lignin, ethanol organosolv lignin, and thermochemical methods.

(1) Lignin Hydrolysis Extraction

The Klason lignin method is a simple and widely used technique in the paper and pulp industry for isolating lignin from wood. Undesired components such as waxes, fats, resins, and wood gums are first extracted using alcohol-benzene for cleaning purposes. Then, a 64–75% sulfuric acid solution is added to hydrolyze the carbohydrates in cellulose. The hydrolyzed wood is diluted with water, and the mixture is boiled in a water bath with a reflux condenser. Lignin settles down and forms a black solid, which is then filtered. The Klason lignin method offers high accuracy and ease of use. However, it may alter the structure of lignin during the hydrolysis process.[140] Another method, known as the Willstatter lignin method, is similar to the Klason method, but hydrochloric acid is replaced with sulfuric acid.[141]

(2) Brauns or Native Lignin (BNL)

In the Brauns lignin method, wood is crushed in a Wiley mill machine, and wood chips of 100 to 150 mesh size are selected. The wood chips are first extracted with cold water, followed by extraction with ethyl ether for 48 h to isolate the exterior components. Ethanol is then added to the solution at room temperature and left for 8 to 10 days, or until the solution becomes clear. Calcium carbonate is used to neutralize the pH of the solution. The alcohol is removed using a vacuum evaporator, and water is added to the residue. Evaporation is continued to remove the remaining alcohol residues. The lignin residue is ground using a pestle and mortar, gradually adding water and anhydrous ether until it solidifies. The solid is filtered using a vacuum filter, and the liquid is dried with an efficient desiccant. The dried lignin is extracted with anhydrous

ether in a Soxhlet apparatus. The aqueous residue is dissolved in dioxane to create a 10% solution, which is then precipitated by dripping it into stirred distilled water (approximately 15 times the volume of dioxane). The lignin solution in ethanol is precipitated using a solvent until the methoxyl group content becomes constant. This method typically yields around 8% of lignin from wood. The advantage of the Brauns or native lignin method is that it minimally alters the structure of lignin. Characteristics of BNL include similar elemental compositions, low molecular weight, large amounts of ester groups, and higher phenolic hydroxyl content.[142]

(3) Milled Wood Lignin (MWL)

The Milled Wood Lignin (MWL) method, also known as the Bjorkman method, involves extensive grinding followed by solvent extraction. This method allows for the extraction of a significant amount of lignin. Initially, the wood is treated with ethanol-benzene to remove extractives. Subsequently, the wood is subjected to vibration ball milling together with a non-swelling solvent such as toluene (under nitrogen for at least 48 h). The solvent added to the ball mill aids in lignin extraction and reduces the formation of cake on the milled balls. The next step involves extraction with solvents. The ball-milled wood is extracted twice with aqueous dioxane for 24 h under a nitrogen atmosphere. The mixture is then slowly added dropwise to deionized water while stirring, followed by freeze-drying. The freeze-dried crude lignin is dissolved in 90% acetic acid and deionized water to precipitate the lignin. The solution is centrifuged to remove the supernatant, and the solid is dissolved in 1,2-dichloroethane/ethanol and precipitated in diethyl ether. The mixture is centrifuged, and the solid is washed twice

with petroleum ether. Finally, MWL is obtained. The yield of lignin obtained is

เอกสารนี้เป็นเอกสารที่สงวนไว้สำหรับการใช้งานเพื่อการศึกษา 69 เท่านั้น ไม่อนุญาตให้นำไปใช้ประโยชน์ด้านการค้า

ไม่ว่ากรณีใดๆ ทั้งสิ้น อีกทั้งห้ามมิให้ดัดแปลงเนื้อหา และต้องอ้างอิงถึงเจ้าของเอกสารทุกครั้งที่มีการนำไปใช้

approximately 50% of the wood. The lignin appears as a white powder and may contain some carbohydrate compounds.[142-144]

(4) Organosolv Lignin

The organosolv method is an environmentally friendly and cost-effective process for lignin extraction. It involves using organic solvents with an acid or base catalyst to extract lignin. Various organic solvents can be employed, including alcohols, acetone, benzyl alcohol, glycerol, glycols, phenol, acetic acid, formic acid, propionic acid, diethyl ether, amines, esters, ethers, formaldehyde, chloroethanol, either in pure form or as aqueous solutions. In the case of ethanol organosolv lignin, lignocellulose is treated with 35% ethanol containing sulfuric acid at 190 °C for 1 h. The treated sample is washed three times with 50 mL of aqueous ethanol. Then, 3 volumes of water are added to precipitate the lignin. The ethanol organosolv lignin is centrifuged and dried. Organosolv lignin typically exhibits a low molecular weight and high phenolic and aliphatic hydroxyl contents.[145,146]

(5) Thermochemical Method

The thermochemical method involves subjecting lignin to external heating (pyrolysis), which leads to the degradation of lignin due to the increase in temperature and the breakdown of chemical bonds. This method enhances the depolymerization of the lignin structure. Pyrolysis is a thermal process that treats organic compounds in the absence of oxygen. Without oxygen, organic compounds cannot be converted to carbon

dioxide. The conditions of pyrolysis affect the structure of lignin. Typically, lignin produced through this process consists of low molecular weight lignin fragments. If lignin is gasified at high temperatures during pyrolysis, the resulting products include hydrogen, carbon dioxide, carbon monoxide, and methane. Therefore, temperature selection is crucial. At temperatures between 150 °C and 400 °C, the products of depolymerization usually consist of basic lignin units such as 4-methylguaiacol, syringol, coniferyl alcohol, and other lignin-derived chemicals. At higher temperatures (above 450 °C), most of the linkages are cleaved, resulting in the formation of o-vanillin, guaiacol, o-quinone methide, and lower molecular weight substances.[138]

2.2.3 *Techniques for Characterizing Lignin*

Characterizing lignin involves the use of various techniques, particularly when examining lignin in solution. The composition and chemical structure of lignin can vary depending on factors such as its source, type, and isolation method.[147] Several techniques are commonly employed for lignin characterization.

Ultraviolet-visible (UV-visible) spectrophotometry is a convenient and widely used method for analyzing lignin in solution. Due to its aromatic structure, lignin strongly absorbs ultraviolet light. This technique is valuable for both quantitative and qualitative analyses of lignin. UV-visible spectrophotometers measure the intensity of light passing through a sample in a cuvette (I) and compare it to the intensity before passing through the sample (I_0). Transmittance, expressed as (%T), is the ratio I/I_0 . Absorbance (A) is calculated using the equation $A = -\log(\%T/100\%)$. Liquid samples prepared by dissolving lignin in suitable solvents, such as water, ethanol, dimethylformamide, dioxane, pyridine, and dimethyl sulfoxide (DMSO), are

commonly used for analysis. For example, the lignin UV spectra of pine from various extraction techniques are shown in **Figure 2.4**. The UV spectrum of lignin reveals its aromatic nature, with absorption peaks around 280 nm indicating the presence of hydroxyl or methoxyl groups on the substituted benzene ring.[148]

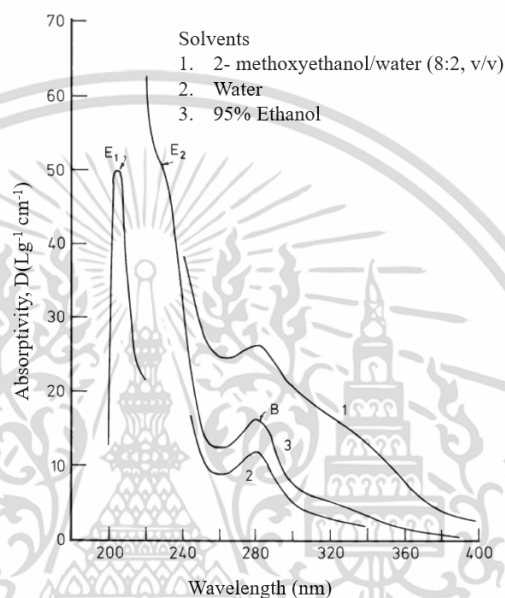


Figure 2.4 Ultraviolet spectra of (1) pine kraft lignin in 2-methoxyethanol/water (8:2, v/v), (2) spruce liginosulfonate in water, and (3) milled wood lignin in 95% ethanol.[147]

Fourier Transform Infrared (FT-IR) spectroscopy is another valuable technique for rapid and accurate lignin analysis. It operates by measuring the absorption of specific frequencies of the electromagnetic spectrum by molecular vibration modes. FT-IR spectroscopy provides information about the functional groups present in lignin and is commonly employed to analyze its composition and identify specific functional groups. For instance, the FT-IR spectrum of kraft lignin derived from ponderosa pine

(Figure 2.5) exhibits characteristic peaks at specific wave numbers, such as 3409 cm^{-1} (OH stretching), 1594 cm^{-1} (symmetric aryl ring stretching), 1512 cm^{-1} (asymmetric aryl ring stretching), 1463 cm^{-1} (asymmetric C–H deformation), 1266 cm^{-1} (aryl ring vibrating), and 1030 cm^{-1} (aromatic CH in-plane deformation). These peaks serve as indicators of lignin and aid in its identification.[147,148]



Figure 2.5 FT-IR spectrum of a softwood kraft lignin derived from ponderosa pine.[147]

In addition, Nuclear Magnetic Resonance (NMR) spectroscopy is a powerful technique for characterizing and classifying lignin, as well as determining its structure. This method relies on the interaction between a magnetic field and atomic nuclei, such as ^1H , ^{13}C , and ^{15}N , and the use of radio frequency pulses to observe the resonant frequency of these nuclei based on their local environment. NMR spectroscopy provides valuable insights into the chemical structure of lignin, allowing for differentiation between different types and variations in its structure. By analyzing the resulting signals, NMR spectroscopy enables the characterization and classification of lignin-based on its unique properties.[147,148]

Other techniques, such as gas chromatography-mass spectrometry (GC-MS) and size-exclusion chromatography (SEC), can also be employed for lignin characterization. GC-MS allows for identifying and quantifying lignin-derived compounds, providing information about their chemical composition. SEC, on the other hand, separates lignin based on its molecular size, offering insights into its distribution and average molecular weight. These related techniques allow for a thorough characterization of lignin, enabling researchers to study its structure, composition, and properties in various applications.[149]

2.2.4 Effect of Microwave on Biomass

Microwave heating has emerged as an alternative method for heating, replacing conventional heating methods in lignin and biomass thermochemical conversion. Microwaves are electromagnetic spectrum energy waves that have frequencies between 0.3 and 300 GHz. When microwaves pass through a material, they are converted to specific frequencies that can be absorbed by the material. The electric fields generated by microwaves cause alignment and realignment of dipoles in polar liquids, leading to friction and the generation of internal energy. Unlike conventional heating, where heat is transferred to the material through convection and conduction, microwave heating directly generates heat inside the material by passing through the walls of the heating container. This results in more uniform and efficient heating compared to conventional methods.[130]

In the context of biomass treatment, microwave heating has effects similar to thermal treatment. Lignin and cell walls become weakened as a result of the rise in

temperature and pressure. Hydrogen bonds are broken by microwaves by forcing dipoles to align with the oscillating electric field. The effects of microwave treatment primarily focus on the fractionation of lignocellulose. The radiation waves break down the crystalline structure of cellulose molecules, reducing the particle size of lignocellulose. As a result, the increased surface area of lignocellulose facilitates better diffusion when in contact with a solvent. Microwave irradiation also leads to the fragmentation of the lignocellulosic structure, enhancing the efficiency of delignification in various isolation methods such as pyrolysis, solvolysis, and hydrolysis using alkaline or acid mediums.[130,150]

2.2.5 *Microwave Heating of Organic Solvents*

Microwave radiation at a frequency of 2.45 GHz is commonly used due to its avoidance of interference with telecommunication and cellular phone frequencies. It has a significant impact on the rate of many processes in the chemical and food industry and finds application in extraction processes. Materials can be categorized based on their interaction with microwaves into three groups: microwave-reflected materials (bulk metals and alloys), microwave transparent materials (such as fused quartz, borosilicate glasses, ceramics, and Teflon), and microwave-absorbed materials (including aqueous solutions and polar solvents).[151]

The rate of energy transfer during microwave heating depends on the strength of the field generated within the material, the frequency of the radiation, and the material's loss factor. The dielectric constant (ϵ) indicates the material's capacity to store energy from the applied field, while the loss factor (ϵ'') represents its ability to dissipate this energy as heat. The dissipation factor (also known as the loss tangent, $\tan \delta$) is the

ratio of the dielectric loss to the dielectric constant. The efficiency of a material in converting microwave energy into heat can be explained by its dissipation factor. Generally, materials with higher ϵ and ϵ'' values exhibit faster heating rates compared to those with lower values. Furthermore, the dielectric loss and the dielectric constant in the liquid phase are higher compared to other phases and decrease as the liquid temperature increases.[152]

Dipolar polarization, ionic conduction, and interfacial polarization are the three ways that microwaves move energy through materials. These processes help materials quickly superheat when exposed to microwaves (**Figure 2.6**). In conventional heating, the boiling point of a solvent at atmospheric pressure is reached when the partial vapor pressure equals ambient pressure. However, in microwave irradiation, the boiling point can be higher than the normal boiling point. The microwave energy is dissipated throughout the solvent's entire volume, leading to the formation of tiny bubbles from nucleation points. The high internal vapor pressure generated resists the surface tension, causing the boiling point to exceed the normal boiling point and resulting in superheated solvents.[153]

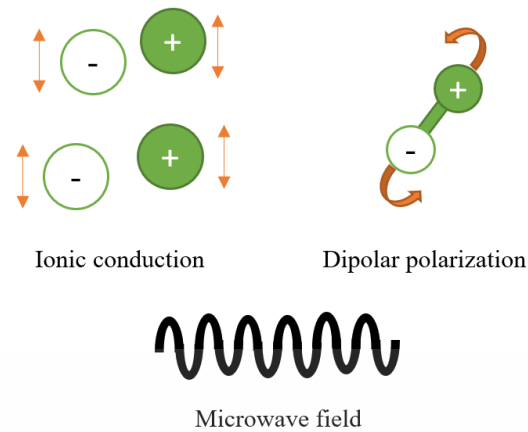


Figure 2.6 Ionic conduction and dipolar polarization under microwave conditions.[153]

2.2.6 *Softwood and Hardwood*

Woods can be classified into two broad categories: hardwoods and softwoods.[154]

- (1) Gymnospermae (gymnosperms) - These trees have naked seeds.
- (2) Angiospermae (angiosperms) - These trees have seeds enclosed within the ovary of the flower.

Softwood comes from gymnosperm trees and is nonporous, typically having needles and cones. Medullary rays and tracheids are responsible for water transportation and sap production.[154] Softwood with long lengths and slender fibers is preferred as raw materials for strong papers and as reinforcement components. Low-density softwoods contain thin-walled fibers and are suitable for papers that need high bonding-related strength qualities including tensile, burst, and surface strength.

Examples of these species include different spruces, firs, Scots pine, and lodgepole pine. Slash pine, loblolly pine, longleaf pine, and shortleaf pine are examples of high-density softwoods that offer improved tear strength and bulk, making them perfect for generating sheets with high bending stiffness.[154]

Hardwoods are angiosperm trees characterized by the presence of vessels (pores). Vessels are long tubes that may extend throughout the length of the tree and are responsible for water or sap conduction from roots to stems or leaves.[154] Hardwoods are generally plants with broad leaves, but they shed their leaves during winter or autumn. Most tropical woods belong to the hardwood category. Hardwoods are the chosen raw materials for pulp used in printing papers. Due to the smaller size of hardwood fibers, there are more fibers per mass of pulp, which results in the production of desirable properties such as small-scale homogeneity, opacity, and surface smoothness, which are crucial for printing papers.[155]

2.2.7 *Rubber Tree*

The rubber tree (*Hevea brasiliensis*) is primarily cultivated for latex production in tropical regions, particularly Southeast Asia and Western Africa. Thailand, Indonesia, and Malaysia are the largest natural rubber producers in Southeast Asia, with Thailand being the major cultivator (68%) in the region. The economic lifespan of rubber trees used for latex production ranges from 20 to 30 years. Once latex production declines in older trees, they are annually cut down for replanting. Rubberwood, obtained from these trees, is commonly used in the manufacturing of furniture, particle boards, and plywood. Large branches are utilized for charcoal production, while small branches, stumps, and roots are burned to prepare the land for replanting. The chemical composition of

rubberwood includes cellulose (39–42%), hemicellulose (29–32%), and lignin (18–21%).[154,156]

2.2.8 Literature Review

The utilization of lignin fractionation for biomass extraction using the organosolv solvent extraction method has been studied since 1968.[157] Over the years, different methods and conditions have been continuously explored. For instance, YU Hai-bo et al.[131] (2013) investigated the extraction of polyphenols from grape peel using alcohol solvents with acid catalysis or without any catalyst, along with the use of microwave heating. The study found that the process took 1–5 min, with varying microwave power levels of 180, 360, and 540 W, and ethanol concentrations of 40–60%. The optimal conditions were determined as 50% ethanol, 3 min of extraction time, and 540 W of microwave power, which resulted in the highest polyphenol extraction efficiency.

Another study conducted by Saksit Imman et al.[132] (2015) focused on lignin separation from rice straw using a single-step solvothermal process. The effects of different solvents, acid promoters, and microwave treatment were investigated. In order to achieve reaction temperatures of 140, 160, and 180 °C, respectively, the microwave power was adjusted at 200, 300, and 450 W. The study contrasted conventional heating techniques with microwave-assisted heating techniques. The findings obtained utilizing the traditional heating procedure at 180 °C without any acid promoter were comparable to those obtained at 450 W, which led to the maximum lignin recovery of 53.0%.

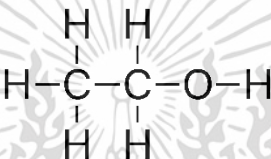
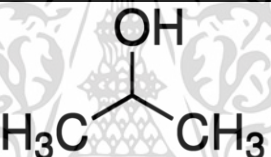
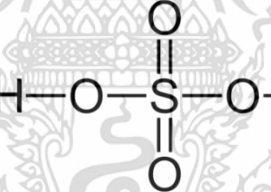
In the study by Fanny Monteil-Rivera et al.[158] (2012), microwave-assisted extraction of lignin from triticale straw was investigated. The process involved varying the ethanol fraction (27–95%), microwave temperature (83, 100, 125, 150, 167 °C), and sulfuric acid concentration (0–1 N). The highest lignin yield of 91% was obtained using 92% ethanol, 0.64 N sulfuric acid, and a temperature of 148 °C.

Dengle Duan et al.[126] (2017) examined the depolymerization of ethanol organosolv lignin using alcohols and microwave heating. The lignin was mixed with alcohol and sulfuric acid as a catalyst and the process was carried out at 160 °C for 30 min, while maintaining a pressure and power below 220 psi and 100 W, respectively. Ethanol showed a conversion rate of 84%, whereas isopropanol showed a rate of 27%. This experiment also considered the presence of moisture and acid in the extracted lignin, as water can pose challenges for future utilization. For example, water contamination in gasohol can decrease efficiency and cause engine damage. High water content can lead to phase separation between ethanol and gasoline, where the water will begin to remove the ethanol from the gasoline.[159] However, Gupta P. et al.[160] demonstrate the economic advantage of water contents mixture with ethanol as fuel on SI engines in cases less than 20%.

2.3 Methodology

2.3.1 Materials

Table 2.2 Chemicals Used In this Work.

Name Chemical Formula	Structure	Purity	Source
Rubberwood sawdust	N/A	N/A	Sri Incese (Thailand) Co., LTD
Ethanol C ₂ H ₆ O		95%	Chemipan
Isopropanol C ₃ H ₈ O		99.8%	Chemipan
Sulfuric acid H ₂ SO ₄		95–97%	Merck

2.3.2 Solvent Extraction with Microwave-Assisted Method

The sawdust underwent 24 h at 105 °C in an oven to assure its dryness. Until it was required for the experiment, it was then kept in a sealed plastic container to avoid moisture absorption. Microwave-assisted extraction of lignin from the biomass was carried out. For the procedure, a 500 mL Erlenmeyer flask was employed. A 1:10 weight ratio of ethanol or isopropanol was used to combine the dry rubberwood sawdust (5 g).

The flask was shaken before being put in a modified microwave (SAMSUNG

GE711K/XST Microwave, Thai Samsung Electronics Co., Ltd., Bangkok, Thailand) with the right power settings (750 W, 20 L, 2.45 GHz) (see **Figure 2.7**). A plastic cover served as the condenser seal. Different extraction powers (100 W and 200 W) and periods (five to thirty min, with five-min intervals) were used. Vacuum filtration was used to separate the solid fraction from the mixture after extraction. While the liquid solution was gathered for further determinations, the solid residue was dried in a Petri dish at 105 °C.

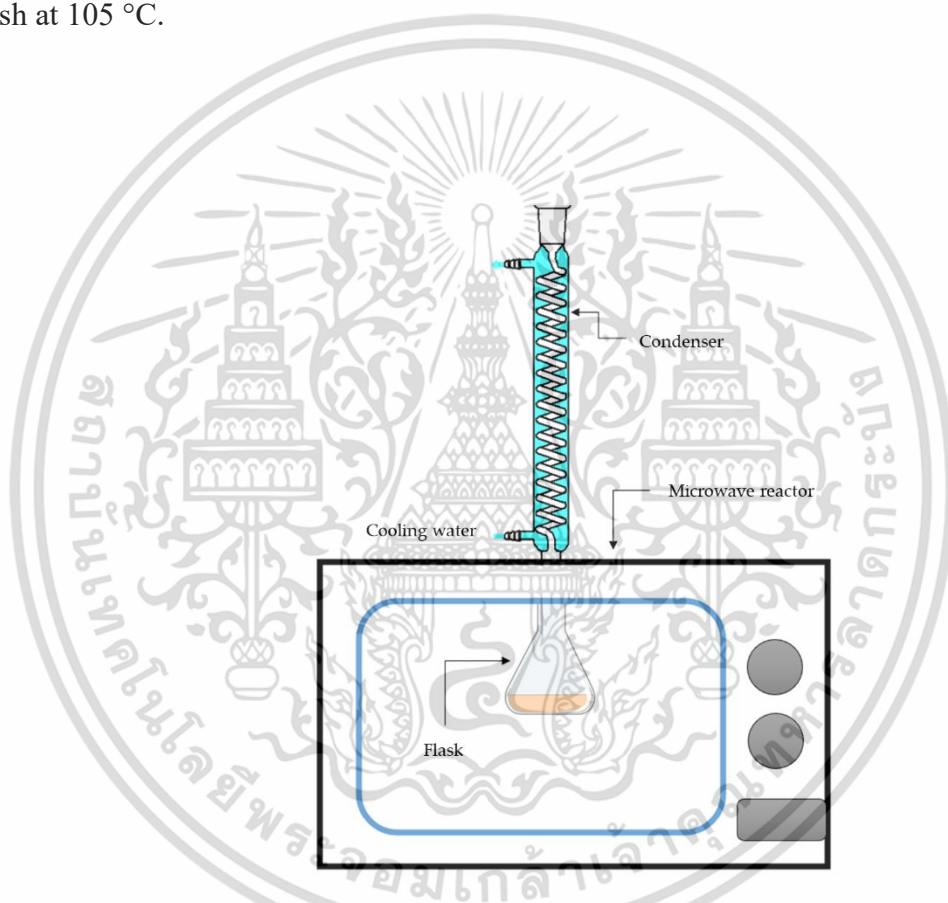


Figure 2.7 Schematic diagram of the modified microwave oven.

2.3.3 *Klason Lignin Analytical Method*

In this procedure, 15 mL of 72% sulfuric acid was added to 1 g of dried wood, and the mixture was agitated with a glass rod. After that, the mixture was covered with

a watch glass and placed in water for two h. Then, the fluids of the beaker were moved

เอกสารนี้เป็นเอกสารที่สงวนไว้สำหรับการใช้งานเพื่อการศึกษา 82 เท่านั้น ไม่อนุญาตให้นำไปใช้ประโยชน์ด้านการค้า
ไม่ว่ากรณีใดๆ ทั้งสิ้น อีกทั้งห้ามมิให้ดัดแปลงเนื้อหา และต้องอ้างอิงถึงเจ้าของเอกสารทุกครั้งที่มีการนำไปใช้

to a 1000 mL flask, which had 300–400 mL of water added to it. Rinse water was used to dilute the solution to a final volume of 575 mL. The flask was then put through 4 h of reflux to keep its volume constant. By leaving the flask in an inclined position for 12 h, lignin was precipitated.

Vacuum filtration was used to filter the mixture, and any leftover acid was then rinsed out of the precipitated lignin. The filter paper's lignin was dried for 24 h at 105 °C in an oven[161]. Finally, **Equation 2-2** was used to determine the amount of lignin in the dry wood (also known as Klason lignin).

$$\text{Lignin \%} = A \times 100 / W \quad \text{Equation 2-2}$$

where,

Lignin % is the lignin content in the wood sample.

A is the weight of lignin (g).

W is the dry weight of the test specimen (g).

2.3.4 Ultraviolet-Visible Spectrophotometry (UV-vis) Analytical Method

The solution samples were evaluated with a UV-visible spectrophotometer (Thermo Evolution 201, Madison, WI, USA) for UV-visible spectrophotometry analysis. First, 2.7 mL of ethanol and 0.3 mL of the lignin sample were combined in a quartz cuvette. The sample's absorbance was then assessed at wavelengths between 200 and 400 nm. By comparing the weight of the extracted lignin to a standard curve generated from a UV-visible spectrophotometer, the weight of the lignin was calculated.

As determined by the Klason method (0.02064 g of lignin per gram of rubberwood

sawdust), the yield of recovered lignin was also compared to the total amount of lignin found in rubberwood. **Equation 2-3** was used to get the yield % of the extracted lignin.

$$Yield_{Lignin} = \frac{W_{ExtractedLignin}}{W_{TotalLignin}} \times 100\% \quad \text{Equation 2-3}$$

where,

$W_{ExtractedLignin}$ is the weight of the extracted lignin (g).

$W_{TotalLignin}$ is the weight of lignin present in the feedstock (g).

2.3.5 *Characterization Method Using Fourier Transform Infrared Spectroscopy (FT-IR)*

The Attenuated Total Reflectance (ATR) technique was used to examine the produced samples. The FT-IR data were acquired using an FT-IR spectrometer (Nicolet iS20, Madison, WI, USA) with a spectral resolution of 4 cm^{-1} and a range of 4000 to 700 cm^{-1} at Sci-Ins, King Mongkut's Institute of Technology, Ladkrabang.

2.3.6 *Heteronuclear Single Quantum Coherence Spectroscopy (2D HSQC NMR) Characterization Method*

40 mg or 0.6 mL of the samples were diluted in 0.5 mL of methanol-d4 for the 2D HSQC NMR analysis. The NMR spectra were collected using a JEOL JNM-ECZR 500 MHz, Tokyo, Japan, NMR spectroscopy apparatus from Sci-Ins, King Mongkut's Institute of Technology, Ladkrabang. For the ^1H - and ^{13}C -dimensions, the spectral

widths were 6 ppm and 100 ppm, respectively. The data were gathered using 8 scans, an acquisition time of 0.164 seconds, and a relaxation delay of 1 second. The dimension size was 256 x 819 points. The frequency of $^1J_{CH}$ was 145 Hz.

2.3.7 Bomb Calorimeter Characterization Method

20–50 mL of the extracted solution had to be prepared for the bomb calorimeter testing in a stainless-steel jar with oxygen provided. The temperature was then set to a range of 18 °C to 24 °C, and the vessel containing the sample of the solutions was placed inside the calorimeter. At STREC, Chulalongkorn University, the higher heating value (HHV) was determined using a LECO AC500 Isoperibol calorimeter.

2.4 Results and Discussion

2.4.1 Microwave-Assisted Extraction of Lignin

Figure 2.8 demonstrates the percentage of recovered lignin from deconstructed biomass, achieved by employing various solvents and microwave power settings in a microwave oven. The utilization of isopropanol as the solvent resulted in the lowest yield of extracted lignin, mainly due to its inadequate solubility for lignin. Conversely, ethanol exhibited higher effectiveness in delignification as it facilitated a faster rate of delignification compared to isopropanol. Even at 100 W, ethanol yielded a higher extraction of lignin, primarily because primary alcohols, such as ethanol, possess greater selectivity in delignification compared to secondary and tertiary alcohols.[162] Furthermore, lower molecular weight of ethanol enhanced its permeability and fluidity.[126] The hydroxyl group present in alcohols demonstrates nucleophilic reactive capabilities[163], enabling the decomposition of the glycosidic bond in cellulose and the ether bond in lignin. The highest concentration of lignin was achieved when using ethanol as the solvent, with the microwave power set to 200 W for 30 min.

In contrast, isopropanol yielded a significantly lower extraction of lignin, reaching a maximum of only 2.72 percent, while ethanol yielded 6.26 percent under identical conditions. Although isopropanol potentially reached higher temperatures in the microwave, its solubility capacity had a more substantial impact.

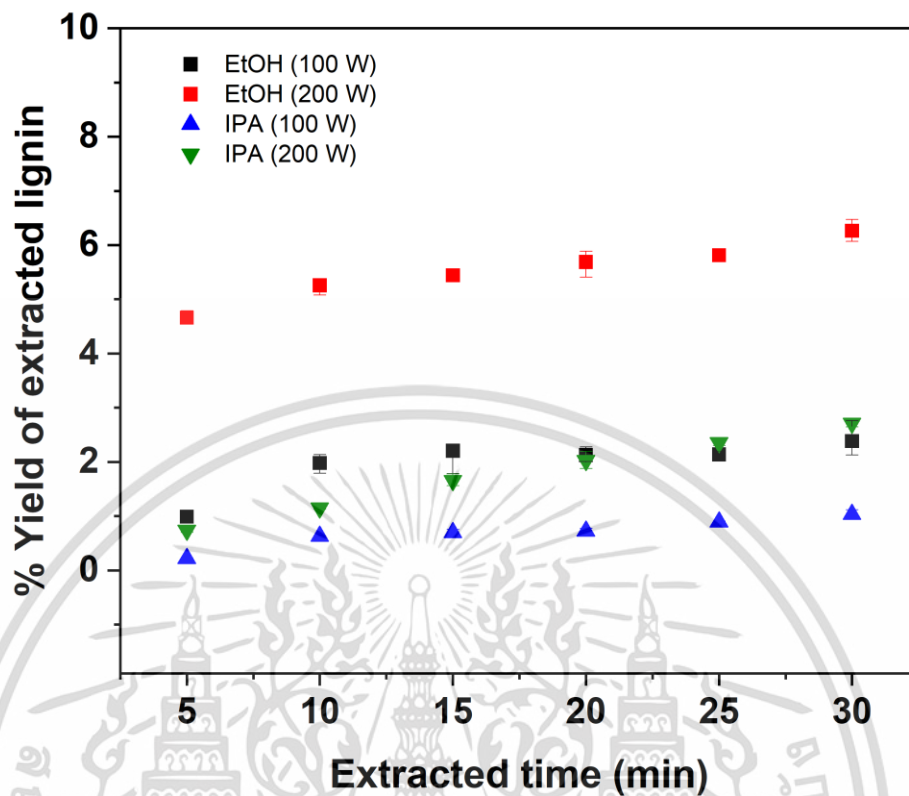


Figure 2.8 The percentage yield of extracted lignin.

Microwave power directly influences the temperature during the extraction process. Higher microwave power results in higher boiling points for solvents. Solvents such as ethanol and isopropanol have low boiling points. According to studies conducted by Farid Chemat and Erik Esvelde[153], the boiling point of 20 mL of ethanol reached approximately 12 K more than normal boiling point during microwave operation at 100 W. The solubility of most substances increases with rising temperature. As microwave power increases, the solubility of lignin in the solvent also increases. Moreover, increasing temperature reduces the viscosity of alcohol solvents and improves their diffusivity, facilitating effective interaction with lignocellulosic materials. Consequently, higher microwave power leads to higher lignin yields.

Increasing the microwave power from 100 W to 200 W resulted in lignin yields increasing from 2.38 percent to 6.26 percent in ethanol solvent after 30 min. In isopropanol, the lignin yield increased from 1.05 percent to 2.72 percent under the same duration. The duration of the extraction process also plays a role. At shorter extraction times (5 min), the lignin yield is low due to the lower reaction temperature, which is insufficient to break the strong bond between lignin and other components. However, with an increased extraction time, the lignin yield and biomass depolymerization efficiency improve.

It is important to note that this microwave-assisted method exhibits lower lignin extraction efficiency compared to the organosolv method. However, it offers the advantage of not requiring higher power settings, which would lead to rapid solvent evaporation and hinder reflux. Additionally, this method eliminates the need for acid or alkaline catalysts commonly used in the organosolv technique, thus minimizing waste products.

2.4.2 Analysis Using Fourier Transform Infrared Spectroscopy (FT-IR)

Comparisons of the FT-IR spectra between the extracted lignin, commercial organosolv lignin, and Klason lignin from rubberwood are presented in **Figure 2.9** and **Table 2.3**.

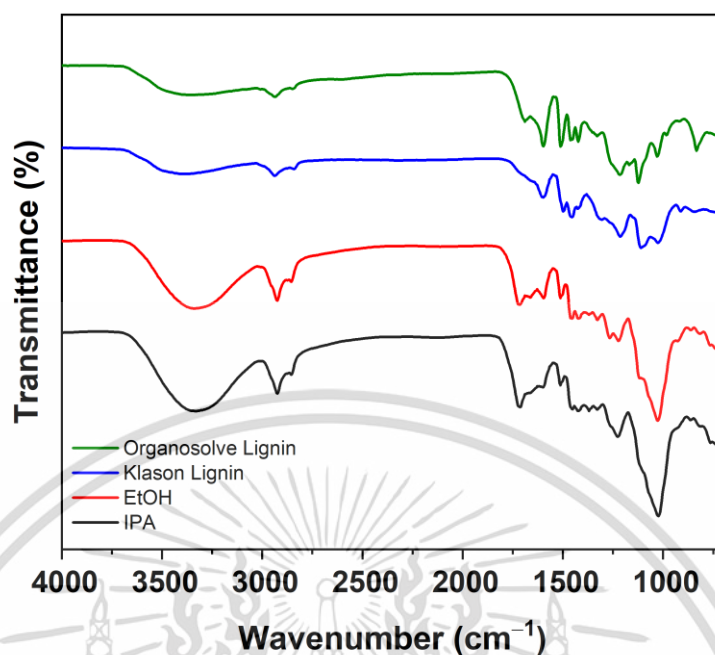


Figure 2.9 FT-IR spectra of lignin obtained through the organosolv method, Klason lignin, and solvents extraction using the microwave-assisted method.

The FT-IR results indicated no significant differences in the spectra of the extracted lignins when isopropanol and ethanol were used as solvents. However, the spectra of the Klason and organosolv methods differed from the extracted lignins obtained through this microwave-assisted extraction. In the 3680–3025 cm^{-1} range, a broad band represented the stretching vibration of O–H groups in aliphatic and aromatic hydroxy groups. The extracted lignin using isopropanol as the solvent exhibited higher relative intensities in this range, indicating a higher hydroxy group content. Furthermore, the lignin obtained from the Klason and organosolv methods, which involved the use of acid as a catalyst, showed lower oxidation compared to this extraction method. The peaks at 2930 cm^{-1} and 2850 cm^{-1} represented CH stretching in methyl and methylene groups, and C–H stretching in the O–CH₃ group, respectively.

เอกสารนี้เป็นเอกสารที่สงวนไว้สำหรับการใช้งานเพื่อการศึกษา 89 เท่านั้น ไม่อนุญาตให้นำไปใช้ประโยชน์ด้านการค้า

ไม่ว่ากรณีใดๆ ทั้งสิ้น อีกทั้งห้ามมิให้ดัดแปลงเนื้อหา และต้องอ้างอิงถึงเจ้าของเอกสารทุกครั้งที่มีการนำไปใช้

The peak at 1716 cm^{-1} corresponded to the C=O stretch of unconjugated carboxyl, ketone, and ester groups, which could be used to investigate the presence of lignin and remaining hemicellulose during extraction.[132,145] The peak at 1660 cm^{-1} indicated the stretching of conjugated carbonyl in lignin. The peaks at 1600, 1510, 1170, and 1420 cm^{-1} represented aromatic skeletal vibrations, while the peak at 1455 cm^{-1} indicated C–H deformation frequencies combined with aromatic ring vibration. The peaks in Klason and organosolv lignin showed more prominent peaks due to the precipitation of lignin in water during those methods. In contrast, in this method, the moisture in the solution needed to be considered. The phenolic hydroxyl group was identified by the absorbance at 3368 cm^{-1} , which indicated the breaking of $\beta\text{-O-4}$ bonds during extraction. This band suggested that microwave irradiation not only broke the bond connecting lignin with cellulose and hemicellulose but also broke the ether bond in lignin.[164] The peaks at 1265, 1226, and 833 cm^{-1} were related to guaiacyl units, which are the predominant monomers in rubberwood lignin. The absorbance at 1325 and 1126 cm^{-1} represented syringyl ring breathing and C–O stretching, respectively. The absorbance at 1026 cm^{-1} was assigned to the C–O–C mode of glycosidic linkages, indicating the presence of cellulose and hemicellulose in the solution.[145] The peak at 925 cm^{-1} indicated the presence of a pyranose ring in hemicellulose. The solutions obtained from both solvent extractions were rich in phenolic, carbonyl, and aromatic compounds. The spectra confirmed that the samples consisted of lignin, although they were contaminated with cellulose and hemicellulose residues remaining during extraction.

Table 2.3 The Assignment of FT-IR Bands.[132,145,165,166]

Wavenumbers (cm ⁻¹)	Assignments
3680–3025	O–H stretch, H–bonded
2930	C–H stretch methyl and methylene groups (aliphatic)
2850	C–H stretch O–CH ₃ group
1716	C=O stretch, unconjugated ketone, carboxyl, and ester groups
1660	C=O stretch conj.
1600	Aromatic skeletal vibration
1510	Aromatic skeletal vibration
1455	CH deformations and aromatic ring vibrations
1420	Aromatic skeletal vibration combined with C–H in plane deformation
1368	Phenolic hydroxyl group
1325	Syringyl ring breathing, C–O stretch
1265	C–C, C–O, and C=O stretches in guaiacyl
1226	Guaiacyl ring breathing
1170	Aromatic C–H in plane deformation
1126	Syringyl ring breathing
1026	C–O–C
925	C–H deformation of out of plane, aromatic ring, pyranose ring
833	Aromatic CH out of plane deformation G + S

2.4.3 Analysis Using Heteronuclear Single Quantum Coherence Spectroscopy (2D HSQC NMR)

The extracted lignins, Klason lignin, and organosolv lignin were analyzed using 2D NMR analysis to obtain information about the carbon-proton attachments. The side chain region of the lignin structure was revealed in the HSQC spectra, as shown in

Table 2.4.

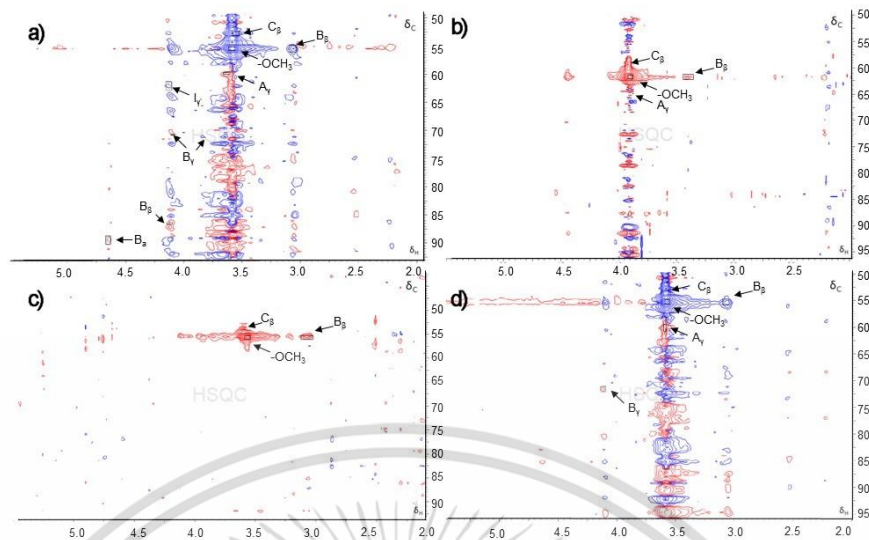


Figure 2.10 HSQC spectra ($\delta C/\delta H$ 50–95/2.0–5.5) of (a) extracted lignin solutions using ethanol, (b) extracted lignin solutions using isopropanol, (c) Klason lignin, and (d) organosolv lignin.

In the HSQC spectra, **Figure 2.10**, prominent peaks corresponding to methoxyl ($\delta C/\delta H$ 55.48/3.06) linkages were observed in all lignin samples. The resinol substructures (B) were identified by their C–H correlations for C_β – H_β , C_γ – H_γ , and C_α – H_α at $\delta C/\delta H$ 55.48/3.06, 70.79/4.10 & 71.21/3.82, and 89.47/4.65. The lignin extracted using ethanol as the solvent exhibited a high content of methoxyl and resinol substructures. β –O–4 substructures (A) were confirmed by C–H correlations at $\delta C/\delta H$ 59.83/3.63 and 86.52/4.12 for C_γ – H_γ and C_β – H_β . Phenylcoumaran substructures (C) and cinnamyl alcohol end-groups (I) showed some C–H correlations at $\delta C/\delta H$ 52.81/3.55 and 62.08/4.13, respectively. However, these correlations were detected at a low contour level, except for the methoxyls correlation, which had a strong spectrum. The

presence of numerous undesired peaks made it challenging to determine the C–H correlation of the lignin structure.

Table 2.4 The Assignment of Main Signals in the 2D HSQC NMR Spectra of Lignin.[167]

Labels	δ_C/δ_H	Assignment
C $_{\beta}$	52.81/3.55	C $_{\beta}$ –H $_{\beta}$ in phenylcoumaran substructures (C)
B $_{\beta}$	55.48/3.06	C $_{\beta}$ –H $_{\beta}$ in resinol substructures (B)
–OCH $_3$ (OMe)	55.48/3.58	C–H in methoxyls
A $_{\gamma}$	59.83/3.63	C $_{\gamma}$ –H $_{\gamma}$ in β –O–4 substructures (A)
I $_{\gamma}$	62.08/4.13	C $_{\gamma}$ –H $_{\gamma}$ in cinnamyl alcohol end- groups (I)
B $_{\gamma}$	70.79/4.10,71.21/ 3.82	C $_{\gamma}$ –H $_{\gamma}$ in resinol substructures (B)
B $_a$	89.47/4.65	C $_a$ –H $_a$ in resinol substructures (B)
A $_{\beta}$	86.52/4.12	C $_{\beta}$ –H $_{\beta}$ in β –O–4 substructures linked to a S unit (A)

2.4.4 Ultraviolet-Visible Spectrophotometry (UV-vis) Analysis

The UV spectra of the lignin solutions and Klason lignin were obtained, as shown in **Figure 2.11**.

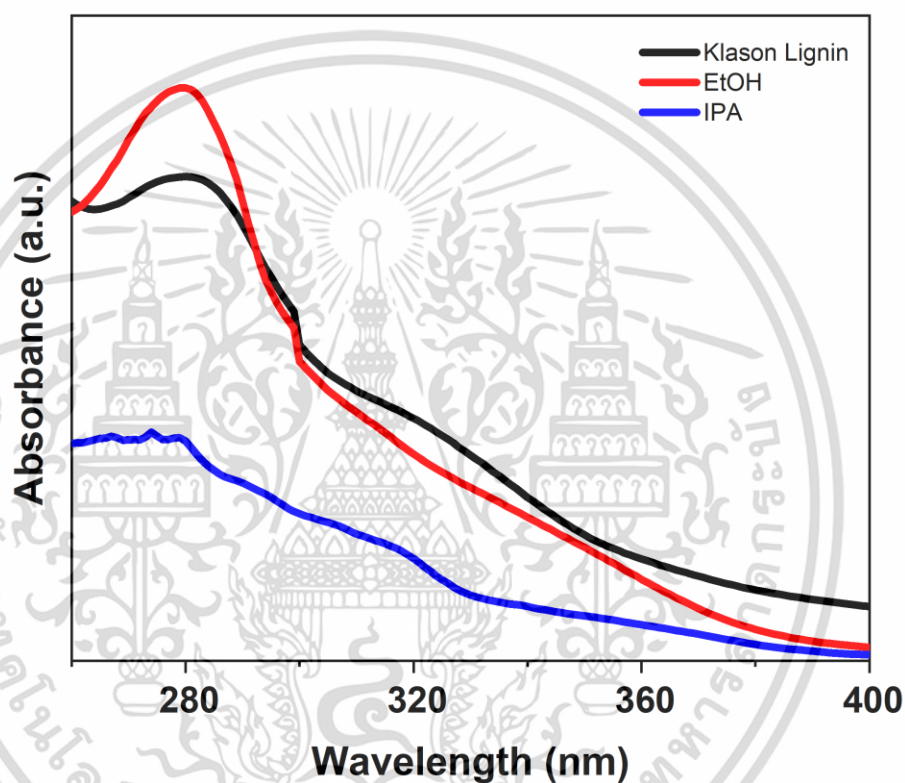


Figure 2.11 UV-visible spectra of the experimental lignins and Klason lignin.

The lignin solutions exhibited characteristic UV spectra of lignin, with the highest peak observed at 280 nm, indicating the presence of non-conjugated phenolic compounds.[148,168] Both extracted lignin solutions using different solvents showed a maximum peak at 280 nm, similar to the Klason lignin. However, the lignin extracted with isopropanol had a lower absorbance at 280 nm compared to the one extracted with

ethanol under the same conditions. This result suggests that ethanol as a solvent had higher extraction efficiency. Additionally, in the isopropanol-extracted solution, the absorbance at 208 nm indicated isopropanol absorption.

2.4.5 Higher Heating Value (HHV) Characterization

The higher heating value (HHV) of the extracted lignin solutions was compared to pure solvents (95.6% v/v ethanol and 99.8% v/v isopropanol), as illustrated in **Figure 2.12**. The optimized extraction conditions for the lignin solutions were a microwave power of 200 W and 30 min. The HHV of both extracted lignin solutions was lower than that of the pure solvent. The HHV of lignin typically ranges from 17000 to 25000 kJ/kg and depends on the molecular weight of lignin.[169] The heating value of lignin was lower than that of the pure alcohol solvents, indicating a decrease in HHV in the extracted lignin due to the presence of lignin and alcohol. The HHV of the ethanol-extracted lignin solutions was reduced by less than 9.86% compared to 95% ethanol, while the HHV of the isopropanol-extracted lignin solutions was reduced by less than 1.13% compared to isopropanol. It is worth noting that previous studies have explored the use of lignin as an additive in transportation fuel. The extracted solution, rich in hydroxyl, phenolic, carbonyl, and aromatic compounds, could potentially serve as an additive in gasoline and/or diesel.[170,171] However, further testing is required to assess the quality and performance of this extracted lignin, such as combustion performance tests, engine efficiency tests, emission tests, etc.

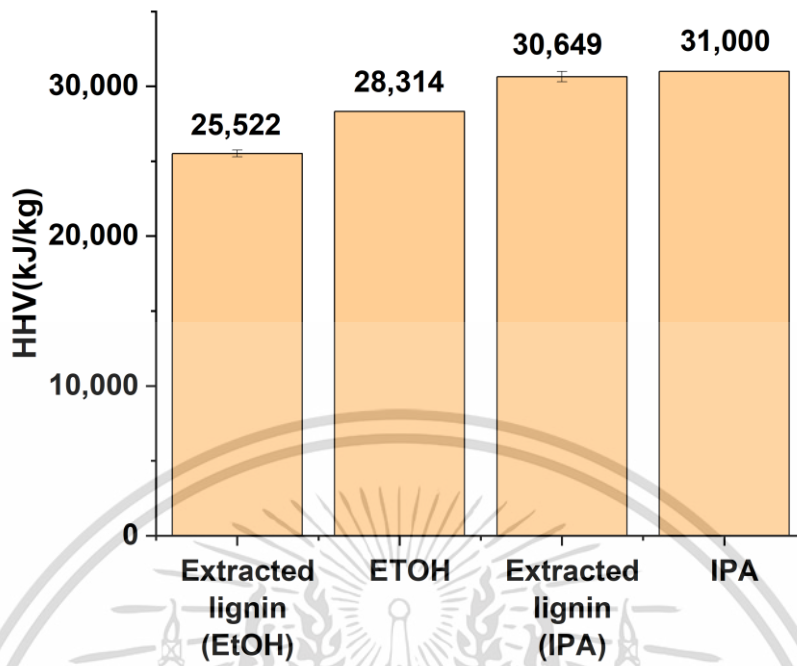


Figure 2.12 The higher heating value (HHV) of the extracted solutions compared to pure solvents.

2.5 Conclusion

This study investigated the microwave-assisted extraction of lignin using ethanol and isopropanol as solvents. Isopropanol demonstrated lower efficiency in lignin extraction due to its poor solubility, while ethanol showed faster and more selective delignification. The microwave power influenced the yield of extracted lignin, with higher power resulting in increased solubility and improved diffusion. The highest lignin concentration was achieved at 200 W for 30 min using ethanol as the solvent. The analysis of extracted lignins using FT-IR and 2D HSQC NMR confirmed their lignin composition, although they also contained cellulose and hemicellulose residues. UV-vis spectra indicated the presence of lignin-specific peaks, with similar profiles to Klason lignin. The extracted lignin solutions exhibited lower higher heating values (HHV) compared to pure alcohol solvents, suggesting potential applications as fuel additives. This microwave-assisted extraction method offers an alternative to traditional organosolv techniques, eliminating the need for acid or alkaline catalysts and reducing waste generation. Further research should focus on evaluating the extracted lignin's performance as a fuel additive, including combustion behavior, engine efficiency, and emission characteristics, to assess its viability in the transportation sector.

Overall, the findings of this study contribute to the understanding of microwave-assisted lignin extraction and its potential applications. By utilizing ethanol as a solvent and optimizing microwave power, higher yields of lignin can be achieved, offering a promising avenue for lignocellulosic biomass valorization and sustainable resource utilization.

REFERENCES

- [1] Pan, C., Nuzzo, R. G., & Gewirth, A. A. 2017. $\text{ZnAl}_x\text{Co}_{2-x}\text{O}_4$ Spinel as Cathode Materials for Non-Aqueous Zn Batteries with an Open Circuit Voltage of ≤ 2 V. *Chem. Mater.*, 29, 9351–9359
- [2] Zhang, L. Y., Chen, L., Zhou, X. F., & Liu, Z. P. 2015. Towards High-Voltage Aqueous Metal-Ion Batteries Beyond 1.5 V: The Zinc/Zinc Hexacyanoferrate System. *Adv. Energy Mater.*, 5, 1400930
- [3] Zhang, L., Chen, L., Zhou, X., & Liu, Z. 2015. Morphology-Dependent Electrochemical Performance of Zinc Hexacyanoferrate Cathode for Zinc-Ion Battery. *Sci. Rep.*, 5, 18263
- [4] Chae, M. S., Heo, J. W., Kwak, H. H., Lee, H., & Hong, S.-T. 2017. Organic electrolyte-based rechargeable zinc-ion batteries using potassium nickel hexacyanoferrate as a cathode material. *J. Power Sources*, 337, 204–211
- [5] Kundu, D., Vajargah, S. H., Wan, L. W., Adams, B., Prendergast, D., & Nazar, L. F. 2018. Aqueous vs. nonaqueous Zn-ion batteries: consequences of the desolvation penalty at the interface. *Energy Environ. Sci*, 11, 881–892
- [6] Lv, Y. Q., Xiao, Y., Ma, L. T., Zhi, C. Y., & Chen, S. M. 2022. Recent Advances in Electrolytes for "Beyond Aqueous" Zinc-Ion Batteries. *Adv. Mater.*, 34, 2106409
- [7] Pan, C., Zhang, R., Nuzzo, R. G., & Gewirth, A. A. 2018. $\text{ZnNi}_x\text{Mn}_x\text{Co}_{2-2x}\text{O}_4$ Spinel as a High-Voltage and High-Capacity Cathode Material for Nonaqueous Zn-Ion Batteries. *Adv. Energy Mater.*, 8, 1800589
- [8] Senguttuvan, P., Han, S. D., Kim, S., Lipson, A. L., Tepavcevic, S., Fister, T. T., Bloom, I. D., Burrell, A. K., & Johnson, C. S. 2016. A High Power Rechargeable Nonaqueous Multivalent Zn/ V_2O_5 Battery. *Advanced Energy Materials*, 6, 1600826
- [9] Guerfi, A., Trottier, J., Boyano, I., De Meatza, I., Blazquez, J. A., Brewer, S., Ryder, K. S., Vijn, A., & Zaghbi, K. 2014. High cycling stability of zinc-anode/conducting polymer rechargeable battery with non-aqueous electrolyte. *J. Power Sources*, 248, 1099–1104

- [10] Li, Y. X., Zhao, J. X., Hu, Q., Hao, T. W., Cao, H., Huang, X. M., Liu, Y., Zhang, Y. Y., Lin, D. M., Tang, Y. X., & Cai, Y. Q. 2022. Prussian blue analogs cathodes for aqueous zinc ion batteries. *Mater. Today Energy*, 29, 101095
- [11] Shen, Z., Sun, Y., Xie, J., Liu, S., Zhuang, D., Zhang, G., Zheng, W., Cao, G., & Zhao, X. 2018. Manganese hexacyanoferrate/graphene cathodes for sodium-ion batteries with superior rate capability and ultralong cycle life. *Inorg. Chem. Front.*, 5, 2914–2920
- [12] Lee, H.-W., Wang, R. Y., Pasta, M., Woo Lee, S., Liu, N., & Cui, Y. 2014. Manganese hexacyanomanganate open framework as a high-capacity positive electrode material for sodium-ion batteries. *Nat. Commun.*, 5, 5280
- [13] Liu, C., Neale, Z. G., & Cao, G. 2016. Understanding electrochemical potentials of cathode materials in rechargeable batteries. *Mater. Today*, 19, 109–123
- [14] Trócoli, R., & La Mantia, F. 2015. An Aqueous Zinc-Ion Battery Based on Copper Hexacyanoferrate. *ChemSusChem*, 8, 481–485
- [15] Nam, K. W., Kim, H., Choi, J. H., & Choi, J. W. 2019. Crystal water for high performance layered manganese oxide cathodes in aqueous rechargeable zinc batteries. *Energy Environ. Sci*, 12, 1999–2009
- [16] He, P., Yan, M., Zhang, G., Sun, R., Chen, L., An, Q., & Mai, L. 2017. Layered VS₂ Nanosheet-Based Aqueous Zn Ion Battery Cathode. *Adv. Energy Mater.*, 7, 1601920
- [17] Naveed, A., Yang, H., Shao, Y., Yang, J., Yanna, N., Liu, J., Shi, S., Zhang, L., Ye, A., He, B., & Wang, J. 2019. A Highly Reversible Zn Anode with Intrinsically Safe Organic Electrolyte for Long-Cycle-Life Batteries. *Adv. Mater.*, 31, 1900668
- [18] Huang, M., Meng, J., Huang, Z., Wang, X., & Mai, L. 2020. Ultrafast cation insertion-selected zinc hexacyanoferrate for 1.9 V K–Zn hybrid aqueous batteries. *J. Mater. Chem. A*, 8, 6631–6637
- [19] Xu, C.-X., & Jiang, J.-J. 2021. Electrolytes speed up development of zinc batteries. *Rare Metals*, 40, 749–751
- [20] Zhu, R., Xiong, Z., Yang, H., Huang, T., Jeong, S., Kowalski, D., Kitano, S., Aoki, Y., Habazaki, H., & Zhu, C. 2022. A low-cost and non-corrosive

- electropolishing strategy for long-life zinc metal anode in rechargeable aqueous battery. *Energy Storage Mater.*, 46, 223–232
- [21] Ding, J., Du, Z., Gu, L., Li, B., Wang, L., Wang, S., Gong, Y., & Yang, S. 2018. Ultrafast Zn²⁺ Intercalation and Deintercalation in Vanadium Dioxide. *Adv. Mater.*, 30, 1800762
- [22] Hu, P., Yan, M., Zhu, T., Wang, X., Wei, X., Li, J., Zhou, L., Li, Z., Chen, L., & Mai, L. 2017. Zn/V₂O₅ Aqueous Hybrid-Ion Battery with High Voltage Platform and Long Cycle Life. *ACS Appl. Mater. Interfaces*, 9, 42717–42722
- [23] Zhang, N., Cheng, F., Liu, J., Wang, L., Long, X., Liu, X., Li, F., & Chen, J. 2017. Rechargeable aqueous zinc-manganese dioxide batteries with high energy and power densities. *Nat. Commun.*, 8, 405
- [24] Lee, B., Yoon, C. S., Lee, H. R., Chung, K. Y., Cho, B. W., & Oh, S. H. 2014. Electrochemically-induced reversible transition from the tunneled to layered polymorphs of manganese dioxide. *Sci. Rep.*, 4, 6066
- [25] Wei, C., Xu, C., Li, B., Du, H., & Kang, F. 2012. Preparation and characterization of manganese dioxides with nano-sized tunnel structures for zinc ion storage. *J. Phys. Chem. Solids*, 73, 1487–1491
- [26] Li, G., Yang, Z., Jiang, Y., Jin, C., Huang, W., Ding, X., & Huang, Y. 2016. Towards polyvalent ion batteries: A zinc-ion battery based on NASICON structured Na₃V₂(PO₄)₃. *Nano Energy*, 25, 211–217
- [27] Li, G., Yang, Z., Jiang, Y., Zhang, W., & Huang, Y. 2016. Hybrid aqueous battery based on Na₃V₂(PO₄)₃/C cathode and zinc anode for potential large-scale energy storage. *J. Power Sources*, 308, 52–57
- [28] Luu, N. T. H., Ivanov, A. S., Chen, T.-H., Popovs, I., Lee, J.-C., & Kaveevivitchai, W. 2022. Proton-enabled biomimetic stabilization of small-molecule organic cathode in aqueous zinc-ion batteries. *J. Mater. Chem. A*, 10, 12371–12377
- [29] Zhao, Q., Huang, W., Luo, Z., Liu, L., Lu, Y., Li, Y., Li, L., Hu, J., Ma, H., & Chen, J. 2018. High-capacity aqueous zinc batteries using sustainable quinone electrodes. *Sci. Adv.*, 4, 1761
- [30] Fang, G., Zhou, J., Pan, A., & Liang, S. 2018. Recent Advances in Aqueous Zinc-Ion Batteries. *ACS Energy Lett.*, 3, 2480–2501

- [31] Ma, L., Schroeder, M. A., Borodin, O., Pollard, T. P., Ding, M. S., Wang, C., & Xu, K. 2020. Realizing high zinc reversibility in rechargeable batteries. *Nat. Energy*, 5, 743–749
- [32] Guan, Q., Li, Y., Bi, X., Yang, J., Zhou, J., Li, X., Cheng, J., Wang, Z., Wang, B., & Lu, J. 2019. Dendrite-Free Flexible Fiber-Shaped Zn Battery with Long Cycle Life in Water and Air. *Adv. Energy Mater.*, 9, 1901434
- [33] Hao, J., Yuan, L., Ye, C., Chao, D., Davey, K., Guo, Z., & Qiao, S.-Z. 2021. Boosting Zinc Electrode Reversibility in Aqueous Electrolytes by Using Low-Cost Antisolvents. *Angew. Chem. Int. Ed.*, 60, 7366–7375
- [34] Liu, Z., Pulletikurthi, G., & Endres, F. 2016. A Prussian Blue/Zinc Secondary Battery with a Bio-Ionic Liquid-Water Mixture as Electrolyte. *ACS Appl. Mater. Interfaces*, 8, 12158–12164
- [35] Zhang, C., Holoubek, J., Wu, X., Daniyar, A., Zhu, L., Chen, C., Leonard, D. P., Rodríguez-Pérez, I. A., Jiang, J.-X., Fang, C., & Ji, X. 2018. A ZnCl₂ water-in-salt electrolyte for a reversible Zn metal anode. *ChemComm*, 54, 14097–14099
- [36] Wei, T., Ren, Y., Li, Z., Zhang, X., Ji, D., & Hu, L. 2022. Bonding interaction regulation in hydrogel electrolyte enable dendrite-free aqueous zinc-ion batteries from –20 to 60 °C. *J. Chem. Eng.*, 434, 134646
- [37] Wu, T., Zhou, W., Quan, Y., Chen, M., Tian, Q., Han, X., Xu, J., & Chen, J. 2022. Facile and green synthesis of nanocellulose with the assistance of ultraviolet light irradiation for high-performance quasi-solid-state zinc-ion batteries. *J. Colloid Interface Sci.*, 628, 1–9
- [38] Lipson, A. L., Han, S.-D., Kim, S., Pan, B., Sa, N., Liao, C., Fister, T. T., Burrell, A. K., Vaughey, J. T., & Ingram, B. J. 2016. Nickel hexacyanoferrate, a versatile intercalation host for divalent ions from nonaqueous electrolytes. *J. Power Sources*, 325, 646–652
- [39] Dong, Y., Di, S., Zhang, F., Bian, X., Wang, Y., Xu, J., Wang, L., Cheng, F., & Zhang, N. 2020. Nonaqueous electrolyte with dual-cations for high-voltage and long-life zinc batteries. *J. Mater. Chem. A*, 8, 3252–3261

- [40] Yaghoobnejad Asl, H., Sharma, S., & Manthiram, A. 2020. The critical effect of water content in the electrolyte on the reversible electrochemical performance of Zn–VPO₄F cells. *J. Mater. Chem. A*, 8, 8262–8267
- [41] Li, H., Ma, L., Han, C., Wang, Z., Liu, Z., Tang, Z., & Zhi, C. 2019. Advanced rechargeable zinc-based batteries: Recent progress and future perspectives. *Nano Energy*, 62, 550–587
- [42] Alfaruqi, M. H., Mathew, V., Gim, J., Kim, S., Song, J., Baboo, J. P., Choi, S. H., & Kim, J. 2015. Electrochemically Induced Structural Transformation in a γ -MnO₂ Cathode of a High Capacity Zinc-Ion Battery System. *Chem. Mater.*, 27, 3609–3620
- [43] Pan, H., Shao, Y., Yan, P., Cheng, Y., Han, K. S., Nie, Z., Wang, C., Yang, J., Li, X., Bhattacharya, P., Mueller, K. T., & Liu, J. 2016. Reversible aqueous zinc/manganese oxide energy storage from conversion reactions. *Nat. Energy*, 1, 16039
- [44] Sun, W., Wang, F., Hou, S., Yang, C., Fan, X., Ma, Z., Gao, T., Han, F., Hu, R., Zhu, M., & Wang, C. 2017. Zn/MnO₂ Battery Chemistry With H⁺ and Zn²⁺ Coinsertion. *J. Am. Chem. Soc.*, 139, 9775–9778
- [45] Yan, J., Wang, J., Liu, H., Bakenov, Z., Gosselink, D., & Chen, P. 2012. Rechargeable hybrid aqueous batteries. *J. Power Sources*, 216, 222–226
- [46] Zhang, N., Dong, Y., Wang, Y., Wang, Y., Li, J., Xu, J., Liu, Y., Jiao, L., & Cheng, F. 2019. Ultrafast Rechargeable Zinc Battery Based on High-Voltage Graphite Cathode and Stable Nonaqueous Electrolyte. *ACS Appl. Mater. Interfaces*, 11, 32978–32986
- [47] Kasiri, G., Trocoli, R., Hashemi, A. B., & La Mantia, F. 2016. An electrochemical investigation of the aging of copper hexacyanoferrate during the operation in zinc-ion batteries. *Electrochim. Acta*, 222, 74–83
- [48] Renman, V., Ojwang, D. O., Valvo, M., Gómez, C. P., Gustafsson, T., & Svensson, G. 2017. Structural-electrochemical relations in the aqueous copper hexacyanoferrate-zinc system examined by synchrotron X-ray diffraction. *J. Power Sources*, 369, 146–153

- [49] Li, Q., Ma, K., Yang, G., & Wang, C. 2020. High-voltage non-aqueous Zn/K_{1.6}Mn_{1.2}Fe(CN)₆ batteries with zero capacity loss in extremely long working duration. *Energy Storage Mater.*, 29, 246–253
- [50] Li, Q., Ma, K., Hong, C., Yang, Z., Qi, C. Z., Yang, G., & Wang, C. 2021. High-voltage K/Zn dual-ion battery with 100,000-cycles life using zero-strain ZnHCF cathode. *Energy Storage Mater.*, 42, 715–722
- [51] Li, Z., Liu, T., Meng, R., Gao, L., Zou, Y., Peng, P., Shao, Y., & Liang, X. 2021. Insights into the Structure Stability of Prussian Blue for Aqueous Zinc Ion Batteries. *EEM*, 4, 111–116
- [52] Naveed, A., Chen, J., Raza, B., Liu, Y., & Wang, J. 2022. Rechargeable hybrid organic Zn battery (ReHOZnB) with non-flammable electrolyte. *Journal of Electroanalytical Chemistry*, 904, 115949
- [53] Pan, C., Nuzzo, R. G., & Gewirth, A. A. 2017. ZnAl_xCo_{2-x}O₄ Spinel as Cathode Materials for Non-Aqueous Zn Batteries with an Open Circuit Voltage of ≤ 2 V. *Chemistry of Materials*, 29, 9351-9358
- [54] Pan, C., Zhang, R., Nuzzo, R. G., & Gewirth, A. A. 2018. ZnNi_xMn_xCo_{2-2x}O₄ Spinel as a High-Voltage and High-Capacity Cathode Material for Nonaqueous Zn-Ion Batteries. *Advanced Energy Materials*, 8, 1800589
- [55] Kaveevivitchai, W., & Manthiram, A. 2016. High-capacity zinc-ion storage in an open-tunnel oxide for aqueous and nonaqueous Zn-ion batteries. *Journal of Materials Chemistry A*, 4, 18737-18741
- [56] Park, M. J., Yaghoobnejad Asl, H., Therese, S., & Manthiram, A. 2019. Structural impact of Zn-insertion into monoclinic V₂(PO₄)₃: implications for Zn-ion batteries. *Journal of Materials Chemistry A*, 7, 7159-7167
- [57] Li, Q., Ma, K. X., Hong, C., Yang, G. Z., & Wang, C. X. 2021. Realizing excellent cycle stability of Zn/Na₃V₂(PO₄)₃ batteries by suppressing dissolution and structural degradation in non-aqueous Na/Zn dual-salt electrolytes. *SCMs*, 64, 1386–1395
- [58] Wu, S.-C., Tsa, M.-C., Liao, H.-J., Su, T.-Y., Tang, S.-Y., Chen, C.-W., Lo, H.-A., Yang, T.-Y., Wang, K., Ai, Y., Chen, Y.-Z., Lee, L., Lee, J.-F., Lin, C.-J., Hwang, B. J., & Chueh, Y.-L. 2022. Intercalation of Zinc Monochloride Cations

- by Deep Eutectic Solvents for High-Performance Rechargeable Non-aqueous Zinc Ion Batteries. *ACS Appl. Mater. Interfaces*, 14, 7814–7825
- [59] Zhou, L.-F., Gao, X.-W., Du, T., Gong, H., Liu, L.-Y., & Luo, W.-B. 2022. New Phosphate $Zn_2Fe(PO_4)_2$ Cathode Material for Nonaqueous Zinc Ion Batteries with Long Life Span. *ACS Appl. Mater. Interfaces*, 14, 8888–8895
- [60] Zhou, L.-F., Gao, X.-W., Du, T., Gong, H., Liu, L.-Y., & Luo, W.-B. 2022. A new phosphate member: $ZnMn_2(PO_4)_2$ as an advanced cathode material for aqueous and nonaqueous zinc ion batteries. *J. Alloys Compd*, 905, 163939
- [61] Bhatia, A., Xu, J., Pereira-Ramos, J.-P., Rouse, G., & Baddour-Hadjean, R. 2022. γ' - V_2O_5 Polymorph: A Genuine Zn Intercalation Material for Nonaqueous Rechargeable Batteries. *Chem. Mater.*, 34, 1203–1212
- [62] Han, S. D., Kim, S., Li, D. G., Petkov, V., Yoo, H. D., Phillips, P. J., Wang, H., Kim, J. J., More, K. L., Key, B., Klie, R. F., Cabana, J., Stamenkovic, V. R., Fister, T. T., Markovic, N. M., Burrell, A. K., Tepavcevic, S., & Vaughey, J. T. 2017. Mechanism of Zn Insertion into Nanostructured delta- MnO_2 : A Nonaqueous Rechargeable Zn Metal Battery. *Chem. Mater.*, 29, 4874–4884
- [63] Kao-ian, W., Nguyen, M. T., Yonezawa, T., Pornprasertsuk, R., Qin, J., Siwamogsatham, S., & Kheawhom, S. 2021. Highly stable rechargeable zinc-ion battery using dimethyl sulfoxide electrolyte. *Mater. Today Energy*, 21, 100738
- [64] Zhang, R., Pan, C., Nuzzo, R. G., & Gewirth, A. A. 2019. CoS_2 as a Sulfur Redox-Active Cathode Material for High-Capacity Nonaqueous Zn Batteries. *Journal of Physical Chemistry C*, 123, 8740–8745
- [65] Yang, M., Leon, N., Pan, B., Yu, Z., Cheng, L., & Liao, C. 2020. Mechanistic Insights in Quinone-Based Zinc Batteries with Nonaqueous Electrolytes. *Journal of The Electrochemical Society*, 167, 100536
- [66] Guerfi, A., Trottier, J., Boyano, I., De Meatza, I., Blazquez, J. A., Brewer, S., Ryder, K. S., Vjih, A., & Zaghbi, K. 2014. High cycling stability of zinc-anode/conducting polymer rechargeable battery with non-aqueous electrolyte. *Journal of Power Sources*, 248, 1099-1104

- [67] Tripathy, D., Viswanatha, H. M., Harish, M. N. K., & Sampath, S. 2022. Ion storage performance of a polymer for mono-, di- and tri-valent metal ions in non-aqueous electrolytes. *ChemComm*, 58, 7821–7824
- [68] Wang, N., Dong, X., Wang, B., Guo, Z., Wang, Z., Wang, R., Qiu, X., & Wang, Y. 2020. Zinc–Organic Battery with a Wide Operation-Temperature Window from –70 to 150 °C. *Angew. Chem. Int. Ed.*, 59, 14577–14583
- [69] Wang, K., Zhang, X., Han, J., Zhang, X., Sun, X., Li, C., Liu, W., Li, Q., & Ma, Y. 2018. High-Performance Cable-Type Flexible Rechargeable Zn Battery Based on MnO₂@CNT Fiber Microelectrode. *ACS Appl. Mater. Interfaces*, 10, 24573–24582
- [70] Wang, M. Q., Emre, A., Tung, S., Gerber, A., Wang, D. D., Huang, Y. D., Cecen, V., & Kotov, N. A. 2019. Biomimetic Solid-State Zn²⁺ Electrolyte for Corrugated Structural Batteries. *ACS Nano*, 13, 1107–1115
- [71] Ma, L. T., Chen, S. M., Li, H. F., Ruan, Z. H., Tang, Z. J., Liu, Z. X., Wang, Z. F., Huang, Y., Pei, Z. X., Zapien, J. A., & Zhi, C. Y. 2018. Initiating a mild aqueous electrolyte Co₃O₄/Zn battery with 2.2 V-high voltage and 5000-cycle lifespan by a Co(III) rich-electrode. *Energy Environ. Sci*, 11, 2521–2530
- [72] Zhao, Y. W., Ma, L. T., Zhu, Y. B., Qin, P., Li, H. F., Mo, F. N., Wang, D. H., Liang, G. J., Yang, Q., Liu, W. S., & Zhi, C. Y. 2019. Inhibiting Grain Pulverization and Sulfur Dissolution of Bismuth Sulfide by Ionic Liquid Enhanced Poly(3,4-ethylenedioxythiophene):Poly(styrenesulfonate) for High-Performance Zinc-Ion Batteries. *ACS Nano*, 13, 7270–7280
- [73] Lu, Y., Zhu, T., Xu, N., & Huang, K. 2019. A Semisolid Electrolyte for Flexible Zn-Ion Batteries. *ACS Applied Energy Materials*, 2, 6904–6910
- [74] Guo, F. J., Gao, S., Ji, C. C., Mi, H. Y., Li, H., Zhang, W. T., & Pang, H. 2021. Finely crafted polyaniline cathode for high-performance flexible quasi-solid-state Zn-ion battery. *Solid State Ion.*, 364, 115612
- [75] Wang, J. Q., Liu, J., Hu, M. M., Zeng, J., Mu, Y. B., Guo, Y., Yu, J., Ma, X., Qiu, Y. J., & Huang, Y. 2018. A flexible, electrochromic, rechargeable Zn//PPy battery with a short circuit chromatic warning function. *J. Mater. Chem. A*, 6, 11113–11118

- [76] Chae, M. S., & Hong, S.-T. 2019. Prototype System of Rocking-Chair Zn-Ion Battery Adopting Zinc Chevrel Phase Anode and Rhombohedral Zinc Hexacyanoferrate Cathode. *Batteries*, 5, 3
- [77] Renman, V., Ojwang, D. O., Valvo, M., Gomez, C. P., Gustafsson, T., & Svensson, G. 2017. Structural-electrochemical relations in the aqueous copper hexacyanoferrate-zinc system examined by synchrotron X-ray diffraction. *Journal of Power Sources*, 369, 146-153
- [78] Trocoli, R., Kasiri, G., & La Mantia, F. 2018. Phase transformation of copper hexacyanoferrate (KCuFe(CN)₆) during zinc insertion: Effect of co-ion intercalation. *J. Power Sources*, 400, 167–171
- [79] Jia, Z. J., Wang, B. G., & Wang, Y. 2015. Copper hexacyanoferrate with a well-defined open framework as a positive electrode for aqueous zinc ion batteries. *Materials Chemistry and Physics*, 149, 601-606
- [80] Gupta, T., Kim, A., Phadke, S., Biswas, S., Luong, T., Hertzberg, B. J., Chamoun, M., Evans-Lutterodt, K., & Steingart, D. A. 2016. Improving the cycle life of a high-rate, high-potential aqueous dual ion battery using hyper-dendritic zinc and copper hexacyanoferrate. *J. Power Sources*, 305, 22–29
- [81] Kasiri, G., Glenneberg, J., Hashemi, A. B., Kun, R., & La Mantia, F. 2019. Mixed copper-zinc hexacyanoferrates as cathode materials for aqueous zinc-ion batteries. *Energy Storage Mater.*, 19, 360–369
- [82] Zhang, Y. J., Wang, Y., Lu, L., Sun, C. W., & Yu, D. Y. W. 2021. Vanadium hexacyanoferrate with two redox active sites as cathode material for aqueous Zn-ion batteries. *J. Power Sources*, 484, 229263
- [83] Wang, F. X., Li, Y. P., Zhu, W. J., Ge, X. L., Cui, H. T., Feng, K., Liu, S. S., & Yang, X. 2021. Zn-Ion Batteries: Boosting the Rate Capability and Low-temperature Performance by Combining Structure and Morphology Engineering. *ACS Appl. Mater. Interfaces*, 13, 34468–34476
- [84] Wang, L. P., Wang, P. F., Wang, T. S., Yin, Y. X., Guo, Y. G., & Wang, C. R. 2017. Prussian blue nanocubes as cathode materials for aqueous Na-Zn hybrid batteries. *J. Power Sources*, 355, 18–22

- [85] Ma, L. T., Chen, S. M., Long, C. B., Li, X. L., Zhao, Y. W., Liu, Z. X., Huang, Z. D., Dong, B. B., Zapien, J. A., & Zhi, C. Y. 2019. Achieving High-Voltage and High-Capacity Aqueous Rechargeable Zinc Ion Battery by Incorporating Two-Species Redox Reaction. *Adv. Energy Mater.*, 9, 1902446
- [86] Li, W. R., Xu, C. W., Zhang, X. K., Xia, M. T., Yang, Z. W., Yan, H. H., Yu, H. X., Zhang, L. Y., Shu, W. J., & Shu, J. 2021. Sodium manganese hexacyanoferrate as Zn ion host toward aqueous energy storage. *Journal of Electroanalytical Chemistry*, 881, 114968
- [87] Deng, W. J., Li, Z. G., Ye, Y. K., Zhou, Z. Q., Li, Y. B., Zhang, M., Yuan, X. R., Hu, J., Zhao, W. G., Huang, Z. Y., Li, C., Chen, H. B., Zheng, J. X., & Li, R. 2021. Zn^{2+} Induced Phase Transformation of $K_2MnFe(CN)_6$ Boosts Highly Stable Zinc-Ion Storage. *Adv. Energy Mater.*, 11, 2003639
- [88] Song, J., Wang, L., Lu, Y., Liu, J., Guo, B., Xiao, P., Lee, J.-J., Yang, X.-Q., Henkelman, G., & Goodenough, J. B. 2015. Removal of interstitial H₂O in hexacyanometallates for a superior cathode of a sodium-ion battery. *J. Am. Chem. Soc.*, 137, 2658-2664
- [89] Toby, B. H., & Von Dreele, R. B. 2013. GSAS-II: the genesis of a modern open-source all purpose crystallography software package. *J. Appl. Cryst.*, 46, 544–549
- [90] Wu, X., Wu, C., Wei, C., Hu, L., Qian, J., Cao, Y., Ai, X., Wang, J., & Yang, H. 2016. Highly Crystallized $Na_2CoFe(CN)_6$ with Suppressed Lattice Defects as Superior Cathode Material for Sodium-Ion Batteries. *ACS Appl. Mater. Interfaces*, 8, 5393–5399
- [91] Song, J., Wang, L., Lu, Y., Liu, J., Guo, B., Xiao, P., Lee, J.-J., Yang, X.-Q., Henkelman, G., & Goodenough, J. B. 2015. Removal of Interstitial H₂O in Hexacyanometallates for a Superior Cathode of a Sodium-Ion Battery. *J. Am. Chem. Soc.*, 137, 2658–2664
- [92] Hu, M., Ishihara, S., Ariga, K., Imura, M., & Yamauchi, Y. 2013. Kinetically Controlled Crystallization for Synthesis of Monodispersed Coordination Polymer Nanocubes and Their Self-Assembly to Periodic Arrangements. *Chem. Eur. J.*, 19, 1882–1885

- [93] Uemura, T., & Kitagawa, S. 2003. Prussian Blue Nanoparticles Protected by Poly(vinylpyrrolidone). *J. Am. Chem. Soc.*, 125, 7814–7815
- [94] Wang, L., Lu, Y., Liu, J., Xu, M., Cheng, J., Zhang, D., & Goodenough, J. B. 2013. A Superior Low-Cost Cathode for a Na-Ion Battery. *Angew. Chem. Int. Ed.*, 52, 1964–1967
- [95] Kareis, C. M., Lapidus, S. H., Her, J.-H., Stephens, P. W., & Miller, J. S. 2012. Non-Prussian Blue Structures and Magnetic Ordering of $\text{Na}_2\text{Mn}^{\text{II}}[\text{Mn}^{\text{II}}(\text{CN})_6]$ and $\text{Na}_2\text{Mn}^{\text{II}}[\text{Mn}^{\text{II}}(\text{CN})_6]\cdot 2\text{H}_2\text{O}$. *J. Am. Chem. Soc.*, 134, 2246–2254
- [96] Xue, L., Li, Y., Gao, H., Zhou, W., Lü, X., Kaveevivitchai, W., Manthiram, A., & Goodenough, J. B. 2017. Low-Cost High-Energy Potassium Cathode. *J. Am. Chem. Soc.*, 139, 2164–2167
- [97] Li, W., Wang, K., Cheng, S., & Jiang, K. 2019. An Ultrastable Presodiated Titanium Disulfide Anode for Aqueous “Rocking-Chair” Zinc Ion Battery. *Adv. Energy Mater.*, 9, 1900993
- [98] Giri, A., Goswami, N., Pal, M., Zar Myint, M. T., Al-Harhi, S., Singha, A., Ghosh, B., Dutta, J., & Pal, S. K. 2013. Rational surface modification of Mn_3O_4 nanoparticles to induce multiple photoluminescence and room temperature ferromagnetism. *J. Mater. Chem. C*, 1, 1885–1895
- [99] Martínez-García, R., Reguera, E., Rodriguez, J., Balmaseda, J., & Roque, J. 2004. Crystal structures of some manganese(II) and cadmium hexacyanoferrates (II,III) and structural transformations related to the sorption of Cesium. *Powder Diffr.*, 19, 255–264
- [100] Song, M., Tan, H., Chao, D., & Fan, H. J. 2018. Recent Advances in Zn-Ion Batteries. *Adv. Funct. Mater.*, 28, 1802564
- [101] Johra, F. T., Lee, J. W., & Jung, W. G. 2014. Facile and safe graphene preparation on solution based platform. *J Ind Eng Chem*, 20, 2883–2887
- [102] Parthasarathi, N., & Duraiselvam, M. 2010. Improvement of high temperature wear resistance of AISI 316 ASS through NiCrBSiCFe plasma spray coating. *JMMCE*, 09, 653–670
- [103] Wang, R. Y., Shyam, B., Stone, K. H., Weker, J. N., Pasta, M., Lee, H.-W., Toney, M. F., & Cui, Y. 2015. Reversible Multivalent (Monovalent, Divalent,

- Trivalent) Ion Insertion in Open Framework Materials. *Adv. Energy Mater.*, 5, 1401869
- [104] Wang, L., Song, J., Qiao, R. M., Wray, L. A., Hossain, M. A., Chuang, Y. D., Yang, W. L., Lu, Y. H., Evans, D., Lee, J. J., Vail, S., Zhao, X., Nishijima, M., Kakimoto, S., & Goodenough, J. B. 2015. Rhombohedral Prussian White as Cathode for Rechargeable Sodium-Ion Batteries. *J. Am. Chem. Soc.*, 137, 2548–2554
- [105] Wilke, M., Farges, F. o., Petit, P.-E., Brown, G. E., Jr., & Martin, F. o. 2001. Oxidation state and coordination of Fe in minerals: An Fe K-XANES spectroscopic study. *Am. Mineral.*, 86, 714–730
- [106] Chalmin, E., Farges, F., & Brown, G. E. 2009. A pre-edge analysis of Mn K-edge XANES spectra to help determine the speciation of manganese in minerals and glasses. *Contrib. to Mineral. Petrol.*, 157, 111–126
- [107] Laschuk, N. O., Easton, E. B., & Zenkina, O. V. 2021. Reducing the resistance for the use of electrochemical impedance spectroscopy analysis in materials chemistry. *Rsc Advances*, 11, 27925-27936
- [108] Somerville, C., Youngs, H., Taylor, C., Davis, S. C., & Long, S. P. 2010. Feedstocks for Lignocellulosic Biofuels. *Science*, 329, 790-792
- [109] Yang, D., Qiu, X., Zhou, M., & Lou, H. 2007. Properties of sodium lignosulfonate as dispersant of coal water slurry. *Energy Convers.*, 48, 2433-2438
- [110] Yang, D., Qiu, X., Pang, Y., & Zhou, M. 2008. Physicochemical Properties of Calcium Lignosulfonate with Different Molecular Weights as Dispersant in Aqueous Suspension. *J Dispers Sci Technol*, 29, 1296-1303
- [111] Milczarek, G. 2010. Kraft lignin as dispersing agent for carbon nanotubes. *Journal of Electroanalytical Chemistry*, 638, 178-181
- [112] El-Khatib, E. M., Ali, N. F., Nassar, S. H., & El-Shemy, N. S. 2022. Functionalization of natural fibers properties by using TiO₂ nanoparticles to improve its antimicrobial activity. *Biointerface Res. Appl. Chem.*, 12, 4177-4191
- [113] Zimniewska, M., Kozłowski, R., & Batog, J. 2008. Nanolignin Modified Linen Fabric as a Multifunctional Product. *Mol. Cryst*, 484, 409-416

- [114] Chung, Y.-L., Olsson, J. V., Li, R. J., Frank, C. W., Waymouth, R. M., Billington, S. L., & Sattely, E. S. 2013. A Renewable Lignin–Lactide Copolymer and Application in Biobased Composites. *ACS Sustain. Chem. Eng.*, 1, 1231-1238
- [115] Xue, B.-L., Wen, J.-L., & Sun, R.-C. 2014. Lignin-Based Rigid Polyurethane Foam Reinforced with Pulp Fiber: Synthesis and Characterization. *ACS Sustain. Chem. Eng.*, 2, 1474-1480
- [116] Del Saz-Orozco, B., Oliet, M., Alonso, M. V., Rojo, E., & Rodríguez, F. 2012. Formulation optimization of unreinforced and lignin nanoparticle-reinforced phenolic foams using an analysis of variance approach. *Compos Sci Technol*, 72, 667-674
- [117] Yang, C., & Liu, P. 2009. Water-Dispersed Conductive Polypyrroles Doped with Lignosulfonate and the Weak Temperature Dependence of Electrical Conductivity. *Ind. Eng. Chem. Res.*, 48, 9498-9503
- [118] Wang, R., Jiao, L., Zhou, X., Guo, Z., Bian, H., & Dai, H. 2021. Highly fluorescent graphene quantum dots from biorefinery waste for tri-channel sensitive detection of Fe³⁺ ions. *J. Hazard. Mater.*, 412, 125096
- [119] Norgren, M., & Edlund, H. 2014. Lignin: Recent advances and emerging applications. *Curr. Opin. Colloid Interface Sci.*, 19, 409-416
- [120] Tran, M. H., Phan, D.-P., Nguyen, T. H., Kim, H. B., Kim, J., Park, E. D., & Lee, E. Y. 2021. Catalytic hydrogenolysis of alkali lignin in supercritical ethanol over copper monometallic catalyst supported on a chromium-based metal–organic framework for the efficient production of aromatic monomers. *Bioresour. Technol.*, 342, 125941
- [121] Kumar, A., Biswas, B., Kaur, R., Krishna, B. B., & Bhaskar, T. 2021. Hydrothermal oxidative valorisation of lignin into functional chemicals: A review. *Bioresour. Technol.*, 342, 126016
- [122] Hashmi, S. F., Meriö-Talvio, H., Ruuttunen, K., & Sixta, H. 2020. Influence of reaction conditions on solvolysis of organosolv lignin using water and green organic co-solvents as reaction medium. *FPT*, 197, 106200
- [123] Dong, M., Wu, C., Chen, L., Zhou, X., Yang, W., Xiao, H., Ji, X., Dai, H., Hu, C., & Bian, H. 2021. Benzenesulfonic acid-based hydrotropic system for

- achieving lignocellulose separation and utilization under mild conditions. *Bioresour. Technol.*, 337, 125379
- [124] Shi, Y., Xia, X., Li, J., Wang, J., Zhao, T., Yang, H., Jiang, J., & Jiang, X. 2016. Solvolysis kinetics of three components of biomass using polyhydric alcohols as solvents. *Bioresour. Technol.*, 221, 102-110
- [125] Kumar, A., Anushree, Kumar, J., & Bhaskar, T. 2020. Utilization of lignin: A sustainable and eco-friendly approach. *J. Energy Inst.*, 93, 235-271
- [126] Duan, D., Wang, Y., Ruan, R., Tayier, M., Dai, L., Zhao, Y., Zhou, Y., & Liu, Y. 2018. Comparative study on various alcohols solvolysis of organosolv lignin using microwave energy: Physicochemical and morphological properties. *Chem Eng Process*, 126, 38-44
- [127] Li, H., Cai, X., Wang, Z., & Xu, C. 2020. Cost-effective production of organosolv lignin from woody biomass using ethanol-water mixed solvent at mild conditions. *J. Supercrit. Fluids*, 158, 104745
- [128] Ahmad, E., & Pant, K. K. 2018. Lignin Conversion: A Key to the Concept of Lignocellulosic Biomass-Based Integrated Biorefinery. In T. Bhaskar, A. Pandey, S. V. Mohan, D.-J. Lee, & S. K. Khanal (Eds.), *Waste Biorefinery* (pp. 409-444): Elsevier.
- [129] Inkrod, C., Raita, M., & Laosiripojana, N. 2017. Characteristics of lignin extracted from pararubber wood sawdust via organosolv fractionation. *JGSEE*, 8, 71-76
- [130] Bundhoo, Z. M. A. 2018. Microwave-assisted conversion of biomass and waste materials to biofuels. *Renewable Sustainable Energy Rev.*, 82, 1149-1177
- [131] Yu, H. B., Ding, L. F., Wang, Z., & Shi, L. X. 2014. Study on Extraction of Polyphenol from Grape Peel Microwave-Assisted Activity. *Adv Mat Res.*, 864-867, 520-525
- [132] Imman, S., Arnthong, J., Burapatana, V., Champreda, V., & Laosiripojana, N. 2015. Fractionation of rice straw by a single-step solvothermal process: Effects of solvents, acid promoters, and microwave treatment. *Renewable Energy*, 83, 663-673

- [133] Zhou, L., Budarin, V., Fan, J., Sloan, R., & Macquarrie, D. 2017. Efficient Method of Lignin Isolation Using Microwave-Assisted Acidolysis and Characterization of the Residual Lignin. *ACS Sustain. Chem. Eng.*, 5, 3768-3774
- [134] Ninomiya, K., Yamauchi, T., Ogino, C., Shimizu, N., & Takahashi, K. 2014. Microwave pretreatment of lignocellulosic material in cholinium ionic liquid for efficient enzymatic saccharification. *Biochem. Eng. J.*, 90, 90-95
- [135] Bonechi, C., Consumi, M., Donati, A., Leone, G., Magnani, A., Tamasi, G., & Rossi, C. 2017. Biomass: An overview. In F. Dalena, A. Basile, & C. Rossi (Eds.), *Bioenergy Systems for the Future* (pp. 3-42): Woodhead Publishing.
- [136] Klass, D. L. 1998. Photosynthesis of Biomass and Its Conversion-Related Properties. In D. L. Klass (Ed.), *Biomass for Renewable Energy, Fuels, and Chemicals* (pp. 51-90). San Diego: Academic Press.
- [137] G. Calvo-Flores, F. 2020. Lignin a Renewable Raw Material. In *Encyclopedia of Renewable and Sustainable Materials* (pp. 2224).
- [138] Chio, C., Sain, M., & Qin, W. 2019. Lignin utilization: A review of lignin depolymerization from various aspects. *Renewable and Sustainable Energy Reviews*, 107, 232-249
- [139] Ogunkoya, D., Li, S., Rojas, O. J., & Fang, T. 2015. Performance, combustion, and emissions in a diesel engine operated with fuel-in-water emulsions based on lignin. *Appl. Energy*, 154, 851-861
- [140] Schoning, A. e. 1965. Absorptiometric determination of acid-soluble lignin in semichemical bisulfite pulps and in some woods and plants. *Svensk Papperstidning-nordisk Cellulosa*, 68, 607-613
- [141] Horst, D. J., Ramírez Behainne, J. J., de Andrade Júnior, P. P., & Kovaleski, J. L. 2014. An experimental comparison of lignin yield from the Klason and Willstatter extraction methods. *Energy Sustain Dev*, 23, 78-84
- [142] Obst, J. R., & Kirk, T. K. 1988. Isolation of lignin. In *Methods in Enzymology* (Vol. 161, pp. 3-12): Academic Press.

- [143] Wang, R., Luo, Y., Jia, H., Ferrell, J. R., & Ben, H. 2020. Development of quantitative ¹³C NMR characterization and simulation of C, H, and O content for pyrolysis oils based on ¹³C NMR analysis. *RSC Adv.*, 10, 25918-25928
- [144] Bu, L., Tang, Y., Gao, Y., Jian, H., & Jiang, J. 2011. Comparative characterization of milled wood lignin from furfural residues and corncob. *J. Chem. Eng.*, 175, 176-184
- [145] El Hage, R., Brosse, N., Chrusciel, L., Sanchez, C., Sannigrahi, P., & Ragauskas, A. 2009. Characterization of milled wood lignin and ethanol organosolv lignin from miscanthus. *Polym. Degrad. Stab.*, 94, 1632-1638
- [146] Ramakoti, B., Dhanagopal, H., Deepa, K., Rajesh, M., Ramaswamy, S., & Tamilarasan, K. 2019. Solvent fractionation of organosolv lignin to improve lignin homogeneity: Structural characterization. *Bioresource Technology Reports*, 7, 100293
- [147] Stark, N., Yelle, D., & Agarwal, U. 2015. Techniques for Characterizing Lignin. In *Lignin in Polymer Composites* (pp. 49-66).
- [148] Lin, S. Y., & Dence, C. W. (1992). *Methods in Lignin Chemistry*: Springer Berlin Heidelberg.
- [149] Capareda, S. C. 2022. Comprehensive biomass characterization in preparation for conversion. In D. Mohan, C. U. Pittman, & T. E. Mlsna (Eds.), *Sustainable Biochar for Water and Wastewater Treatment* (pp. 1-37): Elsevier.
- [150] Agarwal, A., Rana, M., & Park, J.-H. 2018. Advancement in technologies for the depolymerization of lignin. *FPT*, 181, 115-132
- [151] Gude, V. G., Patil, P., Martinez-Guerra, E., Deng, S., & Nirmalakhandan, N. 2013. Microwave energy potential for biodiesel production. *Sustainable Chemical Processes*, 1, 5
- [152] Davis, J. L., & Young, R. A. 1991. Microwave-Assisted Solvent Pulping. *Holzforschung*, 45, 71-78
- [153] Chemat, F., & Esveld, E. 2001. Microwave Super-Heated Boiling of Organic Liquids: Origin, Effect and Application. *Chem Eng Technol*, 24, 735-744
- [154] Biermann. 2018. Raw Material and Pulp Making. In *Handbook of Pulp and Paper*: Elsevier Science.

- [155] Dillen, J. R., Dillén, S., & Hamza, M. 2016. Wood Sources. In *Pulp and Paper*.
- [156] Riyaphan, J., Phumichai, T., Neimsuwan, T., Witayakran, S., Sungsing, K., Kaveeta, R., & Phumichai, C. 2015. Variability in chemical and mechanical properties of Pará rubber (*Hevea brasiliensis*) trees. *ScienceAsia*, 41, 251
- [157] Nitsos, C., Rova, U., & Christakopoulos, P. (2018). Organosolv Fractionation of Softwood Biomass for Biofuel and Biorefinery Applications. *Energies*, 11(1), 50
- [158] Monteil-Rivera, F., Huang, G. H., Paquet, L., Deschamps, S., Beaulieu, C., & Hawari, J. 2012. Microwave-assisted extraction of lignin from triticale straw: Optimization and microwave effects. *Bioresour. Technol.*, 104, 775-782
- [159] Johansen, T., & Schramm, J. 2009. Low-Temperature Miscibility of Ethanol-Gasoline-Water Blends in Flex Fuel Applications. *Energy Sources, Part A*, 1634-1645
- [160] Gupta, P., Sae-wang, V., Kanbua, P., & Laoonual, Y. 2018. Impact of water contents blended with ethanol on si engine performance and emissions. *Journal of Research and Applications in Mechanical Engineering*, 1, 7-11
- [161] Tappi, T. 2006. Acid-insoluble lignin in wood and pulp. *TAPPI Test Methods*, 1–7
- [162] Alejandro, R., Eduardo, E., Juan, D.-R., Rafael, S., Isabel, B., & Antonio, R. 2018. Different Solvents for Organosolv Pulping. In K. Salim Newaz (Ed.), *Pulp and Paper Processing*. Rijeka: IntechOpen.
- [163] Xu, J., Jiang, J., Hse, C., & Shupe, T. F. 2012. Renewable chemical feedstocks from integrated liquefaction processing of lignocellulosic materials using microwave energy. *Green Chem.*, 14, 2821-2830
- [164] Muley, P. D., Mobley, J. K., Tong, X., Novak, B., Stevens, J., Moldovan, D., Shi, J., & Boldor, D. 2019. Rapid microwave-assisted biomass delignification and lignin depolymerization in deep eutectic solvents. *Energy Convers.*, 196, 1080-1088
- [165] Yuan, T.-Q., Sun, S.-N., Xu, F., & Sun, R.-C. 2011. Characterization of Lignin Structures and Lignin–Carbohydrate Complex (LCC) Linkages by Quantitative

- 13C and 2D HSQC NMR Spectroscopy. *J. Agric. Food Chem.*, 59, 10604-10614
- [166] Guerra, A., Mendonça, R., Ferraz, A., Lu, F., & Ralph, J. 2004. Structural Characterization of Lignin during Pinus taeda Wood Treatment with Ceriporiopsis subvermispora. *AEM*, 70, 4073-4078
- [167] Huang, C., He, J., Narron, R., Wang, Y., & Yong, Q. 2017. Characterization of Kraft Lignin Fractions Obtained by Sequential Ultrafiltration and Their Potential Application as a Biobased Component in Blends with Polyethylene. *ACS Sustain. Chem. Eng.*, 5, 11770-11779
- [168] Lee, R. A., Bédard, C., Berbereri, V., Beauchet, R., & Lavoie, J.-M. 2013. UV–Vis as quantification tool for solubilized lignin following a single-shot steam process. *Bioresour. Technol.*, 144, 658-663
- [169] Araújo, L. C. P., Yamaji, F. M., Lima, V. H., & Botaro, V. R. 2020. Kraft lignin fractionation by organic solvents: Correlation between molar mass and higher heating value. *Bioresour. Technol.*, 314, 123757
- [170] Zhou, L., Boot, M. D., Johansson, B. H., & Reijnders, J. J. E. 2014. Performance of lignin derived aromatic oxygenates in a heavy-duty diesel engine. *Fuel*, 115, 469-478
- [171] Zhou, L., Boot, M. D., & Johansson, B. H. 2013. Comparison of emissions and performance between saturated cyclic oxygenates and aromatics in a heavy-duty diesel engine. *Fuel*, 113, 239-247

AUTHOR BIOGRAPHY

Author: Mr. Trakarn Yimtrakarn
Degree: Master of Engineering
Date: 4th June 2017
Date of Birth: 05th Dec 1997
Place of Birth: Thailand

Undergraduate and Graduate Education:

2020-2023: **Master of Chemical Engineering (Dual Degree)**, King Mongkut's Institute of Technology Ladkrabang (Thailand), GPA: 3.69/4.00

2010-2023: **Master of Chemical Engineering (Dual Degree)**, National Cheng Kung University (Taiwan), GPA: 87.5/100 (6 credits)

2016-2020: **Bachelor of Chemical Engineering**, King Mongkut's Institute of Technology Ladkrabang (Thailand), GPA: 3.25/4.00 (second-class honors)

Major: Chemical Engineering

Presentations and Publications:

Yimtrakarn, T.; Kaveevivitchai, W.; Lee, W.-C.; Lerkkasemsan, N. *Polymers* **2022**, *14*, 814. <https://doi.org/10.3390/polym14040814>.

Yimtrakarn, T.; Liao, Y.-C.; Mv, A. S.; Chen, J.-L.; Chuang, Y.-C.; Lerkkasemsan, N.; Kaveevivitchai, W. *Mater. Today Commun.* **2023**, *34*, 105231. <https://doi.org/10.1016/j.mtcomm.2022.105231>.

2023 HIGEM Conference **Best Poster Award**